8-2016

Development and Implementation of an Anthropomorphic Head & Neck Phantom for the Assessment of Proton Therapy Treatment Procedures

Daniela Branco

DEVELOPMENT AND IMPLEMENTATION OF AN ANTHROPOMORPHIC HEAD AND NECK PHANTOM FOR THE ASSESSMENT OF PROTON THERAPY TREATMENT PROCEDURES

by

Daniela Rezende Fiuza Branco,BS

APPROVED:

Advisory Professor - David Followill, Ph.D.

Paige Taylor, M.S.

Xiaodong Zhang, Ph.D.

Heng Li, Ph.D.

Michele Guindani, Ph.D.

APPROVED:

Dean, The University of Texas
Graduate School of Biomedical Sciences at Houston

DEVELOPMENT AND IMPLEMENTATION OF AN ANTHROPOMORPHIC HEAD AND NECK PHANTOM FOR THE ASSESSMENT OF PROTON THERAPY TREATMENT PROCEDURES

A THESIS

Presented to the Faculty of
The University of Texas
Health Science Center at Houston

and

The University of Texas
MD Anderson Cancer Center
Graduate School of Biomedical Sciences

in Partial Fulfillment
of the Requirements
for the Degree of

MASTER OF SCIENCE

By

Daniela Rezende Fiuza Branco, BS.

Houston, Texas

August 2016

Dedication

To my parents, Manuel and Celeste, brother, Luciano, and all my wonderful friends.

For always being together,

never apart.

Maybe in distance,

but never in heart.

Unknown Author

Acknowledgements

I would like to thank my advisor, Dr. Followill, not only for the support and patience, but also for all the research and life advices along the way.

I would also like to acknowledge and thank my committee members for their crucial guidance and time: Paige Taylor, Dr. Xiaodong Zhang, Dr. Heng Li, Dr. Michele Guindani.

I would also like to thank John Costales, our phantom engineer, for constructing our phantom, Cody Wages, our proton dosimetrist, for the help and advice with the treatment planning, Matt Kerr, our senior physics assistant, for the help with the delivery of the proton treatments, Hunter Mehrens, for the help with the phantom analysis software, and the IROC Houston staff, Carrie Amador, Natalie Torres, Nadia Hernandez, Lynda McDonald for all the assistance with the TLD and film dosimetry.

Lastly, I would like to express my appreciation to my family and friends. Thank you for always being there to support me and specially for having made this experience possible.

Development and Implementation of an Anthropomorphic Head & Neck Phantom for the Assessment of Proton Therapy Treatment Procedures

By: Daniela Branco, B.S.

Chair of Advisory Committee: David Followill, Ph.D.

Proton therapy has been used to treat cancer for more than 50 years, and over the past decade, its use has grown rapidly. One of the main goals of modern radiation therapy is to deliver a high dose to the planning target volume (PTV) with minimal exposure and damage to the surrounding healthy tissue. Protons offer a unique advantage over photon radiotherapy in that they deposit dose over a finite range, in contrast to the more gradual energy deposition of photon and electron beams. At present, 23 proton centers are in operation in the United States and another 13 centers are in development. The increasing interest in the use of protons creates a demand for quality monitoring and evaluation of the treatments provided, especially as they apply to NCI funded clinical trials. The goal of the Imaging and Radiation Oncology Core (IROC) Houston QA Center is to assure NCI that institutions participating in clinical trials deliver radiation treatment plans/doses that are clinically comparable and consistent. IROC Houston makes use of anthropomorphic QA phantoms in order to help verify the quality of the proton treatment process from imaging to treatment delivery. With new Head and Neck (H&N) proton therapy trials being developed, IROC Houston needs a H&N proton phantom that can be used as part of credentialing. Therefore, the hypothesis of this study is that an anthropomorphic H&N phantom can be designed and built to evaluate proton therapy H&N treatment procedures that can reproducibly (±3%) assure agreement between the measured doses and calculated doses to within ±7%/4mm.

Table of Contents

List of Illustrations

List of Tables

1 Introduction and Background

1.1 Statement of Problem

1.1.1 General Problem

Proton therapy has been used to treat cancer for more than 50 years, and over the past decade, its use has grown rapidly. At present, 23 proton centers are in operation in the United States and another 13 centers are in development [1]. As a consequence of the increasing interest in the use of protons, the demand for good quality assurance (QA) programs to control and maintain the standard of quality of patient care is high. Even though each particular proton therapy facility already has its own set of comprehensive quality assurance tests in place, based on the recommendations from the International Commission on Radiation Units and Measurements (ICRU) [2], an independent QA program that confirms accuracy, comparability and consistency of proton therapy delivery between facilities is also needed, especially for clinical trial activities.

As a core support for its clinical trials, the National Cancer Institute (NCI) funds various quality assurance centers across the country in order to provide trial support and to help assure that institutions are delivering comparable and consistent doses of radiation. The Imaging and Radiation Oncology Core (IROC) Houston QA Center, formerly known as the Radiological Physics Center (RPC) [3], is one of those QA centers and has as a mission to assure NCI that participating institutions have acceptable quality assurance procedures and no significant systematic dosimetry inconsistencies, so that each site can be considered qualified and capable of providing quality clinical treatments for cancer patients. This is especially true for clinical trials that allow proton therapy since it is a relatively new mainstream form of

radiation therapy. In fact, the NCI, in 2012, developed guidelines [4] for the use of proton therapy in NCI funded multi-institutional clinical trials. These guidelines specify an approval process that each new proton facility has to go through before being allowed to enter a proton treated patient onto NCI clinical trials. In addition to the proton approval process, the guidelines also describe the use of protocol specific credentialing requirements. IROC Houston's proton therapy approval process consists of completing a facility questionnaire, irradiating baseline anthropomorphic QA phantoms, consistent treatment of at least 3 anatomic sites at the facility, annual remote monitoring of the proton beam outputs and an on-site dosimetry reviews by an IROC physicist. IROC Houston also conducts a variety of credentialing activities, such as; protocol specific questionnaires to evaluate an institution's understanding of the protocol and their capabilities, treatment-planning standards to allow the institution to demonstrate their planning ability, and protocol specific use of anthropomorphic phantoms in order to verify the end to end process from imaging to treatment planning to setup to dose delivery for the specific treatment conditions of the protocol [5]. These mailable anthropomorphic QA phantoms used for the approval and credentialing processes are an important part of the remote monitoring audits and are used to verify the accuracy of the dose delivery for the individual proton treatments as they represent a hypothetical and/or patient treatment. These patient treatment verifications typically measure the precision of the dose delivered as well as the spatial distribution of the dose. The use of thermoluminescent dosimeters (TLDs) for point-dose measurements and radiochromic film for relative-dose distributions allows IROC Houston to measure the dose distribution delivered to the phantom that can then be compared to the dosimetry data calculated by the proton institutions to verify the accuracy of the planned proton treatment [6].

1.1.2 Specific Problem

The NCI guidelines for the use of proton therapy in its clinical trials outline a credentialing process for the participating proton institutions that requires the use of anthropomorphic phantoms in order to mimic patient radiation treatment plans. With the recent increase in the use of Intensity Modulated Proton Therapy (IMPT) and as targets become more complex, the IROC Houston QA Center has developed a need to remotely evaluate the planning and dose delivery of these treatments as part of trial credentialing. In order to test the system's ability to deliver a conformal dose to a target, and avoid dose to surrounding critical structures the IROC Houston has developed and used ten different heterogeneous, anthropomorphic phantoms that are used for clinical trial credentialing. The phantoms that have been previously designed and intended to be easily mailed to the institutions as an end to end QA monitoring include a stereotactic radiosurgery head phantom, a proton head phantom, an IMRT head-and-neck (H&N) phantom, a photon spine phantom, a proton spine phantom, a photon lung phantom, a proton lung phantom, a photon liver phantom, a proton liver phantom and a photon/proton pelvic-prostate phantom [3]. At this time, IROC Houston does not have an anthropomorphic QA H&N phantom that can be used to credential IMPT treatments for an oropharynx clinical trial comparing IMPT to IMRT that will soon be included in the NCI's clinical trial portfolio.

1.2 Head and Neck Cancer

Cancers of the oral cavity and oropharynx, which include the cancers of the lip, tongue and mouth, oropharynx, excluding the salivary glands and other pharyngeal sites, constitute a serious problem in the world. These anatomically related cancers, grouped together, represent the sixth most common cancers worldwide [7]. The yearly global incidence of oral cavity cancer is estimated to be approximately 263,000 cases, and the number of deaths from this cancer to be 127,000 [8]. In 2013, it was also estimated that 41,380 people were newly diagnosed and 7,890 died from these cancers in the United States [9].

Most of the cancers (>90%) of the oral cavity and oropharynx are squamous cell carcinomas (SCCs) [10]. Head and neck squamous cell carcinoma (HNSCC) is a term for squamous cell cancers that include the oral cavity, nasal cavity, the paranasal sinuses, the pharynx and the larynx. The oral cavity commonly includes the lips, anterior two thirds of the tongue, gingiva, hard palate, buccal and labial mucosa, retromolar pad, and floor of the mouth. The pharynx is considered to begin behind the nose and extend to the top of the trachea and esophagus (about 5 inches long), and is divided into three sections: nasopharynx, hypopharynx, and oropharynx, where the term “oropharynx” referrers to the posterior one third of the tongue, soft palate, palatine and lingual tonsils, and the posterior pharyngeal wall [11]. The anatomical sites and sizes of these malignancies will greatly influence the associated risk factors and the possible treatment options [12, 13].

Head and neck malignancies account for about 10% of all the cancers around the world, with roughly 40% of these cancers occurring in the oral cavity, 25% in the larynx, 15% in the pharynx, and the rest in the remaining sites (salivary glands, thyroid) [14]. The exact causes of these carcinomas are not sufficiently understood. Nevertheless, head and neck

cancers have been strongly correlated with alcohol and tobacco abuse, where each factor alone may account for a two- to three-fold increase in risk [15-17]. Even though tobacco and alcohol consumption are said to be the main aetiological factors, other risk factors have also been correlated with the disease. Viral agents, such as Epstein–Barr Virus (EBV) and the human papilloma virus (HPV) [18-20], dietary deficiencies or imbalances [21-23], dental health [24, 25], occupation [26-28], and genetic and familial factors [29, 30] have been suggested to not necessarily be the cause of these malignancies but to be associated, individually or in combination, with an increased probability of the occurrence of these cancers.

According to the International Agency for Research on Cancer (IARC), around 60 to 80% of these malignancies could be prevented by monitoring the established risk factors [31]. Specifics that can be used as predictors of survival are reported to be tumor size, tumor stage, nodal status, grade of tumor, performance status, site of primary, thickness, depth of invasion, tumor margin, etc [13]. Prognosis is highly dependent on the local invasion and lymph node involvement. The 5 year survival rate is approximately 50% when lymph nodes are not involved, and falls to 30% in the case of lymph node involvement [14]. By the time a diagnosis is made, more than 40% of the patients have one or more metastatic sites, sometimes due to the first observable symptoms being minimal or even to being minimized by the patient or physician. Pain does not necessary start early, which results on more than 50% of the tumors to being detected at an advanced stage [14].

Currently, concurrent radiation therapy and chemotherapy is considered the standard of care for most of the patients with advanced head and neck malignancies [32, 33]. These advanced head and neck cancers require the delivery of reasonably high doses to the planning target volume. Due to the presence of large tissue heterogeneities, the large extension of the

treatment region, the variety of anatomical shapes and position of targets and organs at risk, planning treatments is one of the most complex tasks of conventional radiotherapy. Proton therapy, specifically IMPT, is now being considered to be a viable therapeutic option for patients with H&N cancers due to their dosimetry characteristics, as described below, that can limit damage to surrounding normal tissues.

1.3 Protons in Radiation Therapy

1.3.1 Background

The idea of using energetic protons in medical treatments was first proposed by physicist Robert R. Wilson, Ph.D, in 1946. The use of proton radiation to treat patients was first attempted in the 1950s, however applications were restricted to limited areas of the body. In the late 1970s, with the development of newer technologies and improved accelerators, proton therapy was made more viable for medical applications, such as cancer treatment [34].

Similarly to photons, protons used in radiation therapy cause damage to the DNA of cells and ultimately can lead to cell death. As protons travel through tissue, they interact with atomic electrons and nuclei in the medium through Coulomb forces. These interactions will often produce ionizations and consequently result in absorbed dose. The deposition of energy through the medium, or dose, is described by the proton beam stopping power. The stopping power is dependent on the energy of the proton beam and on the properties of the medium it transverses through. Hence, the stopping power refers to the energy lost per unit path length of the material and is given by Equation 1 [35, 36].

$$\mathbf{S(E)} = \frac{\mathbf{dE}}{\mathbf{dx}} \qquad \textbf{Equation 1}$$

Where S is the linear stopping power which is a function of energy (E), and dE is the mean energy lost as the proton transverses a distance dx, typically given in MeV/cm.

In order to obtain the stopping power that is independent of the density of the material the equation above can be normalized by the density of the absorbing medium, and is expressed in Equation 2: [35, 36]

$$\mathbf{S(E)/\rho} = \frac{\mathbf{1}}{\boldsymbol{\rho}} \frac{\mathbf{dE}}{\mathbf{dx}} \qquad \textbf{Equation 2}$$

Where $S(E)/\rho$ is the mass stopping power and ρ is the density of the material, given in MeV-cm^2/g.

The average distance the proton travels before coming to complete stop, called the particle range, can simply by obtained by integrating the stopping power formula above and is shown in Equation 3: [35, 36]

$$\mathbf{R} = \oint_{\mathbf{0}}^{\mathbf{E_0}} \frac{\mathbf{1}}{\mathbf{S(E)}} \mathbf{dE} \qquad \textbf{Equation 3}$$

Where R is the range, S(E) is the linear stopping power and E_0 is the initial kinetic energy of the proton, thus given in g/cm^2.

The correct prediction of the position in which the protons will stop is crucial for a precise treatment. The accuracy in proton therapy treatment planning strongly depends on the precision of the stopping power information of the tissues in the patient's body so that the deposition of the dose is mainly focused in the target, with the sparing of the healthy surrounding critical structures [37].

1.3.2 Formation of the Proton Beam

Protons are required to be accelerated to very high energies (160 to 250 MeV) in order to be suitable for medical purposes. There are 3 types of proton accelerators: linear accelerators, cyclotrons and synchrotrons. However, because of the need of protons to be accelerated to very high energies in the clinic, conventional linear accelerators are not appropriate for radiotherapy. In order to achieve those energies, linear accelerators would be required to occupy a large space and therefore are not preferred in radiation therapy. Even though new technologies such as laser plasma particle and high-gradient electrostatic accelerators are being developed, cyclotrons and synchrotrons are currently the main accelerators used in proton beam therapy [35].

1.3.2.1 Cyclotrons

In a cyclotron, positively charged particles, such as protons and deuterons, are injected into the center of a round chamber. An electric field is applied at certain parts of the chamber, accelerating the particles and increasing their velocity. They are forced to travel in a circular motion due to the application of magnetic fields. With the increase in speed from the electric fields, the radius of the particles increases and can then be controlled by the magnetic fields along the chamber, until they exit with relatively low energies. The proton energies are limited because they achieve relativistic speeds, where additional acceleration causes the particle to gain mass and change their rotational period. A simplified diagram of a cyclotron is shown in Figure 1.1.

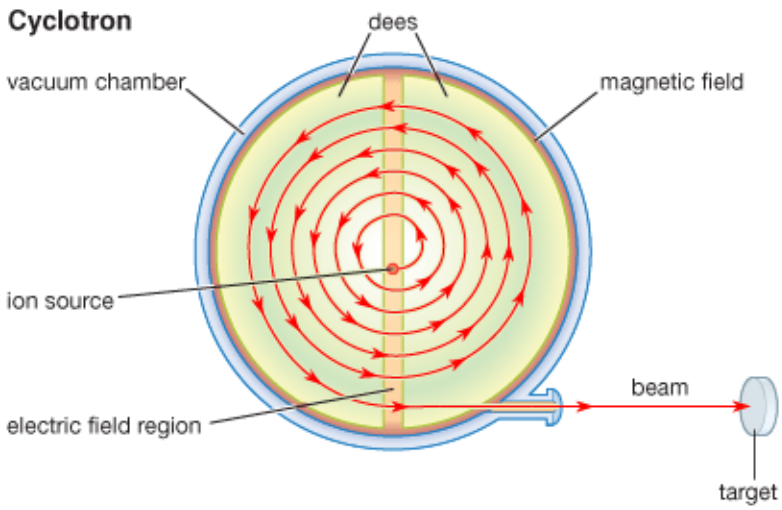

Figure 1-1: Diagram of a Cyclotron
Taken from: https://trac.cc.jyu.fi/projects/ohj1s13/wiki/suunnitelmat/joautant

Synchrocyclotrons and isochronous cyclotrons, on the other hand, can compensate for the increase in particle mass and accelerate particles to much higher energies. Synchrocyclotrons allow for adjustments in the frequency so that the proton's orbital motion still resonates with the electric field and isochronous cyclotrons increase the magnetic field with radius in order to keep a constant cyclotron frequency with energy, allowing for much higher speeds to be obtained (250 MeV). The high energy proton beams can then be modulated to treat at any depth with the use of energy degraders [35].

1.3.2.2 Synchrotrons

The University of Texas MD Anderson Cancer Center Proton Therapy Center in Houston (PTC-H) uses a synchrotron (70 – 250 MeV) to produce their proton beam [38]. Synchrotrons accelerate the particles by injecting low energy protons (3 to 7 MeV) into a narrow vacuum tube ring, where they are accelerated periodically with the use of radiofrequency (RF) cavities. Bending magnets keep the charged particles in the circular orbit. The RF frequency and the magnets strengths' are adapted as the protons' energy is increased,

until the desired beam is obtained, and can then be extracted. A schematic of a synchrotron accelerator can be seen in Figure 1.2.

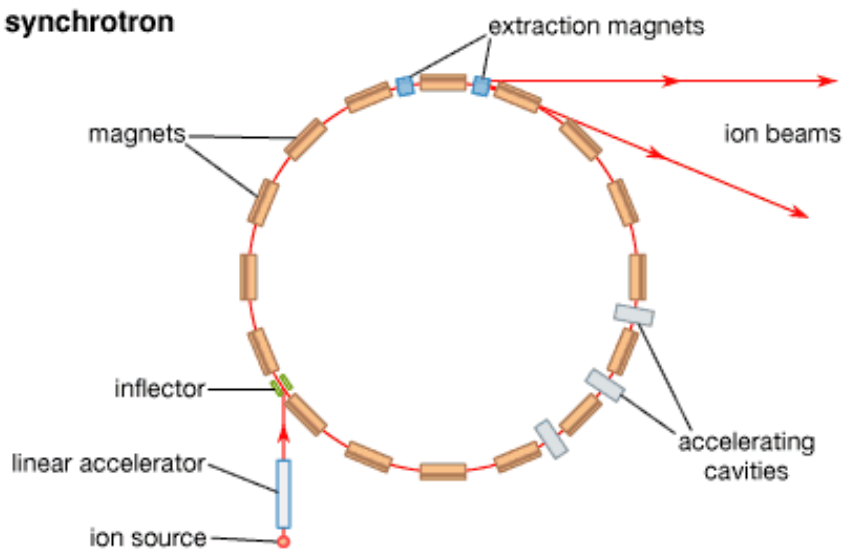

Figure 1-2: Diagram of a Synchrotron

Taken from: http://kids.britannica.com/comptons/art-124574/Particles-are-injected-into-the-ring-of-an-alternating-gradient

In contrast to cyclotrons, synchrotrons can accelerate the particles to the precise energies needed for radiation therapy. That advantage allows for the production of beams that can treat at any depth without the need for energy degraders, which produce greater neutron contamination, create higher post treatment radioactivity and require more shielding [35].

1.3.3 Proton Therapy Treatment Modalities

1.3.3.1 Passive Scattering

The simplest way of spreading a near-monoenergetic proton beam to a useful field size is by using a high atomic number scattering foil, similar to linear accelerators for electron treatments. These passive scattering systems require the use of custom blocks, usually made with brass or cerrobend, range compensators and range modulators. Figure 1.3 shows an example of the custom blocking used to shape the desired treatment field. Range compensators on the other hand, made with low atomic number materials, are used to compensate for patient surface irregularity, PTV surfaces and tissue heterogeneity, and are shown in Figure 1.4. Finally, range modulators are necessary to spread the Bragg peak in depth so that the entire PTV thickness is covered (SOBP), shown in Figure 1.5.

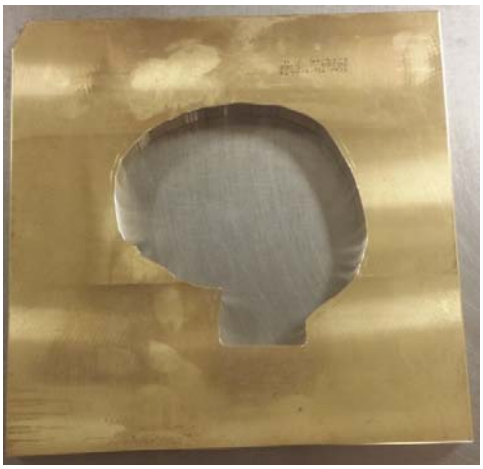

Figure 1-3: Passive scattering brass aperture for cranial blocking

Figure 1-4: Acrylic passive scattering range compensators

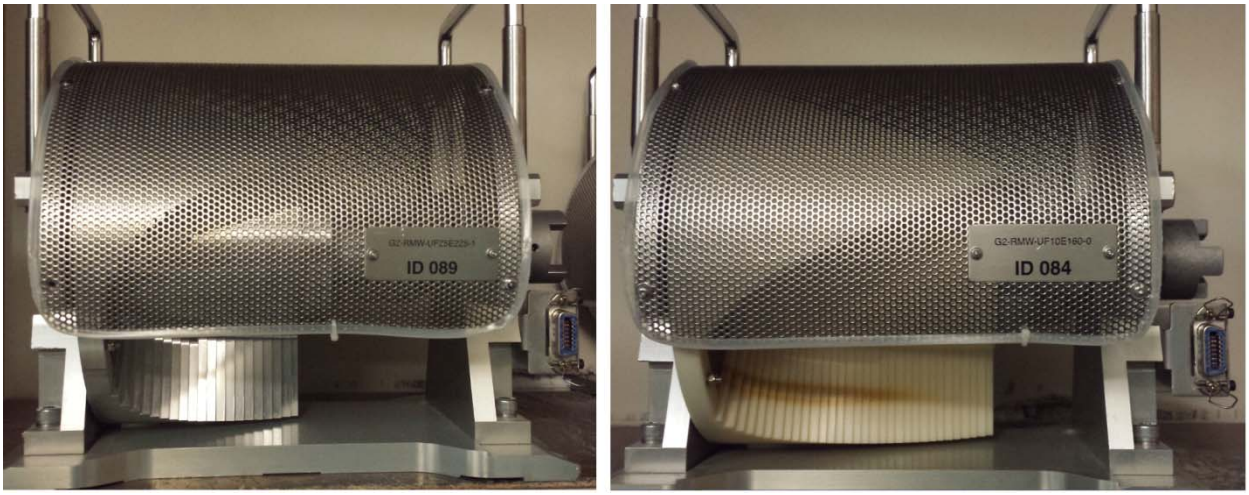

Figure 1-5: Passive scattering range modulators

One area of concern in passive scattering systems is stray radiation. Unwanted dose delivered to healthy tissues is produced both within the patient himself, which is unavoidable regardless of the treatment method, and in the structural components of the accelerator. Passively scattered proton therapy (PSPT) contributes with a non-negligible amount of neutron dose to the patient that leaks out of the treatment head [39]. Neutrons have an enhanced RBE compared to protons [40], and even reasonably small doses increase the risk

of secondary cancers [41]. Leakage neutron dose delivered to patients can be reduced by using scanning beams instead of passively scattered beams [42].

1.3.3.2 Pencil Beam Scanning

Pencil beam scanning, also known as spot scanning, magnetically scans a narrow beam of protons placing the Bragg peaks within the voxels of a three dimensional grid. There have been studies that suggest that spot-scanned proton beams offer the most advantageous therapeutic ratio over scattered proton beams [43]. This method generates treatment fields of any size and shape without the use of custom designed apertures, scattering foils or physical range compensators [35]. This is an advantage because it decreases the degradation of the beam energy, loss of treatment range and the neutron contamination discussed in the previous section, 1.3.3.1. Therefore, treatment plans control the delivery of dose simply as a function of beam intensity, depth, field size, beam positioning, and direction, which can be fully optimized with the use of intensity-modulated proton therapy (IMPT) [35].

Intensity-modulated proton therapy, analogous to IMRT for photon therapy, allows for greater dosimetric optimization and for better sparing of adjacent organs at risk (OARs) [44]. The modality uses multiple ports with inhomogeneous proton fluence so that, when combined, they deliver a homogeneous dose distribution to the target, keeping the dose to the surrounding normal tissues acceptable. Both conventional and IMPT techniques are precise and efficient modes of proton beam delivery with the method of pencil beam scanning [35].

Protons offer a variety of advantages over photons. The use of protons in radiation therapy has become very popular because of its superior dose distribution characteristics that allows for high doses to be delivered to targets and lower doses to be delivered to surrounding healthy tissues distal to the target, potentially resulting in increased tumor control and lower

normal tissue toxicities. When compared to photons, protons scatter less in the patient due to their smaller scattering angles, as consequence of their heavier masses. Another key advantage of protons is the steep dose fall-off at the end of their range. The dose depth distribution for a proton beam is characterized by the phenomenon known as the Bragg peak. This property of proton beams in tissue, where they quickly stop after the Bragg peak, brings the obvious advantage of not depositing any exit dose beyond a certain depth [35]. Figure 1.6 shows the depth dose distribution of a monoenergetic proton beam in comparison to a photon depth distribution.

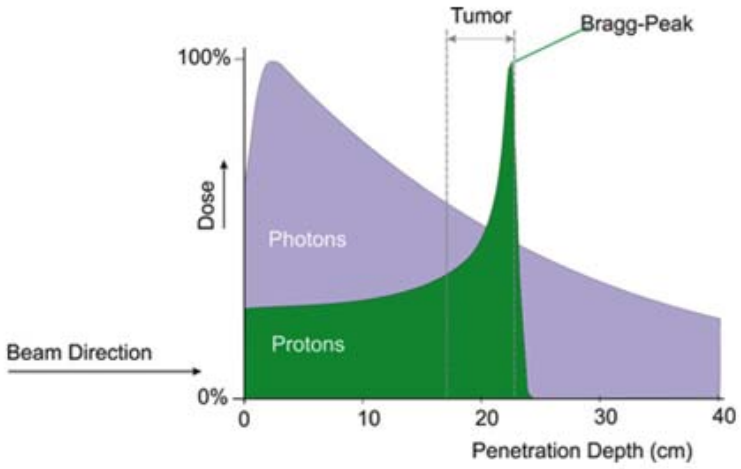

Figure 1-6: Depth dose distribution of a monoenergetic proton beam in comparison to a photon depth distribution

Taken from: http://www.p-cure.com/Why_Proton_Overivew.html

As it can be seen in Figure 1.6, the monoenergetic proton beam cannot cover the full extent of most tumors. The Bragg Peak phenomenon is a function of the energy of the each beam and by varying the energy of a proton beam with a range modulator or at the synchrotron, a compilation of pristine Bragg Peaks can be created to form what is known as the Spread Out Bragg peak (SOBP), shown in Figure 1.7.

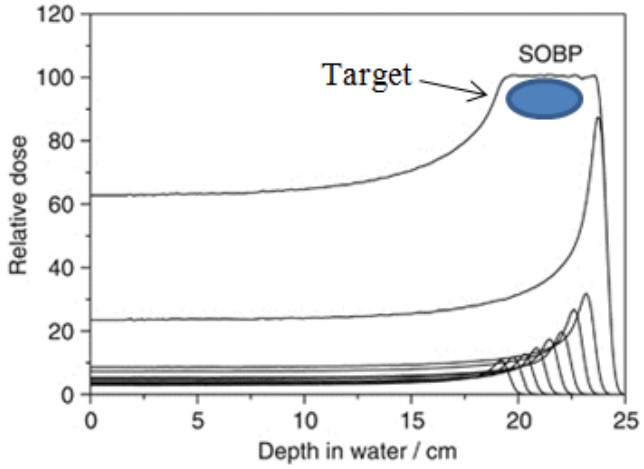

Figure 1-7: Compilation of pristine Bragg Peaks forming the Spread Out Bragg peak (SOBP) to cover the target

Taken from: http://archive.ahrq.gov/news/events/conference/2010/trikalinos/index.html

The spread out Bragg peak is originated by the superposition of different monoenergetic beams, and it allows for a better coverage of larger targets. Despite the advantages, one concern with the use of SOBP beams is that the entrance dose in the medium is significantly increased.

1.3.4 Relative Biological Effectiveness

Protons also show radiobiological advantages when compared to photons or electrons. The relative biological effectiveness (RBE) represents an assessment of the damage caused by the different types of radiation. This RBE comparison is established by dividing the dose of a given reference type of radiation, typically Cobalt-60 or 250 kVp x-rays, by the dose delivered by any type of radiation in order to obtain the same biological effect, shown in Equation 4 [35]:

$$\mathbf{RBE} = \frac{\mathbf{Dose}_{\mathbf{reference\ radiation}}}{\mathbf{Dose}_{\mathbf{test\ radiation}}} \qquad \textbf{Equation 4}$$

Relative biological effectiveness depends on the type and quality of the radiation, the actual biological endpoint considered, dose fractionation, and most significantly, the linear energy transfer (LET) of the radiation. In general, RBE increases with LET, and because charged particles have a higher LET, they also have a higher RBE. On the same note, the LET of a charged particle increases as the particle slows down, and thus, the RBE is greater in the Bragg peak region [35]. The proton radiation therapy community has adopted an average RBE value for protons to be 1.1. Paganetti [45] presented data for a large number of proton biological studies and compiled all of the calculated proton RBEs resulting in the average value of 1.1. In essence, this means that the final biological endpoint produced by protons can be the same as photons, but with 10% lower proton physical dose [35].

1.4 Dose Uncertainties in Proton Therapy

The main advantage of proton therapy treatments comes from the concept that the integral dose deposited on a patient for a given tumor is always lower than when compared to other modalities, mostly due to the lower exit dose. However, the great potential of proton therapy can only be optimized if the range of these protons can be predicted accurately when generating a treatment plan [46]. The range in tissue can be affected by uncertainties existent in the treatment plans such as, patient set up, imaging, beam delivery, dose calculations, organ motion, anatomical variations, or other biological considerations [46]. Poor calculations of the particle's physical range can translate to erroneous treatments that could overdose the healthy tissues or even under dose the tumor. In order to account for these potential deviations, MD Anderson Proton Therapy Center in Houston applies a correction in the proton beam range of 2.5% of the range plus an additional 2 mm for H&N sites.

With the increase in interest in proton therapy and with the many opportunities for inaccuracies in treatment delivery, the need for a QA program that can evaluate these treatments is evident. The phantom created for this project was designed to simulate a human head and neck. However, some of the inherent complexities and uncertainties of the human body that occur in real patients are not present in the phantom, for instance, organ motion and anatomical variations through the course of treatment.

1.5 Hypothesis

An anthropomorphic H&N phantom can be designed and built to evaluate proton therapy H&N treatment procedures that can reproducibly (±3%) assure agreement between the measured doses and calculated doses to within ±7%/4mm. In order to verify the hypothesis, the following aims were established for this project:

1. Design an anthropomorphic H&N phantom that can mimic human structures and disease with tissue equivalent materials for an oropharyngeal cancer.

2. Image the H&N phantom with CT and create clinically relevant treatment plans for passive scattering and spot scanning.

3. Irradiate the phantom 3 times with each treatment plan created and measure the delivered dose distribution and the dose to specific points (targets and normal tissues) within the phantom.

4. Compare the measured and calculated proton doses and distributions to determine agreement and precision.

1.6 Research Approach

Methodology:

1. The phantom will be designed based on the composition, size and geometry of a generalized head and neck tumor (oropharyngeal) and critical structures, such as the parotids and the spinal cord.

2. CT images will be obtained for the phantom and two treatment plans (passive scatter and spot scanning) will be developed using the Eclipse proton planning system. The plan, approved by a radiation oncologist, will be developed based on typical clinical constraints for a generalized H&N cancer adopted at the Proton Therapy Center – Houston.

3. Radiochromic film and TLD capsules will be placed in the phantom through a cylindrical insert. The phantom will be irradiated 3 separate times for each approved treatment plan in order to evaluate the reproducibility of the phantom design.

4. The 2D dose distributions and specific point doses determined from the film and TLDs will be compared with the planning system calculated values, dose profiles and dose distributions to determine the agreement and reproducibility.

2 Materials and Methods

2.1 The Anthropomorphic Head and Neck Phantom

2.1.1 Phantom Design Considerations

In order to remotely evaluate the planning and dose delivery of these treatments, IROC Houston has creatively designed and built a number of different heterogeneous mailable anthropomorphic QA phantoms. One aspect that all of these phantoms have in common is that they all try to simulate the true human anatomy in some way. Some of the phantoms consist simply of plastics shells that can be filled with water, and others can be more complex, mimicking the lung motion of an actual patient. One important characteristic of the design is to include tissue heterogeneities in order to properly account for the clinically relevant anatomical heterogeneities and to be able to image different structures (targets vs. critical structures). Another important consideration for this project is the human anatomy typically involved in head and neck malignancies. The complexity of head and neck cancer is due not only to the large extent and involvement of typical malignancies, but also to the large number of critical structures surrounding or adjacent to the target, such as, the parotid glands, oral cavity, esophagus, larynx, mandible and teeth, eyes and spinal cord. Therefore, in order for radiation treatments to be successful, not only do the prescribed target doses need to be delivered uniformly throughout the tumor but also critical structures constraints need to be respected. Typical dose-volume constraints used at MD Anderson Cancer Center for proton therapy treatments are shown in Table 1.

OAR	Dose	Volume
Parotids	26 Gy	Mean
Cord	45 Gy	Max
Mandible	70 Gy	Max
Cochlea	35 Gy	Max
Lens	5 Gy	Max
Larynx	25 Gy	Mean
Brainstem	45 Gy	Max
Esophagus	25 Gy	Mean

Table 1: Dose-volume constraints used in typical head and neck proton treatments

2.1.2 Determination of Tissue Equivalent Materials for Proton Therapy

IROC Houston currently has a variety of anthropomorphic phantoms that are used in their remote auditing QA programs, including a Head and Neck photon phantom. However, the need for the construction of a proton Head and Neck phantom can be justified based on the requirement for these materials to be tissue equivalent for proton therapy. Materials that can be considered tissue equivalent for photon beams may not necessary be tissue equivalent for proton beams. The relative linear stopping power (RLSP) should be used in order to determine the tissue equivalency of materials to be exposed to proton beams, as the electron density information is used for photons. Proton treatment planning systems rely on the relationship between Hounsfield units and RLSP instead of electron density [47]. Figure 2.1 shows the curve, RLSP versus Hounsfield units, used to determine proton equivalent materials.

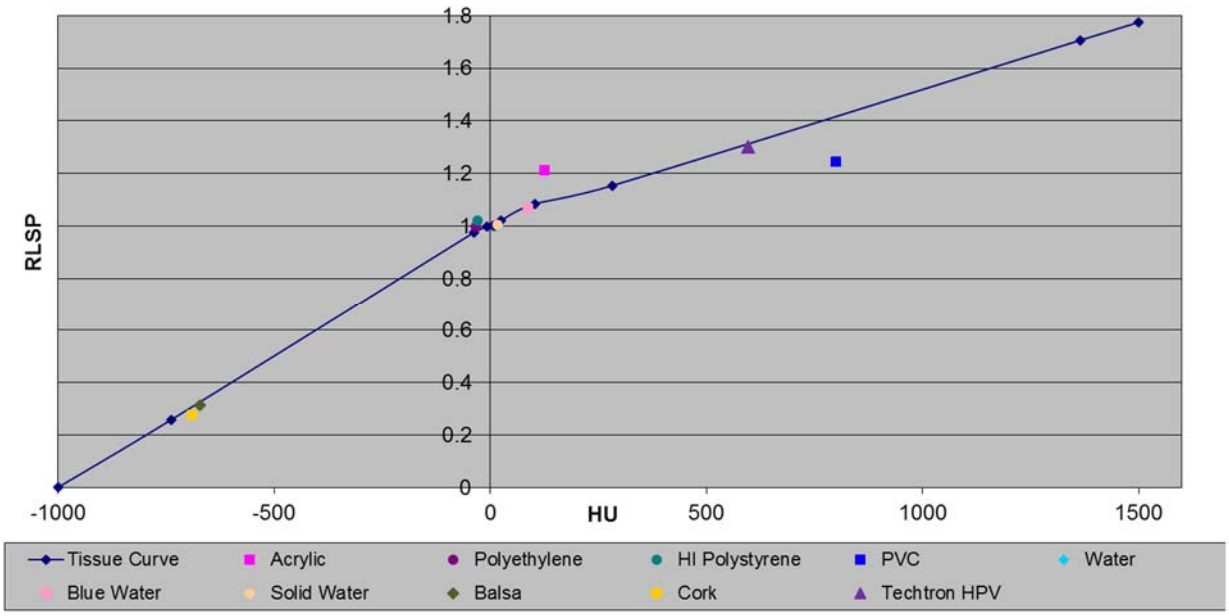

Figure 2-1: Relative Linear Stopping Power versus Hounsfield Units curve used to determine proton equivalent materials

Materials that lay on the curve in Figure 2.1 are considered proton tissue equivalent materials, where a percent difference of less than 5% in the RLSP is the cutoff for materials suitable for proton therapy [47]. For instance, blue water and solid water are materials that will behave like human tissue when exposed to a proton beam, while acrylic, a photon equivalent material, will not.

One interesting note related to the first insert design is that polyethylene and blue water were used as the materials for the target and critical structures. However, according to recent literature, polyethylene demonstrates slight variations in stopping power for different proton treatment energies [48]. As a result, the final composition of the cylinder was solid water and blue water for the structures inside. The evident need for different materials was justified in order to allow for a clear visualization of the structures in the CT scans, and consequently the success of the proton treatment planning.

2.2 Image Acquisition

The phantom was scanned with the MD Anderson Proton Therapy Center of Houston's CT scanner, a GE LightSpeed RT16. A typical head and neck protocol was used to image the phantom, with 1.25 mm slices at 120 kVp. In addition, the scan was done in helical mode with a pitch of 0.9375.

In order to assure reproducibility, the phantom was placed in the supine position, on a Klarity^{TM} mold that was shaped to the Head & Neck phantom. The mold also guaranteed that air gaps were minimized in the scan. Small pieces of tape with cross marks were place on the sides, forehead and neck of the phantom, in the interest of using the room lasers to follow the correct alignment during treatment setups. Actual patients require other features in order to guarantee precise setup up, such as Head & Neck masks, specialized head rests and bite blocks. However, due to the inanimate nature of the phantom, those did not need to be employed. Figure 2.2 shows the phantom resting on the Klarity^{TM} mold with the laser tags taped on the surface.

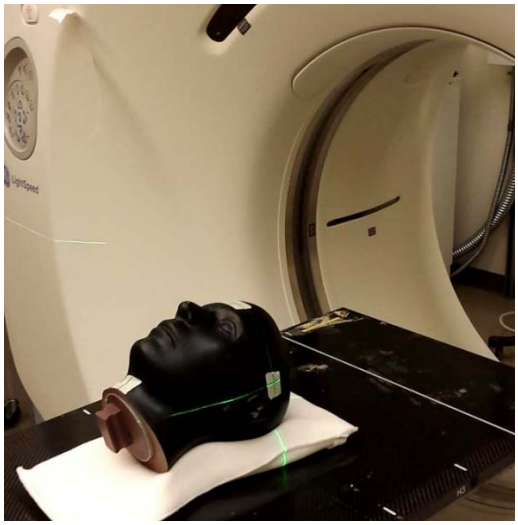

Figure 2-2: Head & Neck phantom resting on Klarity mold with laser tags taped on the surface

2.3 Treatment Planning

Treatment planning considerations were made following the recommendations of the MD Anderson Proton Therapy Center (PTC) of Houston. The typical Head and Neck dose prescription employed at the PTC is delivered in dose gradients, with the goal of hitting the target while minimizing the dose to the surrounding healthy tissue. For this research study, the gross target volume (GTV) was considered to be the clinical tumor volume (CTV), however that is not clinically implemented since the extent of the microscopic disease is not exactly known. Standard guidelines used at the PTC aim to deliver the prescription in 33 fractions as following; 70 Gy to the primary target, 63 Gy to high risk lymph nodes and 57 Gy to additional risk nodal areas. Optimal plans are usually achieved with the use of posterior beams and/or anterior oblique ones. One main reason why these are popular beam arrangements options is because of the large number of critical structures in the anterior part of the head and neck region, such as mandible, teeth, tongue and eyes. Another particularly relevant reason is related to the oral and nasal cavities. These areas will not only change the range of the proton beam due to the absence of actual tissue, but will also transform during the course of treatment, filling and empting with nasal mucus.

The CT scan was performed on a regular couch, which as a consequence, required the insertion of a digital couch into the treatment planning system, in order to account correctly for the posterior proton beam ranges. Another necessary step for the correct calculation of the proton ranges was the CT number override of the imaging artifacts caused by the pin pricks and screws present in the insert. The artifact areas were also contoured and given the real tissue-like (solid water, in the case of the cylinder) Hounsfield unit number.

Although typical treatment doses for Head and Neck cancer are on the order of 70 Gy, the IROC protocol requires the prescription to be a factor of approximately 10 times smaller. Consequently, the primary CTV was planned to have 6 Gy delivered in one fraction. The reason behind lowering of the dose delivered is related to the fact that the total absorbed dose affects the film response to ionizing radiation. IROC uses Gafchromic EBT2 film and it saturates at doses of around 10 Gy [49].

The treatment plan was generated with the assistance of a dosimetrist and an experienced medical physicist member of my committee. The plan was based on typical clinical dose constraints of 26 Gy for the parotids and 45 Gy to the spinal cord. However, it is important to note that these constraints were also scaled according to the target dose and were accepted to be 2.6 Gy and 4.5 Gy respectively.

2.3.1 Spot Scanning Treatment Plan

A spot scanning treatment plan was generated for the target using the prescribed dose of 6 Gy normalized to 100% of the PTV. The optimal dose coverage with best tissue sparing was achieved with the use of one posterior beam, and two anterior oblique ones. Additional plan parameters employed are listed in Table 2. Figure 2.3 and Figure 2.4 show screenshots of axial and sagittal slices of the treatment isodose lines respectively. Figure 2.5 shows the Dose volume histogram (DVH) of the spot scanning plan.

Spot Scanning Treatment Plan Parameters			
Prescription: 6 Gy			
	Beams		
	Posterior	**Anterior Left**	**Anterior Right**
Gantry Angle [deg]	180	65	295
Couch Angle [deg]	0	340	20
Field Weight	1	1	1
MU	135.94	131.90	114.45

Table 2: Spot scanning treatment plan parameters

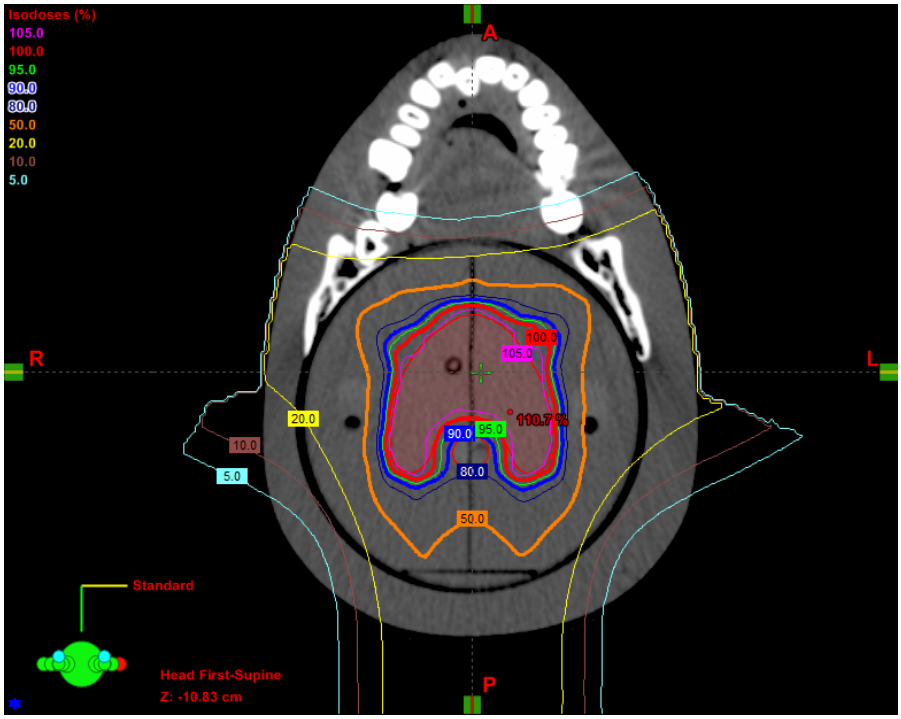

Figure 2-3: Spot scanning treatment plan shown in the axial plane

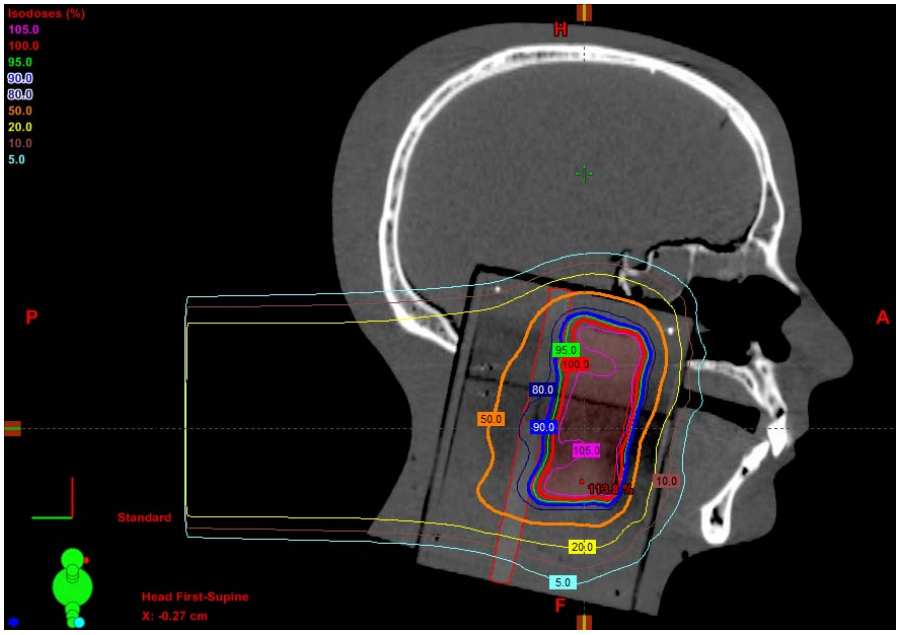

Figure 2-4: Spot scanning treatment plan shown in the sagittal plane

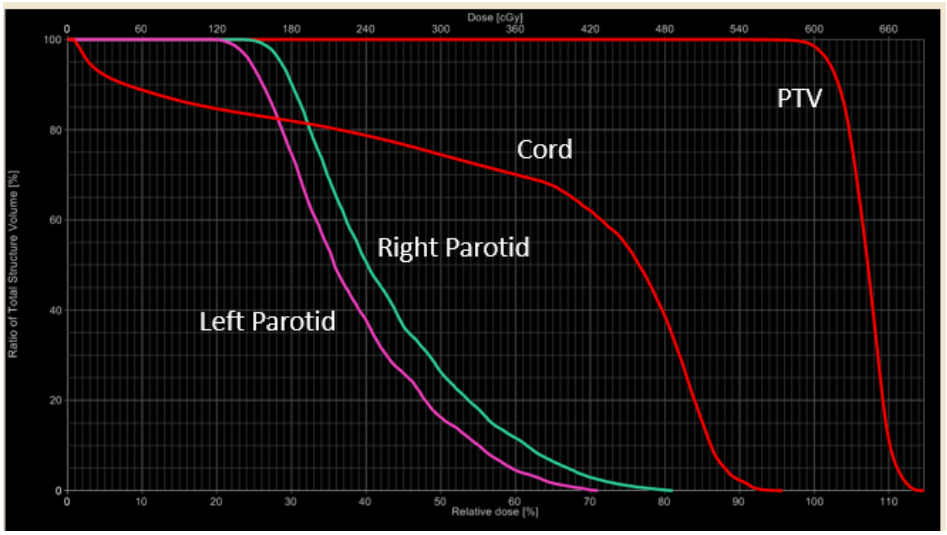

Figure 2-5: DVH of spot scanning beam treatment plan with PTV, cord and parotids

According to the plan, the PTV would receive adequate dose coverage where 96.7% of the volume would be given 100% of the dose. The parotids were under the acceptable dose constrains. The mean dose delivered to the left and right parotids were, 2.59 Gy and 2.30 Gy

respectively, meeting the 2.6 Gy limitation. The cord received a mean dose of 3.77 Gy but a maximum dose of 5.7 Gy, which exceeded the 4.5 Gy maximum dose restriction. This compromise had to occur because of the unrealistic anatomic fit of the structures in the insert. In normal human anatomy, the parotids and cord are more superficial than the phantom insert allowed for. The insert could not have been wider because it had to fit though the neck while still allowing for enough material to support the head. Therefore, a higher than clinically advisable dose was delivered to the cord in order to maintain target coverage.

2.3.2 Passive Scatter Treatment Plan

A passive scattering treatment plan was generated with two AP PA beams with the efforts of achieving tumor control. Figure 2.6 shows a 3D view of the proton beams and the custom 6 cm thick brass blocks designed. The brass blocks were designed to fit to the target structure and were edited to provide some shielding to the parotids as seen in Figure 2.7. Plexi glass compensators were also added to the plan in order to account for patient irregularities, PTV surfaces and tissue heterogeneity.

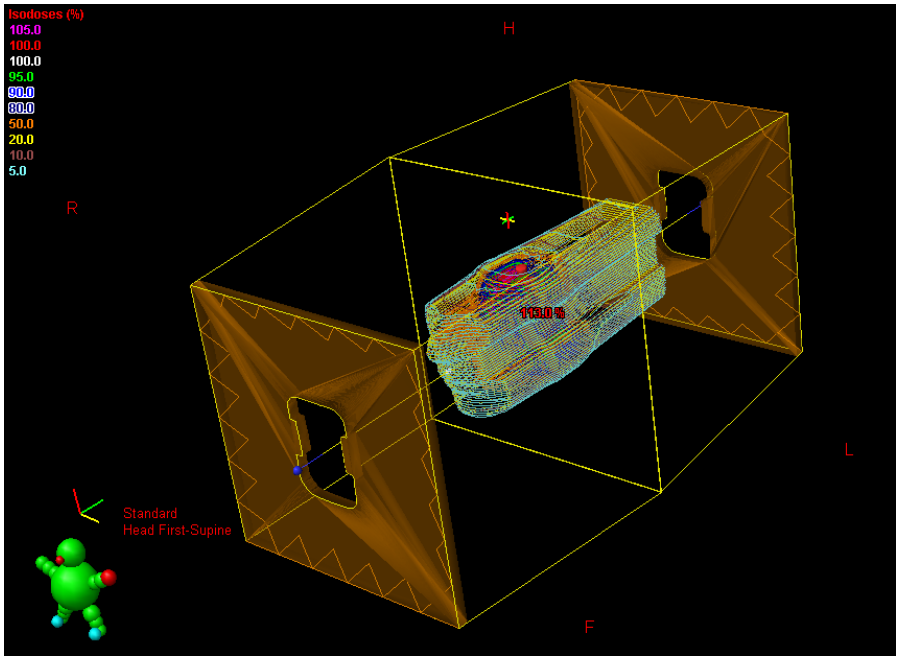

Figure 2-6: 3D view of the AP PA proton beams through brass blocks

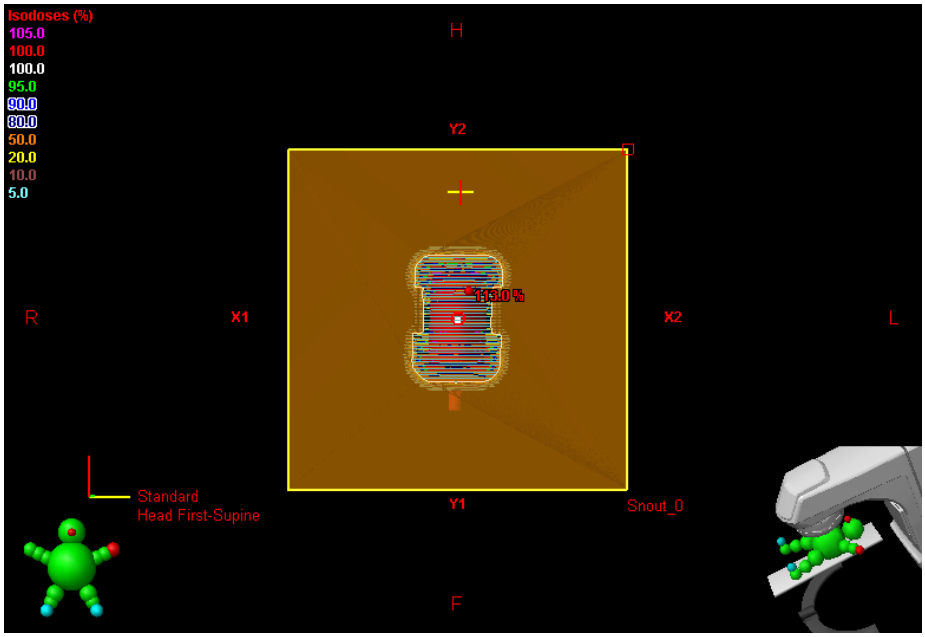

Figure 2-7: Beam's eye view of the brass block fit to target structure with indentations protecting parotids

The passive scattering plan offered great sparing of the parotids but unreasonably high doses to the cord. In addition, the target coverage was insufficient, offering numerous hotspots and poor uniformity, as it can be seen in Figure 2.8 and Figure 2.9. In the axial view, it is possible to notice how the 100% isodose line is not well conformed to the target presenting high tissue toxicity to the surroundings tissues, as well as the OARs designed in the phantom. It is also apparent in the axial image that there is a large area of the tumor that is not covered by the 100% isodose line, leaving great portion of the GTV under dosed.

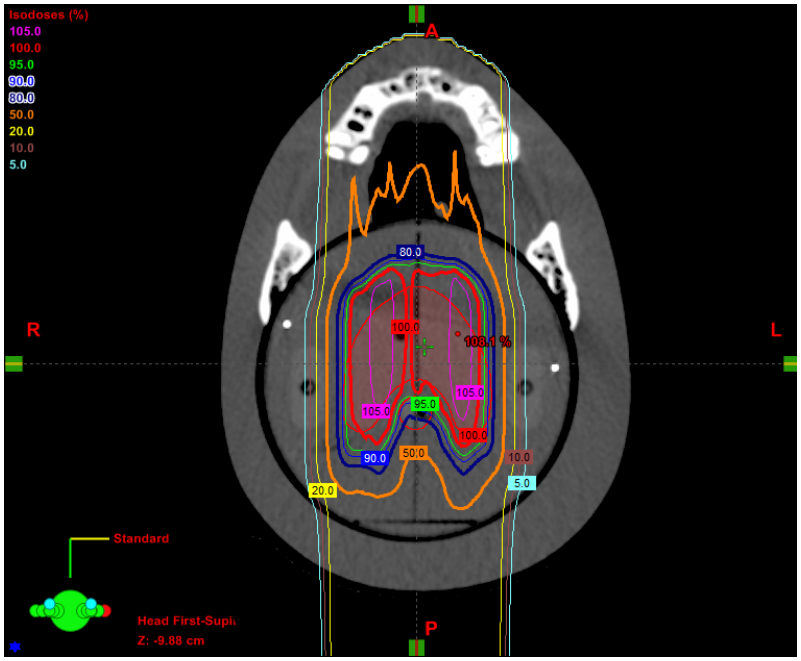

Figure 2-8: Axial view of isodose lines of passive scattering plan

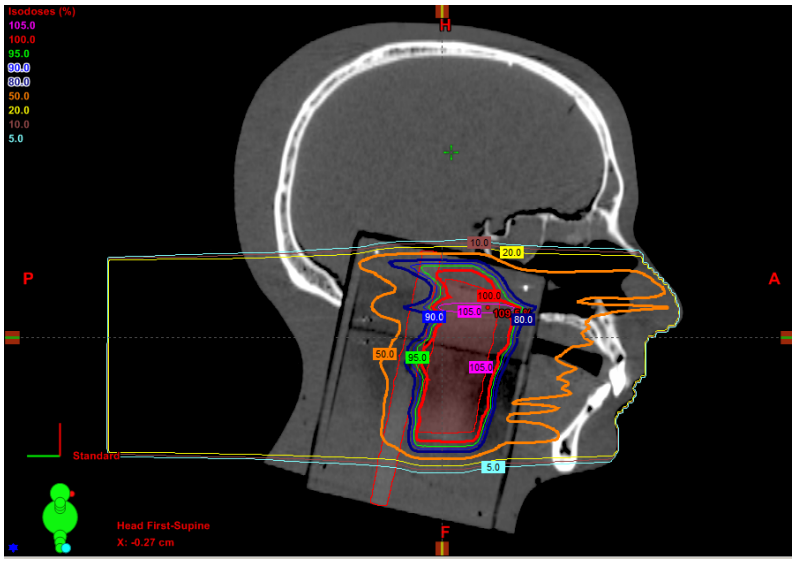

Figure 2-9: Sagittal view of isodose lines of passive scattering plan

The impracticality of the plan can be analyzed further through the DVH created by the TPS in Figure 2.10. The parotids were both well under the dose constraints considered for the plan, 0.76 Gy for the left and 0.96 Gy for the right parotid. However the cord got a maximum dose that was equivalent to the total prescribed target dose of 6.02 Gy. Aside from the enormous cord toxicity, it is possible to confirm again though the DVH that not all of the target was covered and there were a large number of hotspots, totaling the maximum target dose to 6.78 Gy.

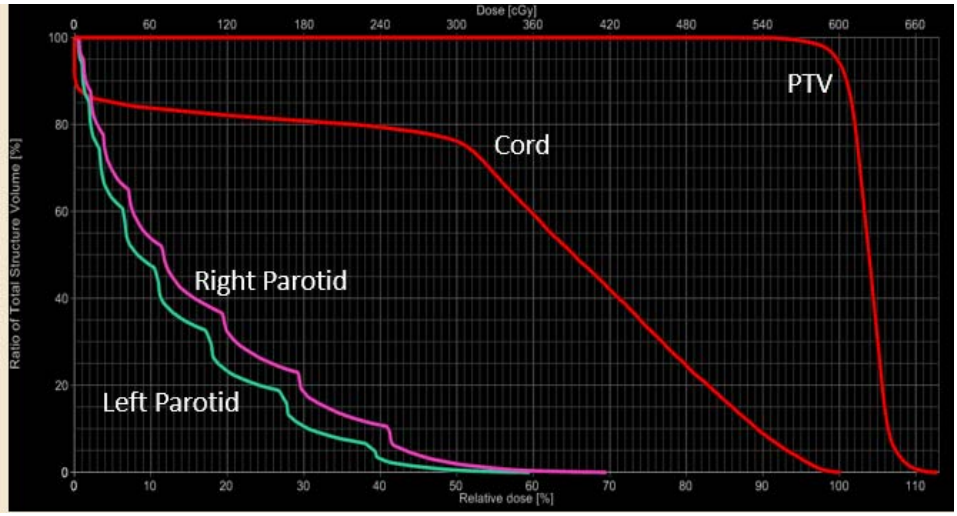

Figure 2-10: DVH of passive scattering beam treatment plan with PTV, cord and parotids

2.4 Treatment Delivery

All irradiations trials were performed on the G3 spot scanning beam gantry at the PTC-H. The phantom was placed in the supine position and aligned with the gantry lasers and x-ray imaging. The AP and lateral kV images were then compared with the DRRs generated in the TPS. The imaging parameters used for the setup were the same as the ones recommended for head and neck patients treated at the PTC and are shown in Table 3.

Orientation	AP	Lateral
kVp	60	70
mA	320	400
ms	50	63

Table 3: Imaging parameters used in the alignment

Once one complete treatment was delivered to the phantom, dosimeters were unloaded and new unirradiated TLDs and film were reloaded. A new set of x-rays were acquired before the subsequent trials in order to ascertain the best positioning. Figure 2.11 shows the three different positions of the gantry for the beams used to deliver the treatment.

Figure 2-11: From left to right; posterior beam, right oblique beam and left oblique beam

2.5 Dosimetry

2.5.1 Planar Dosimetry

2.5.1.1 Film

Gafchromic EBT2 film (Ashland , Wayne, New Jersey), was used in order to perform the analysis of the sagittal and axial dose distributions of the irradiations. Radiochromic film was considered the appropriate relative dosimeter for the study of the dose profiles due to the fact that it shows no angular dependence, is near tissue equivalent and IROC-H has the infrastructure to analyze it precisely and accurately. In addition, it offers sensitivity (0.1 to 10 Gy) in the required range for this project (6 Gy), and has great spatial resolution. It can also be handled in visible light and is self-developing [49, 50], making this passive detector very suitable for the remote quality programs established at IROC. EBT2 films from lot number

08131501 and an expiration date of August 2017 were used for this study. Figure 2.12 shows the cross section of the Gafchromic EBT2 components [51].

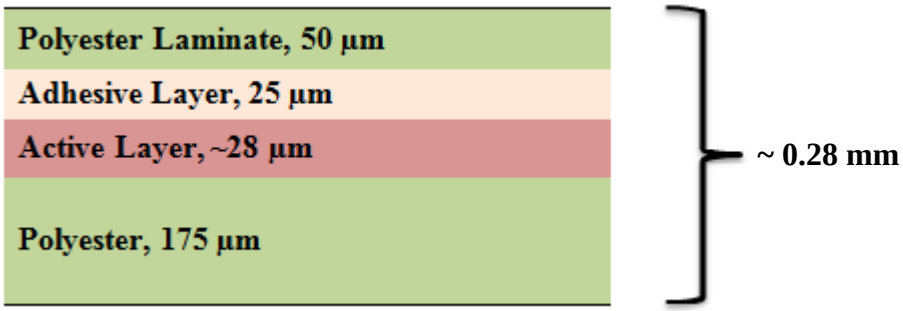

Figure 2-12: Diagram of cross section of the Gafchromic EBT2 components

2.5.1.2 Film Calibration

A film calibration needs to be established to determine the accurate relationship between the intensity of the film and the dose delivered. The same procedure was performed using a passive scatter irradiation technique at the PTC-H for all the irradiated film. A medium size aperture block was used. At 160 MeV, the SOBP was 10 cm and therefore required 8 cm of acrylic buildup above and below the film. The center of the film was set at 270 cm source to axis distance (SAD). The film was cut into sections of 5 x 10 cm^2 and the MU used for each dose level was calculated using Equation 5 and can be seen in Table 4. The range shift factor and the SOBP output factor was 1 for the 10 cm SOBP, while the relative output factor was given to be 0.792.

Equation 5

$$MU = \frac{Physical\ Dose}{Relative\ Output\ Factor * SOBP\ Output\ Factor * Range\ Shift\ Factor}$$

Dose (Gy)	MU
0.5	62.73
1	126.2
2	252.5
3	378.7
4	505
5	631.3
6	757.5
7	883.8
8	1010.1

Table 4: MU required for each dose used in film calibration

The doses shown above are physical doses and therefore did not take into account the proton RBE. The RBE was not taken into account in these MU calculations because the dose distribution analyzed later in the film was normalized to the TLD doses, which involved the 1.1 correction.

The film was scanned using a SBIG CCD Camera, model STF 8300M. The dose versus intensity curve was plotted and a third degree polynomial was fit to it, shown in Figure 2.13. The coefficients obtained from the fit were later inserted into the IROC software in order to proceed with the analysis and convert the film intensity to dose. To ensure the correct orientation for all the tests, the pieces of films were marked with reference points on the edges. The read out was performed at least 24 hours after the irradiations to allow the film to stabilize and assure accurate measurements [51].

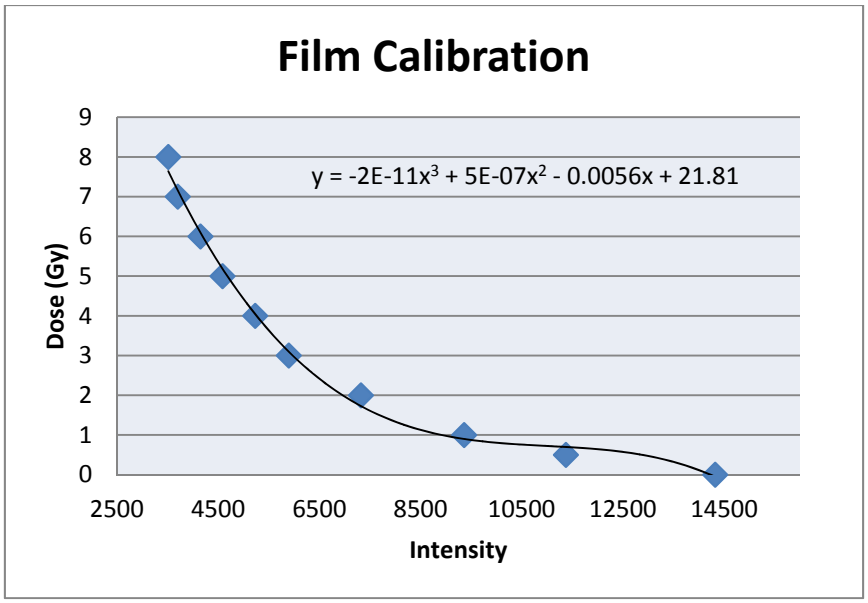

Figure 2-13: Film calibration curve and fitted equation for EBT2 lot 08131501 for proton beam

2.5.2 Point Dosimetry

2.5.2.1 TLD

Thermoluminescent dosimeters (TLDs) were used as point dosimeters in the phantom providing absolute dose measurements at the specific locations where they were positioned, such as target and OARs. TLDs are passive detectors made of LiF crystals filled with impurities that create imperfections in the lattice of the material, also called energy traps. Once irradiated, electrons from the ground state can receive sufficient energy to be raised to the conduction band and get trapped in crystal lattice. These electrons can be released through a heating process and emit visible light [35]. The amount of TL light emitted is proportional to the dose delivered, and can be finally detected with a photomultiplier tube.

TLDs carry a valuable set of advantages in this project because they display a wide useful linear dose range (10E-5 – 10 Gy), and are dose rate independent [35]. In addition, TLDs are also small in size, not disturbing the radiation field, and are accurate and reusable. One important consideration is that TLDs require an annealing process in order to remove residual radiation. The detector response is affected by the previous radiation and heating history. Therefore a standard annealing process needs to be completed before the subsequent irradiation. This standard procedure is well known by IROC and was applied to assure reliable collection of measurements.

There are several necessary parameters in order to calculate the final dose delivered to a powder TLD and they are shown in Equation 6. The first term in represents the thermoluminescent signal per unit mass, $C_{D,w}$ is calibration factor, k_F is the fading correction, k_E is the energy correction (unity for proton beams) and k_L is the linearity correction.

$$\boldsymbol{D = M_{raw} * C_{D,w} * k_F * k_E * k_L} \qquad \textbf{Equation 6}$$

The M reading is normalized by the powder mass so that any mass differences between the TLDs did not affect the calculation. The TL signal was given in nC and the powder mass in mg. Similar to $N_{D,w}$ for ion chambers, the calibration factor $C_{D,w}$ is responsible for the conversion to dose, taking into account the different system sensitivity between the different TLD batches and any variation between readout sessions. The fading correction factor is necessary because trapped electrons will occasionally exit their excited states, resulting on the fading of the signal over time. The fading correction can be calculated using a double exponential modeled of the curve obtained from the readout percent signal versus time, and is shown in Equation 7:

$$k_F = \frac{N}{ae^{-bt} + ce^{-dt}} \qquad \textbf{Equation 7}$$

Where N, a, b, c, d are coefficients determined based on the TLD batch characterization performed by IROC and t is days from irradiation. For the lowest possible fading correction, the TLDs should be read a minimum of 14 days after the irradiation.

A linear correction is also needed since TLD responses are not perfectly linear. Equation 8 is used by IROC to calculate the linear correction factor, where e and f are batch specific coefficients.

$$k_L = \left(M_{raw} * C_{D,w} * k_F\right) * e + f \qquad \textbf{Equation 8}$$

One important aspect about the correction factors is that they all have to be established for a specific batch of TLDs, since they can all vary slightly between batches. Double loaded LiF TLD-100 dosimeters (Quantaflux, LLC, Dayton, OH) were used for each irradiation. The TLDs were read out 10 days after the irradiations and the physical dose obtained from them was multiplied by 1.1, the proton RBE, in order to obtain the equivalent absorbed dose.

2.5.2.2 TLD Characterization

TLD calibration is done by irradiating a set of standard dosimeters to a known dose of radiation and establishing the correction factors needed. The standards were irradiated to a known dose of 300 cGy by a ^{60}Co machine. This characterization was done by the IROC prior to irradiation and the correction factors obtained are tabulated below. The standards used were of the same batch of TLD powder and therefore their previous calibration was valid to be used in this project.

Corrections Factors	Value
N	1.3493
a	1.2815
b	0.0001
c	0.0678
d	0.0719
e	-0.0003
f	1.1005

Table 5: Fading and Linearity Correction Factors

2.6 Dosimetric Analysis

2.6.1 CT, Film and TLD

IROC Houston uses a software developed internally, RCPFilm, to register the CT images and dose distribution with the TLD and film locations. The phantom insert contained pin pricks of known locations that would prick the film once loaded. The pin pricks were used to spatially orient the film with respect to the planned CT data. This was done by using an isocenter located in the target in the axial cut of the insert and measuring the physical distances to the pins. These distances were then inserted in the program and used as a coordinate system. Similarly, TLD distances are also imputed into the program and used as a 3D reference system for the program to spatially orient the CT images.

Once the film is correctly registered the calibration curve previously obtained is then applied to convert the film intensity values to dose. The TLD measurements obtained inside the target serve to scale the film dose. The TPS values are divided by the measured TLD values and that ratio is used to scale the final dose distribution obtained in the film. The reason

for this step is due to the fact that film only offers a relative dose measurement and therefore needs to be normalized by a reliable absolute dosimeter, such as TLDs.

2.6.2 Gamma Analysis

The agreement between the 2D dose distribution on the film and the one predicted by the TPS was analyzed using a gamma analysis procedure. The analysis can be performed by the same IROC in-house software using the properly registered film. Unwanted pixels are masked off and, therefore are not included in the analysis, such as pin pricks, pen marks and film gaps caused by the axial film. Figure 2.14 shows the sagittal film with the unwanted marks masked out. The IROC-H expects an 85% pixel passing rate for the gamma analysis; hence the same criterion was used for this study.

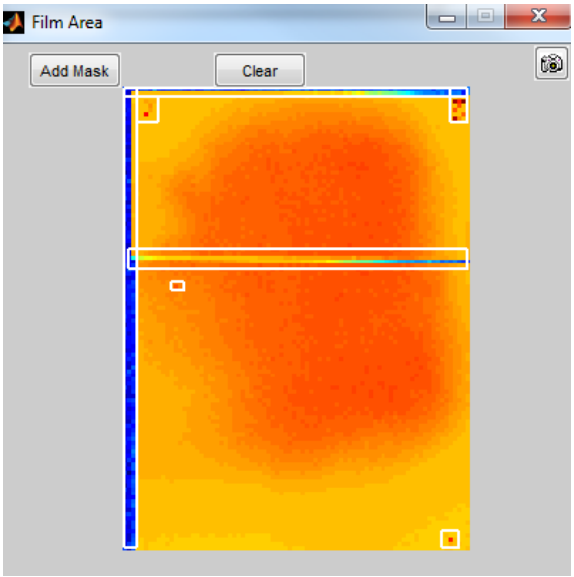

Figure 2-14: Sagittal film with the unwanted marks masked out

3 Results

3.1 The Anthropomorphic Head and Neck Phantom

3.1.1 Design and Construction

The head and neck (H&N) phantom created in this project is composed of tissue equivalent materials with real human bone and air gaps in the beam path. More specifically, the original phantom purchased was an Alderson phantom from The Phantom Laboratory (NY) made of Alderson water equivalent plastic with designed airway channels and a human skull inside to mimic actual human head anatomy. Figure 3.1 shows the head phantom purchased and Figure 3.2 illustrates the sagittal and axial CT scan of the original phantom showing the oral and sinus air cavities and human skull previously mentioned.

Figure 3-1: Alderson Head phantom

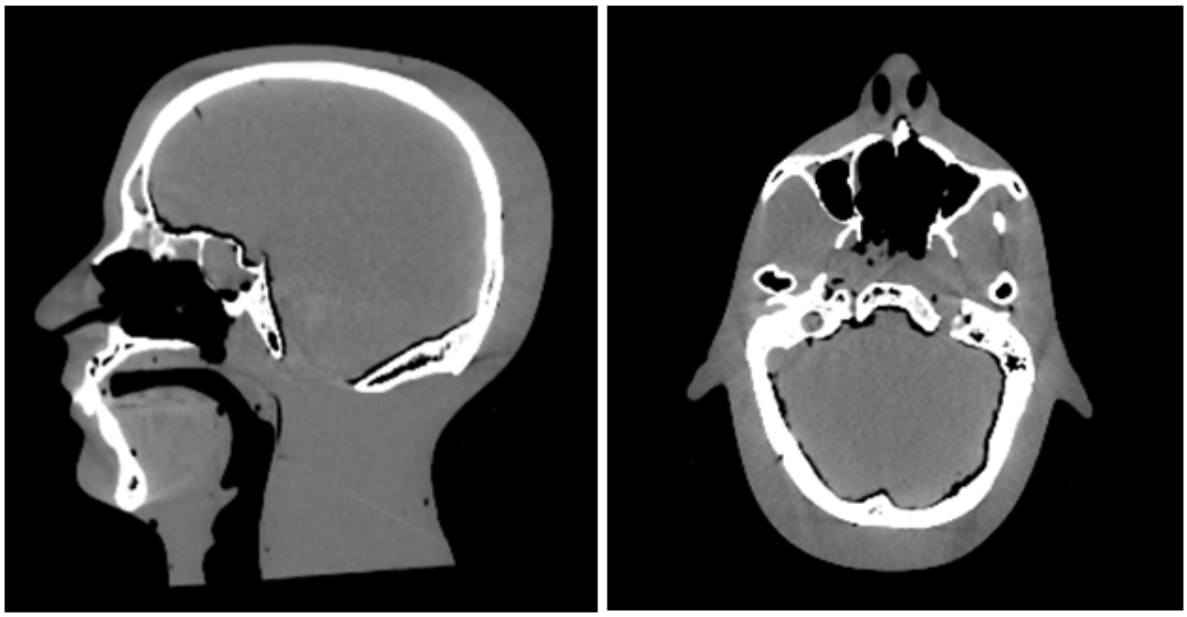

Figure 3-2: Sagittal and Axial CT scan of the original head phantom purchased prior to modifications

To be an appropriate quality assurance phantom for proton trials the head phantom had to include imageable targets and critical structures that mimicked human anatomical dimensions and the usual extent of oropharyngeal disease, while still accommodating radiation dosimeters. In order to facilitate the analysis of the dose profile and dose distribution a cylindrical insert containing all the relevant structures and dosimeters was designed based on actual patient anatomy. The insert design included a "horse shoe" shaped target that wrapped partially around the spinal cord and placed in the center of the insert, along with three relevant organs at risk, the spinal cord and two parotids placed laterally. The placement of the structures were such that proton beams would have to travel through bony structures as well as air cavities. As mentioned previously, the parotid structures had to be placed deeper than usual human anatomy because of physical limitations of the phantom, but their placement was adequate so as to not be unrealistic and still represent an oropharyngeal treatment. Therefore,

the maximum diameter allowed for the insert was 9.5 cm approximately. Figure 3.3 illustrates the 3D schematics of the design and Figure 3.4 shows the dimensions of each structure, where the spinal cord is 13 cm long, the target is 8 cm long and each parotid 3.5 cm long.

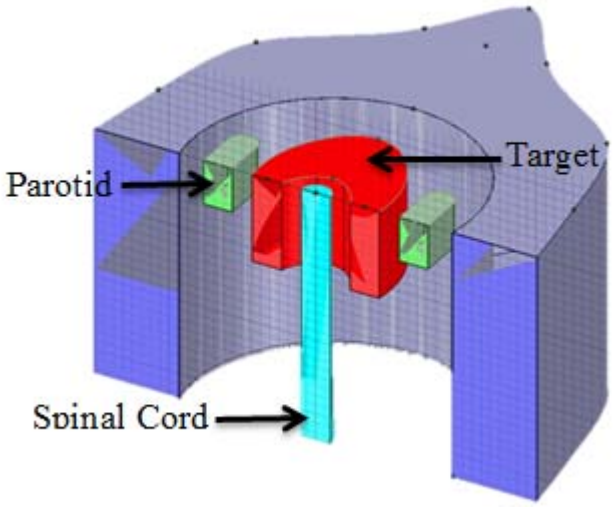

Figure 3-3: Schematics of the insert design

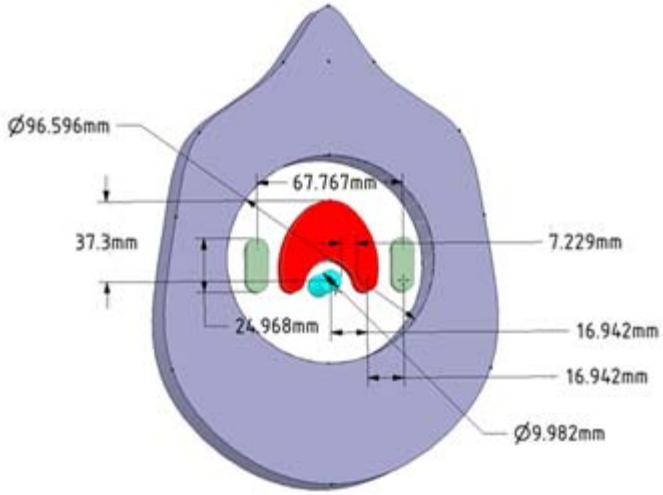

Figure 3-4: Dimensions of Structure and Separations

The insert was split into four pieces so that radiochromic film could be inserted in the axial and sagittal planes. In order to keep the pieces held tightly together and avoid any air

gaps, the four loose pieces of the insert are attached together using small 6-6 nylon screws and the whole cylinder is held secure by an external thin (2 mm) plastic sleeve made of polyethylene. The film is prevented from rotating or moving inside the phantom by small stainless steel pins that also serve to place registration marks on each film. Holes were created inside each relevant structure, one for each parotid and two for the target and spinal cord to hold TLD capsules, so that absolute dose measurements could be made in each structure. Figure 3.5 shows the insert that was constructed with and without the plastic sleeve and Figure 3.6 shows the sagittal and axial view of the cylindrical insert with the superior target TLD in place.

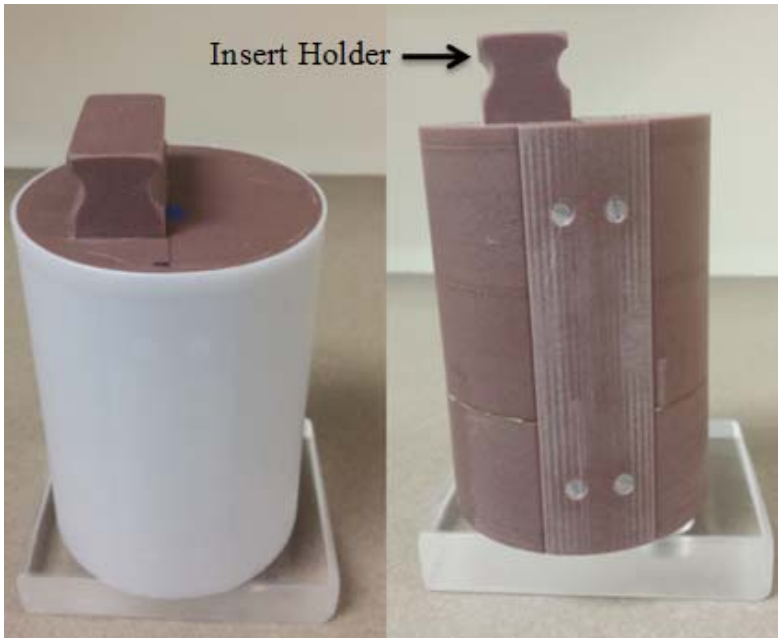

Figure 3-5: Insert with and without the sleeve cap

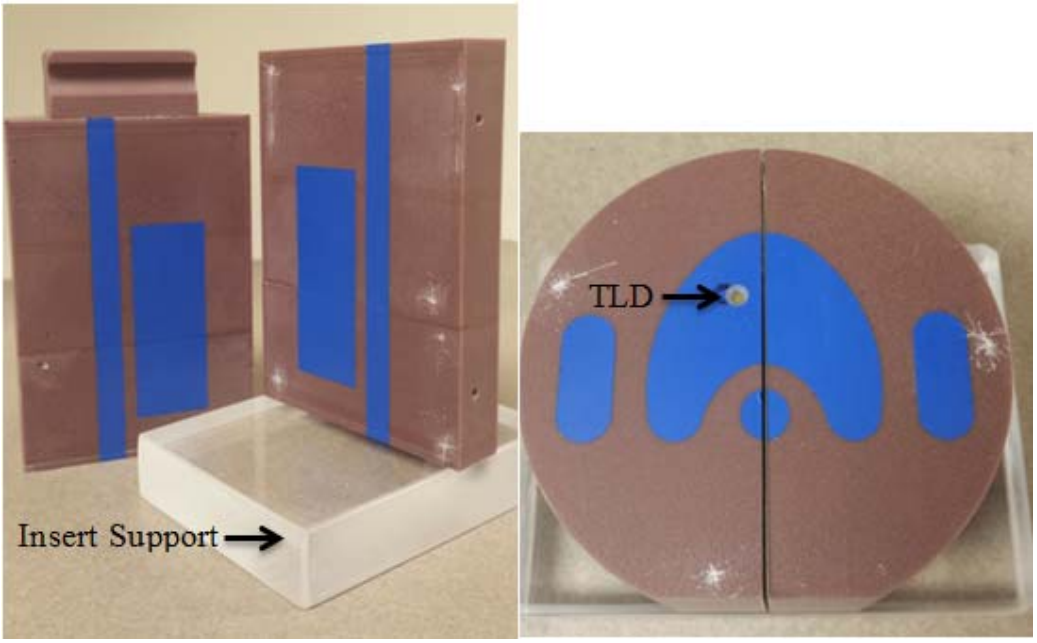

Figure 3-6: Sagittal and axial view of the cylinder insert

3.2 Passive Scattering Considerations

After multiple iterations, it was determined that a passive scattering treatment plan for an oropharyngeal proton treatment was clinically unrealistic and could not be delivered to the designed phantom. This was not surprising since the MD Anderson clinician developing the proton oropharyngeal clinical trial suspected that a viable clinical treatment could only be achieved using Intensity Modulated Proton Therapy (IMPT) with a pencil beam scanning technique. Yet an attempt to develop a passive scattering plan was made. It was determined that the structures (target, cord and parotids) chosen to be in the insert, based on actual patient anatomy, were too close together for the passive plan to successfully achieve the treatment plan goals outlined in the clinical trial. The parotids were sufficiently shielded but the spinal cord was not protected sufficiently resulting into a large a volume receiving the same dose as the target. Furthermore, the target coverage was compromised resulting significant non-

uniformity, with several cold and hot spots. Because of the clinical inappropriateness of the passive scattering plan the proton clinician responsible for approving the treatment plans for this project rejected it, and therefore the project moved on focused on the spot scanning treatments and no measurements were made with the H&N phantom.

3.3 Patient QA of the Phantom

The regular patient QA procedure performed in the PTC clinic was done on the phantom in order to check the treatment plan. Two sets of measurements were taken for every beam used in the pencil beam plan. Measurements were taken in shallow and deep depths, as shown in Figure 3.7 and Figure 3.8 respectively. The depths were chosen to be in regions with low doses gradients on the dose profiles inside the target. Both measurements were done using a MatriXX device with added solid water buildup to correctly place the measurements' depth on the active ion chamber region. The PTC uses a separate software to run a gamma analysis with a criteria of 3%,3mm. Table 6 shows the depths selected and the gamma analysis results. The full patient QA report can be found in the Appendix.

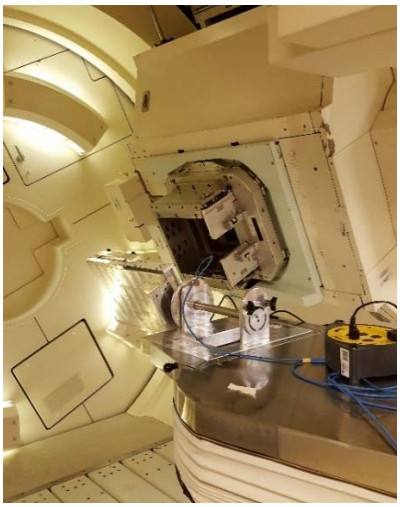

Figure 3-7: Shallow measurements set up using MatriXX IBA on a rotating device

Figure 3-8: Shallow measurements set up using MatriXX IBA on treatment couch

Beam	Depth (cm)	Gamma Index (3%,3mm)
Posterior	5.0	100
	7.9	100
Right Oblique	2.0	95.1
	8.4	100
Left Oblique	5.0	99.4
	8.4	100

Table 6: Measurements depths and gamma index results from Patient QA done on Phantom

3.4 Spot Scanning Measurements

3.4.1 Point Dose Comparison

For the absolute dose comparison, the phantom TLD doses from each of the spot scanning irradiation trials were compared to the calculated doses from the Eclipse treatment planning system. The RBE weighted dose to the superior target TLD was calculated by the

treatment plan to be 646.2 cGy(RBE), and 648.6 cGy(RBE) for the inferior target TLD. The values for calculated and measured target doses (cGy(RBE)), as well as the ratio of the measured to calculated doses, are given in Table 7 for four different irradiation trials. Trial 1, and trials 4-6 were irradiated on two separate dates.

	TLD Location	TPS Dose Calculated	Dose Measured	Ratio [Meas./Calc.]
TRIAL 1	Target Superior	646.2	654.3	1.013
	Target Inferior	648.6	627.9	0.968
TRIAL 4	Target Superior	646.2	631.6	0.977
	Target Inferior	648.6	638.1	0.984
TRIAL 5	Target Superior	646.2	631.8	0.978
	Target Inferior	648.6	625.6	0.964
TRIAL 6	Target Superior	646.2	634.8	0.982
	Target Inferior	648.6	646.3	0.996

Table 7: Target point dose comparison between treatment planning system and TLDs for all irradiation trials

Trials 2 and 3 were not used in the final analysis. Trials 2 and 3 hade acceptable TLD readings for the target but vast OAR dose discrepancies when compared to the TPS, as shown in Table 8. The parotids received twice the dose predicted when compared to the TPS and the cord was given target dose. After investigating these inconsistencies, it was discovered that the IMPT plan had been delivered incorrectly for trials 2 and 3 and that was the reason why the results were poor and did not agree with the calculated dose distributions from the planning system. The couch had a 20 degree rotation on each oblique beam and that couch kick was not employed during the irradiations. Figure 3.7 shows a comparison of the axial trial's 1 and 3 films. The film clearly displays the issue where the dose on Trial 3 is significantly less conformal than on Trial 1, which would explain why the OARs around the target received

higher than predicted doses. The couch rotation was corrected for irradiations 4, 5 and 6 and the results were much more consistent and accurate for the doses delivered to the target and especially critical structures.

	TLD Location	Dose Calculated - Dose measured TPS	Ratio [Meas./Calc.]
TRIAL 2	**Target Superior**	646.2 656.0	1.015
	Target Inferior	648.6 637.0	0.982
	Parotid Left	250.2 453.6	1.813
	Parotid Right	206.4 459.0	2.224
	Cord	503.4 604.9	1.202
TRIAL 3	**Target Superior**	646.2 657.0	1.018
	Target Inferior	648.6 633.6	0.977
	Parotid Left	250.2 443.4	1.772
	Parotid Right	206.4 459.0	2.224
	Cord	503.4 604.5	1.201

Table 8: TLD readings for faulty trials 2 and 3.

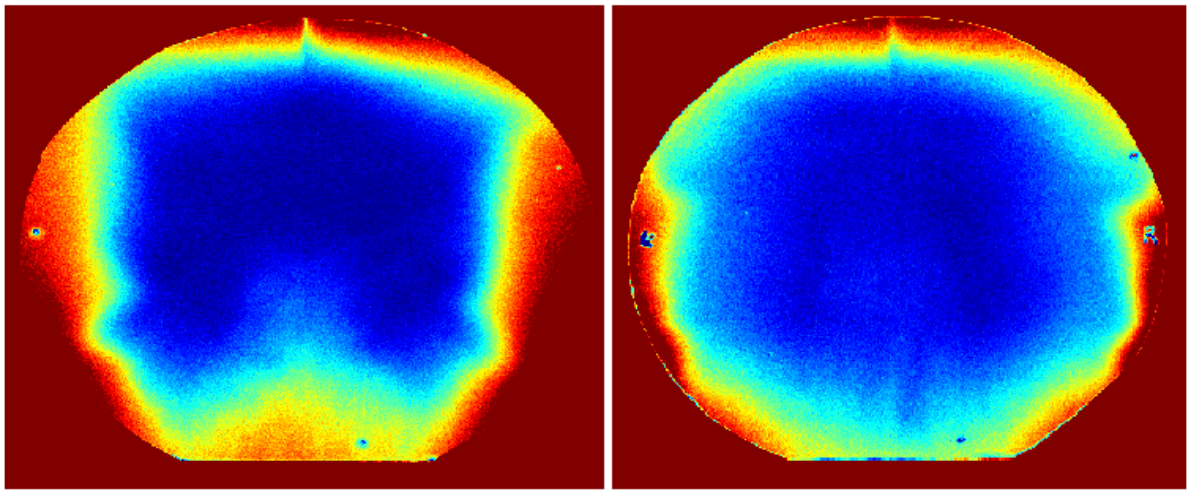

(a) Trial 1 Axial film **(b) Trial 3 Axial film**

Figure 3-9: Axial film scans showing the difference in dose distribution

The superior and inferior target TLD doses for the correctly delivered irradiation trials 1, 4, 5 and 6 were averaged and are shown in Table 9. The measured to calculated ratios showed good agreement between the treatment planning system and the average TLD measurements, 1.6% for the superior target and 1.4% for the inferior. Both target TLD ratios are well below IROCs acceptance criterion of ±5% dose agreement tolerance. The percent standard deviation for the TLD measurements combined (trials 1, 4, 5 and 6) was 1.52%, and therefore meet the 3% reproducibility criterion established in the hypothesis.

	TPS Dose [cGy]	Average Dose Values between Trials 1, 4, 5 and 6 [cGy]	Ratio [Meas./Calc.]
Target Superior	646.2	636.1	0.984
Target Inferior	648.6	639.6	0.986

Table 9: Average target TLD doses for the relevant trials 1, 4 and 5 and measured to calculated ratios

The target TLD doses were 1.6% and 1.4% low when compared to the TPS calculations. One possible explanation for this outcome could be that proton therapy treatment planning systems tend to overestimate target doses by as much as 3.5% for head and neck patients when compared to Monte Carlo simulations as described by Schuemann J. [52] Margins are used in order to account for the inaccurate predictions of the proton range and absolute dose but due to the high complexity of the head and neck geometries and inhomogeneities, these malignancies show the largest dose variations (3-4%) between TPS and Monte Carlo. [52] Our measurements support these findings and would agree with the Monte Carlo dose calculations.

The values for the calculated and measured doses for the critical structures in the phantom are shown in Table 10 along with the ratio of the measured to calculated doses. Table 11 shows the average OARs values for trials 1, 4, 5 and 6. A TLD was also inserted into the

oral cavity in order to ascertain that the dose delivered around the mandible and teeth were kept low, since that is a very sensitive region in patients. That TLD was not part of the treatment plan and therefore a measured to calculated ratio could not be established. Nevertheless, the average reading between all the trials for the mouth TLD was 1.4 cGy, well below clinical constraints.

	TLD Location	Dose Calculated - TPS	Dose measured	Ratio [Meas./Calc.]
TRIAL 1	**Parotid Left**	250.2	274.8	1.098
	Parotid Right	206.4	199.1	0.965
	Cord	503.4	493.2	0.980
TRIAL 4	**Parotid Left**	250.2	273.5	1.093
	Parotid Right	206.4	209.3	1.014
	Cord	503.4	498.5	0.990
TRIAL 5	**Parotid Left**	250.2	285.3	1.140
	Parotid Right	206.4	209.6	1.015
	Cord	503.4	486.5	0.966
TRIAL 6	**Parotid Left**	250.2	311.1	1.243
	Parotid Right	206.4	209.8	1.016
	Cord	503.4	492.7	0.979

Table 10: Critical Structure point dose comparison between treatment planning system and TLDs

	TPS Dose [cGy]	Average Dose Values between Trials 1,4, 5 and 6 [cGy]	Ratio [Meas./Calc.]
Parotid Left	250.2	286.1	1.143
Parotid Right	206.4	206.9	1.002
Cord	503.4	492.7	0.978

Table 11: Average OARs TLD doses for the relevant trials 1, 4 and 5 and measured to calculated ratios

It is also possible to notice that the OAR ratios showed good agreement. The ratios for the parotid doses were 14.3% and 0.2% high for the left and right parotids respectively, while the cord had a dose agreement of 2.2%. It is noticeable that the left parotid has the poorest agreement with the TPS predicted doses. One possible explanation for that is that the left parotid was located in a higher dose gradient region than the right parotid, seen on the axial

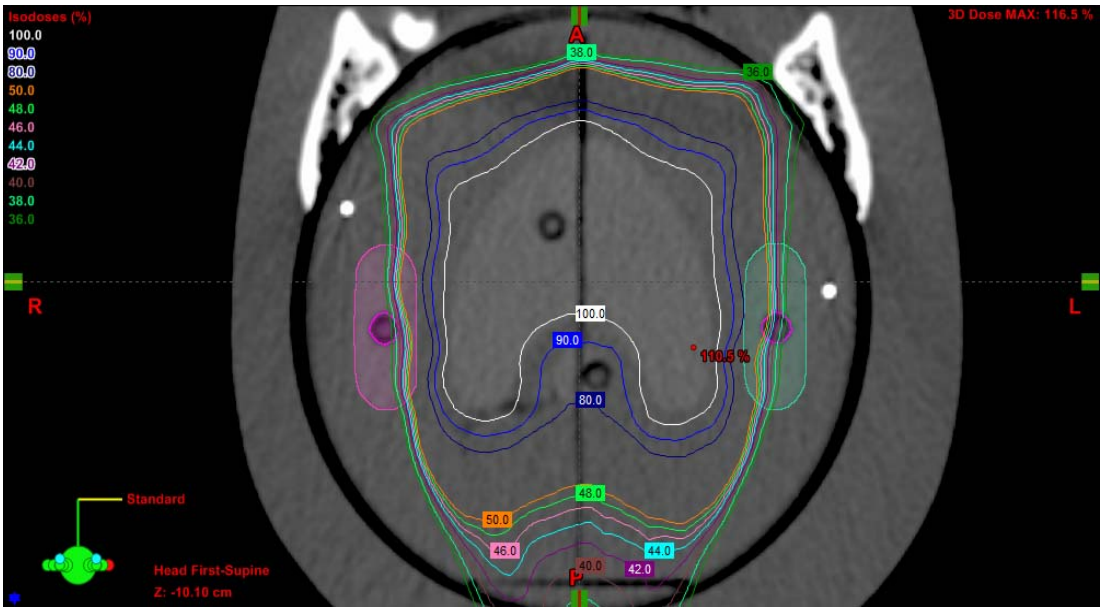

Figure 3-10: Axial screenshot of treatment plan with isodose lines shown to be on top of the left parotid TLD.

screenshot of the treatment plan in Figure 3.10. That means that very small shifts in the setup could represent large dose difference in the TLD results between the several trials.

3.4.2 Relative Dose Comparison

The 2D dose distributions were analyzed by comparing the dose distribution calculated by the treatment planning system and the one measured by the phantom films in the axial and sagittal planes. The film dose distributions were normalized to the TLD doses at the locations of the TLD capsules in the target. The film and CT registration using the pin pricks on the

films was achieved with an RMS < 1mm for all irradiation trials. The RMS error ranged from 0.24 mm to 0.98 mm for the film registration and the 3D RMS used in analysis was 0.54 mm for the CT images. The gamma index acceptance criteria hypothesized in this project is ±7%/4mm, nevertheless tighter criteria of ±5%/3mm, ±5%/4mm were also evaluated. The 2D gamma analysis results showing the percent of pixels meeting the various acceptance criteria for irradiation trials 1, 4, 5 and 6 are listed in Table 12. All trials pass the 85% criteria used at IROC for the gamma index proposed in the hypothesis (±7%/4 mm). As expected, tighter criteria show lower passing rates, but still perform well. The sagittal film in trial 5 is the only one that does not pass the ±5%/4mm criterion, with only 81.8% of pixels passing. The percent standard deviation for the gamma passing rates combined (trials 1, 4, 5 and 6) was 2.43%, and therefore also meet the 3% reproducibility criterion established in the hypothesis.

		2D Gamma Percentage of Pixels Passing		
		5%, 3mm	5%, 4 mm	7%, 4mm
TRIAL 1	**Axial**	86.3%	91.0%	95.5%
	Sagittal	82.6%	87.6%	94.2%
TRIAL 4	**Axial**	91.0%	94.0%	97.3%
	Sagittal	80.2%	87.0%	93.2%
TRIAL 5	**Axial**	82.1%	88.6%	93.4%
	Sagittal	76.0%	81.8%	90.0%
TRIAL 6	**Axial**	91.0%	93.4%	96.2%
	Sagittal	80.6%	86.4%	92.7%

Table 12: 2D gamma analysis pass rates for the spot scanning irradiations

The dose map obtained in the gamma analysis shows the same general distribution of passing and failing pixels through the four trials. Pixels that have a calculated gamma of less than 1 are considered to pass and are assigned the color light blue/blue. As it can be seen in

Figure 3.11, the largest amount of pixels failing fall within the target and in the posterior portion of the film plane. The pixels at the bottom could be falling because of uncertainty present in the calculation of the end of the proton beam range. Both oblique beams conform to the isodose lines creating a bump in the posterior part of the axial film, as seen in Figure 3.12. That area coincides with the failing area in the gamma dose map. Similarly to the axial films, on Figure 3.13, the sagittal films show the majority of the failing pixels to be located inside the target and in the posterior region on the film. The complete set of gamma indexes for all trials and criteria can be found in the Appendix.

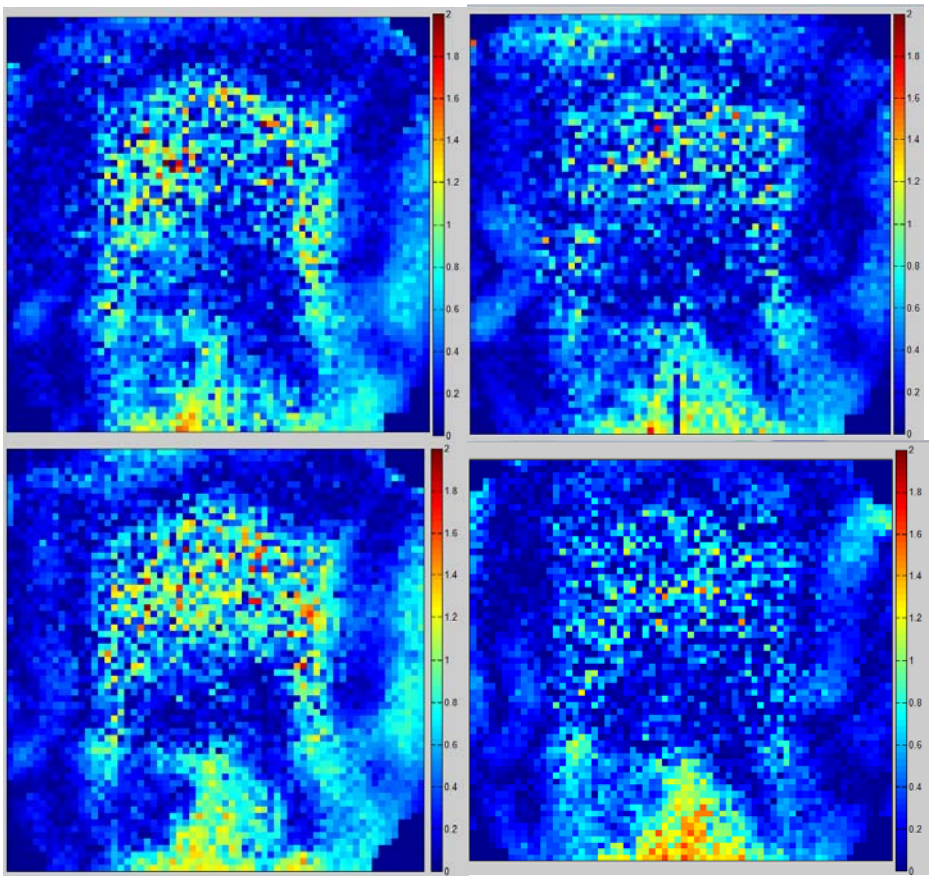

(b) Trial 1 Axial 95.5% **(b) Trial 4 Axial 97.3%**

(c) Trial 5 Axial 93.4% **(d) Trial 6 Axial 96.2%**

Figure 3-11: Axial views for Trials 1, 4, 5 and 6 for 7%,4mm.

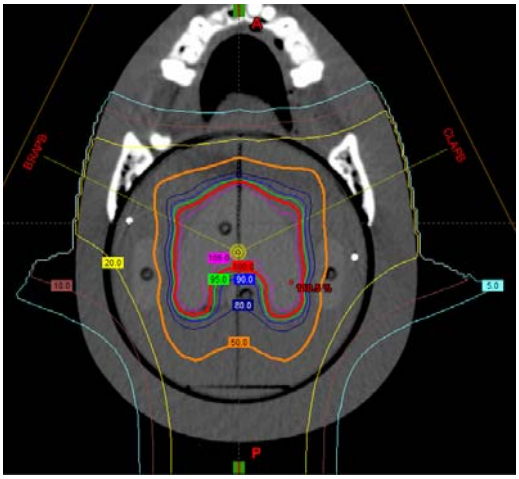

Figure 3-12: Slice of treatment plan showing isodose lines.

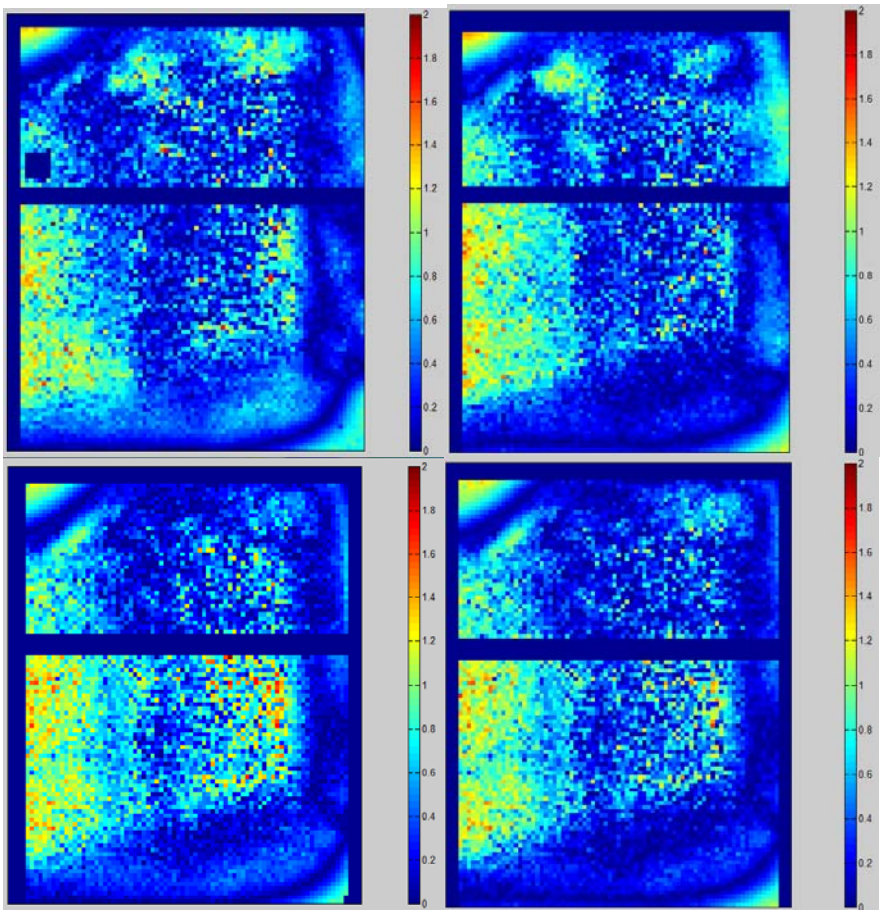

(a) Trial 1 Sagittal 94.2% **(b)Trial 4 Sagittal 93.2%**

(b) Trial 5 Sagittal 90.0% **(d) Trial 6 Sagittal 92.7%**

Figure 3-13: Sagittal views for Trials 1, 4, 5 and 6 for 7%,4mm.

The gamma analysis results for the faulty trials 2 and 3 were also performed for the criteria (7%/4mm) used in this project and the pixel passing percentages are shown in Table 13. It is noticeable that neither trials passed IROC's standard passing rate of 85% of pixels. Both results were similar to each other and well below trials 1, 4, 5 and 6. Figure 3.14 shows the large areas in the axial and sagittal dose maps failing the gamma criteria. This result can demonstrate part of the consequences of how the wrongful application of couch angles can affect the treatment delivery. The harm of misplacing the couch during treatment was also demonstrated in the point dosimetry in the previous section. The target TLDs, placed in the center, showed good conformance with the treatment plan, with ratios within IROCs acceptance standards. However, the OARs, situated more superficial to the target, had large discrepancies in their TLD readings. This could be extrapolated to a real life scenario where, if couch angles were overlooked tumor control would be achieved but along with very high healthy tissue toxicity to the patient.

		2D Gamma Percentage of Pixels Passing
		7%, 4mm
TRIAL 2	**Axial**	74.4%
	Sagittal	78.2%
TRIAL 3	**Axial**	79.5%
	Sagittal	79.5%

Table 13: 2D gamma analysis pass rates for trials 2 and 3 along with their averages

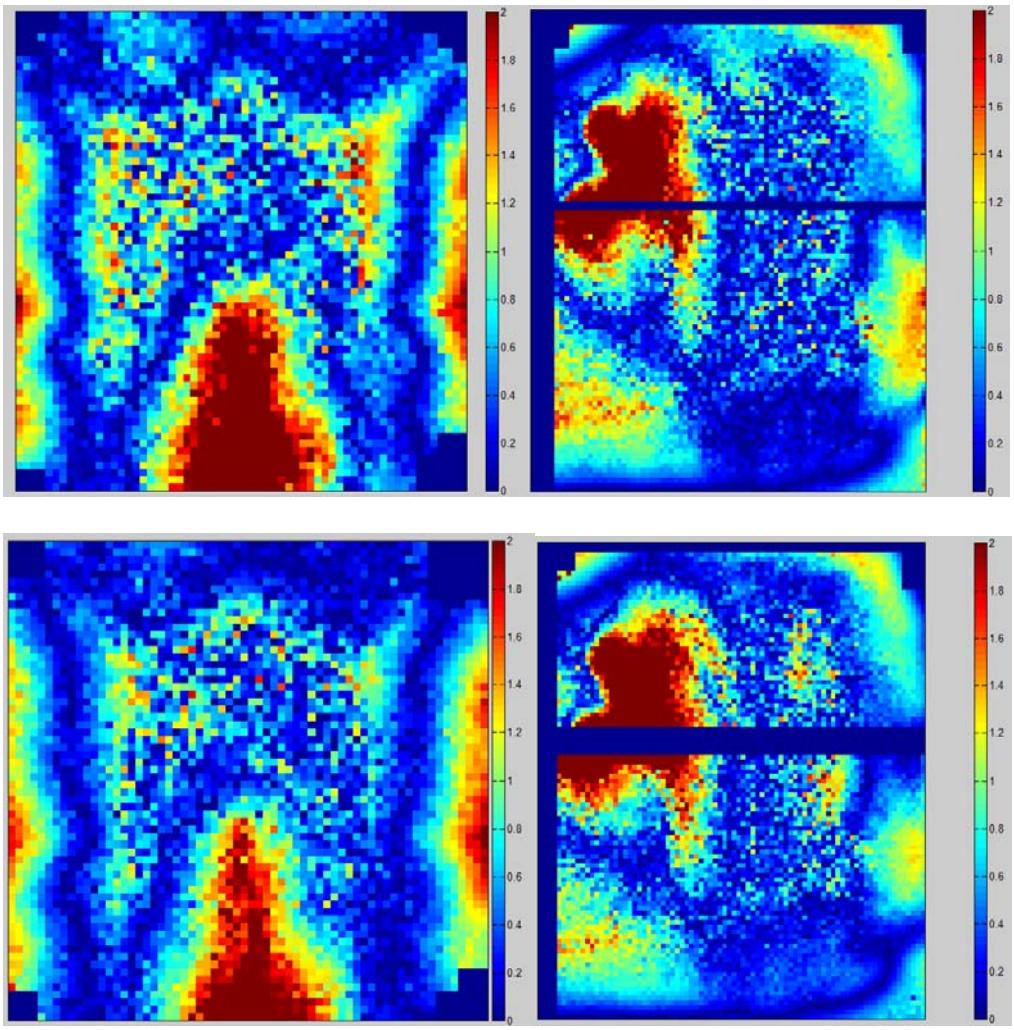

(a) Trial 2 Axial 74.5% **(b)Trial 2 Sagittal 78.2%**

(b) Trial 3 Axial 79.5% **(d) Trial 3 Sagittal 79.5%**

Figure 3-14: Axial and Sagittal dose maps for the faulty trials 2 and 3.

3.4.3 Profile Analysis

Dose profiles comparing the TPS dose with the measured film dose for the trials were also analyzed. The film profile was obtained from the same IROC in-house software used for the film analysis. The film dose curve was smoothed by averaging each data point with 10 values above and below the particular point. Figure 3.16 through Figure 3.19 show the dose

profiles for Trial 1. The left to right profiles cross the target and parotids but not the spinal cord, while the anterior posterior profiles miss the parotids and cross the cord structure. The inferior superior profiles pass through the target inside the TLD slots. These profile references can be seen in Figure 3.15 where the representation of the path of the profiles is shown. The additional profiles can be seen in the Appedix seccion. All profiles analyzed showed the general shape predicted in the TPS, presenting no setup shifts or clear proton beam range issues.

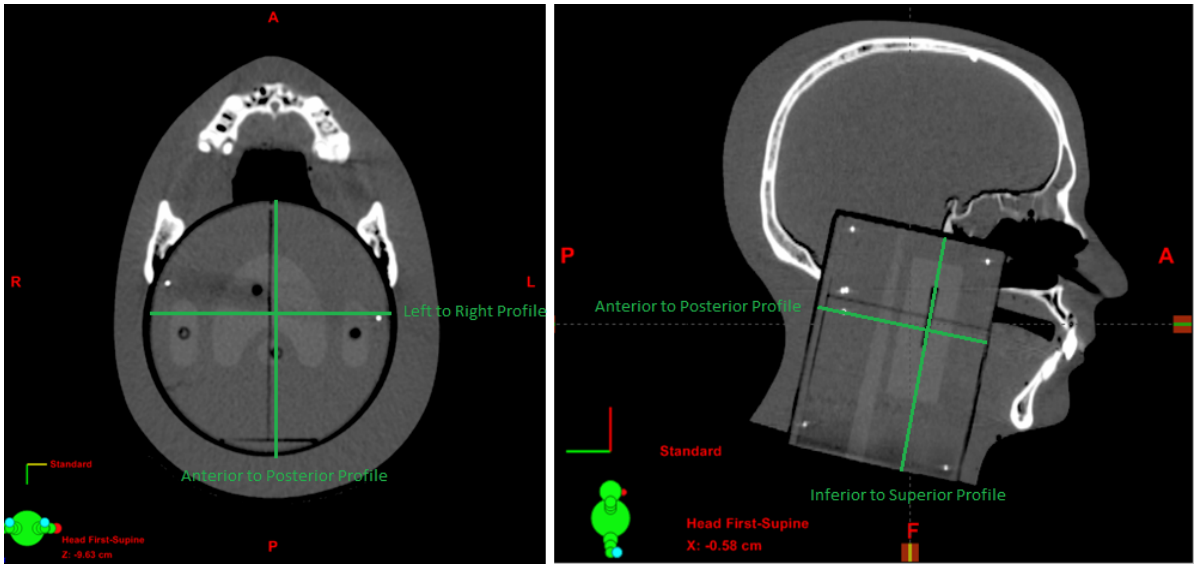

Figure 3-15: Profile Labeling of the orientation of the 4 different profiles.

These profiles also show the areas that failed the gamma analysis. The previous section showed that most pixels failed the axial films inside the target and towards the posterior section on the phantom. Both AP profiles show the largest discrepancy between the TPS and film dose curves to be within the plateau of the target and behind the cord.

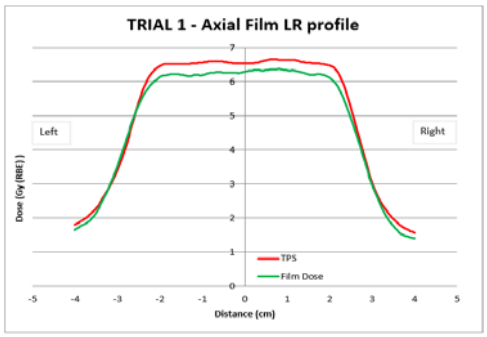

Figure 3-16: Axial (left to right) dose profile comparing the TPS dose with the measured film dose for Trial 1

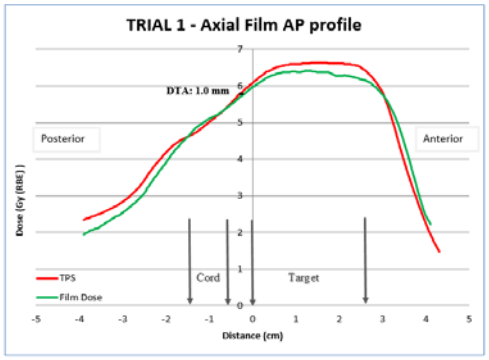

Figure 3-17: Axial (anterior to posterior) dose profile comparing the TPS dose with the measured film dose for Trial 1

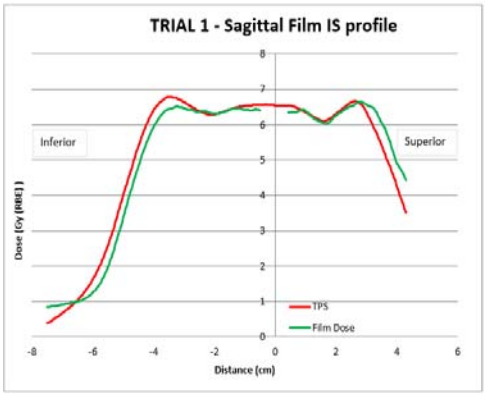

Figure 3-18: Sagittal (inferior to superior) dose profile comparing the TPS dose with the measured film dose for Trial 1

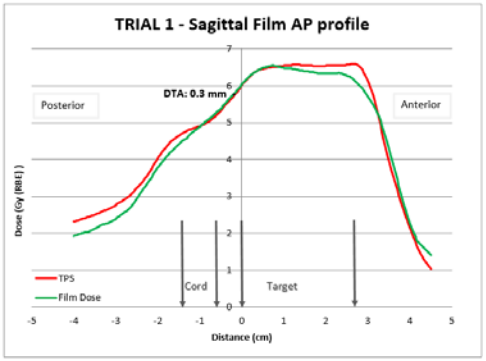

Figure 3-19: Sagittal (anterior to posterior) dose profile comparing the TPS dose with the measured film dose for Trial 1

Distance to agreement (DTA) for all the AP dose profiles were also measured and are shown below in Table 14. They were taken comparing the film dose curve to the TPS dose curve at the midpoint between the spinal cord and target. That was done in order to check the conformality of the dose distribution in that high dose gradient region. The film registration procedure has an uncertainty of 1 mm, but the all fall within IROC's acceptance criteria of 4 mm.

	Profile Orientation	DTA (mm)
TRIAL 1	Axial AP	1.0
	Sagittal AP	0.3
TRIAL 4	Axial AP	0.6
	Sagittal AP	1.9
TRIAL 5	Axial AP	1.6
	Sagittal AP	3.3
TRIAL 6	Axial AP	0.6
	Sagittal AP	2.3

Table 14: Distance to agreement for all AP dose profiles

3.4.4 TLD Verification

A TLD verification procedure was performed in order to check the proton beam output at the same gantry the irradiations were performed. A TLD block, used at IROC for the same purpose, was loaded with 5 TLDs and placed in the center of the SOBP. In order to achieve the correct depth, blocks of acrylic were added in front on the block. The block identification number was E316 and the total dose delivered was 220.3 cGy(RBE). The TLD doses obtained are shown in Table 15 along with the measured to calculated ratios.

	Dose measured	Dose Calculated TPS	Ratio [Meas./Calc.]
TLD 1	216.78	220.30	0.984
TLD 2	213.10	220.30	0.967
TLD 3	215.56	220.30	0.979
TLD 4	217.24	220.30	0.986
TLD 5	217.75	220.30	0.988
Average			0.980

Table 15: Measured TLD doses for the beam output check and the measured to calculated ratios.

The output verification was completed with TLDs from the same batch used in the irradiations. Similarly to the pattern observed in the irradiations, the dose delivered is lower than what predicted. This could represent one potential reason for why the TLD values obtained in the irradiation trials were slightly lower than the TPS or, for the same reason as for the trials, the TPS could be overestimating the planned doses.

4 Conclusions

The hypothesis that an anthropomorphic head and neck phantom can be designed and built to evaluate proton therapy treatment procedures for oropharyngeal cancer with an agreement between measured and calculated doses of ±7%/4mm with a reproducibility of 3% was met for the pencil beam treatment plan. The phantom was used in four end to end scanning treatments and they all passed the 85% pixel passing gamma and IROC's TLD acceptance criteria of ±5% dose agreement tolerance. The scattering plan was not able to be delivered due its lack of clinical relevance and therefore did not have an analysis performed.

The phantom was successfully used as a QA tool with the purpose of simulating a head and neck disease. The horse shoe shaped insert and structures inside were made of solid water and blue water respectively. The design included the oropharyngeal target to be treated and three OARs to be protected, two parotids and a spinal cord. Spot scanning and passive scattering treatment plans were created but due to the lack of clinical relevance of the passive plan, it was determined that it ought not to be delivered. The pencil beam plan achieved adequate target coverage and acceptable parotid doses. The maximum cord dose exceeded the dose restriction because of the tight fit of the insert.

For the point dosimetry, the average dose values between trials 1, 4, 5 and 6 were 636.1 cGy and 639.6 cGy for the superior and inferior target TLDs, respectively. The measured to calculated ratios were 0.984 for the superior target TLD and 0.986 for the inferior target TLD. Being only 1.6% and 1.4% lower than expected, both TLD results fall within IROC's acceptance criteria. The relative dose comparison was performed using a gamma index of ±7%/4 mm, and all trials passed the 85% pixel passing criteria established at IROC. Trial 1 axial being 95.5%, sagittal 94.2%, trial 4 axial being 97.3%, sagittal 93.2%, trial 5

axial 93.4%, sagittal 90.0%, and finally trial 6 axial being 96.2 and sagittal 92.7%. As expected, the tighter criteria (±5%,4mm and ±5%,3mm) had poorer passing rates. The tighter criteria are not suitable for this particular project due to the inherent uncertainty in the detectors used and the nature of the phantom design. The ICRU recommends a radiation dose agreement of ±5% compared to patient treatment plans. However, the TLDs used in the project have 1.5% uncertainty in their dose measurements. That means that institutions that deliver doses close to the ±5% ICRU expectations need extra room to be considered acceptable due to the TLD uncertainty. In addition, the phantom itself contains large heterogeneities, such as bony structures and air cavities that make it harder to obtain perfect measurements or pass tighter criteria. Like the dose criteria, there is uncertainty in the distance to agreement portion of the film measurements. The film registration process is allowed a 1 mm uncertainty while registering the film pin pricks and TLD's positions. Also, similar to the photon H&N phantom, there are very high dose gradients in these treatment plans, demanding a 4mm criteria to more complex of the phantom designs.

Moving forward, a new insert should be designed where the target and organs at risk are placed slightly farther from each other. The cord could be moved down a centimeter and the target could be shrunken down slightly. That would aim to allow for a passive scattering plan to be successfully created and delivered to the phantom. Another possible advantage of constructing an alternative insert would be to more easily achieve clinical constraints for the OARs. The current design did not allow for the pencil beam plan to effectively protect the spinal cord maximum dose, thus a new design could be created to addressed that issue as well.

5 Appendix

5.1 Gamma Analysis

5.1.1 7% 4 mm Criteria

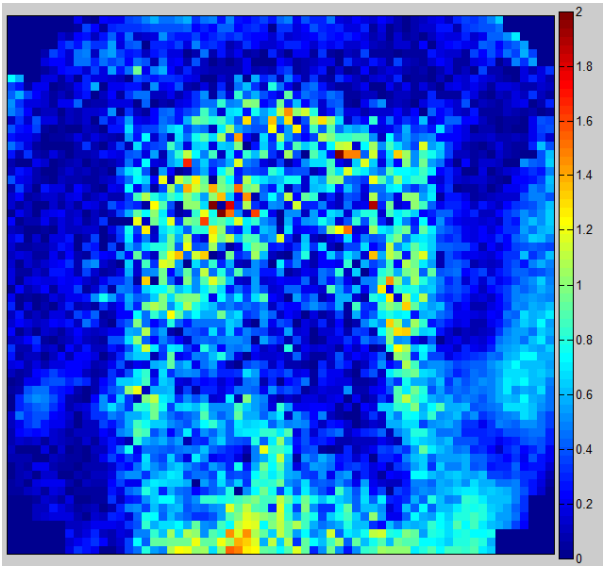

Figure 5-1: TRIAL 1 - Axial 95.5% (7%, 4mm)

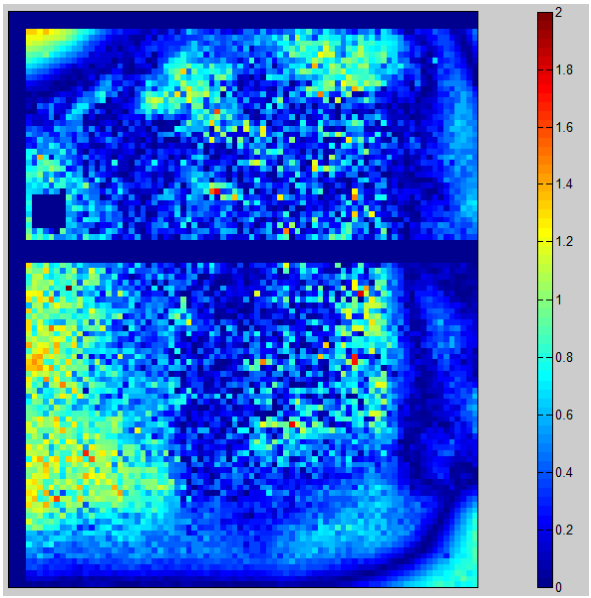

Figure 5-2: TRIAL 1 - Sagittal 94.2% (7%, 4mm)

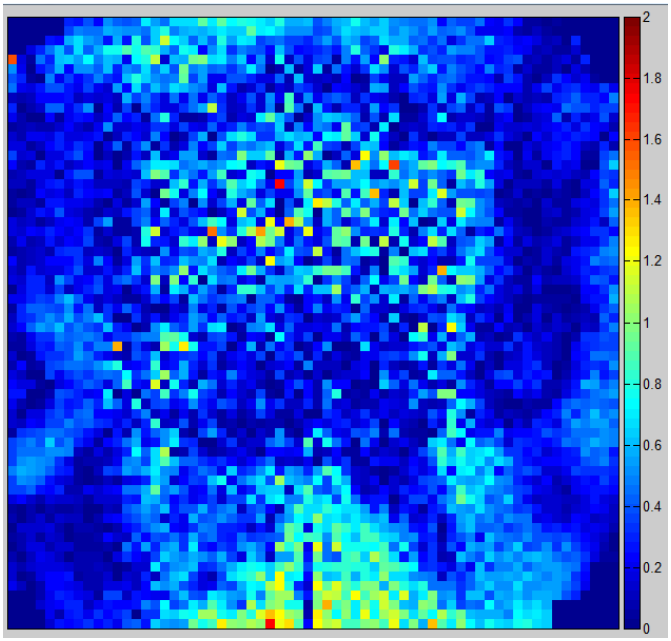

Figure 5-3: TRIAL 4 – Axial 97.3% (7%, 4mm)

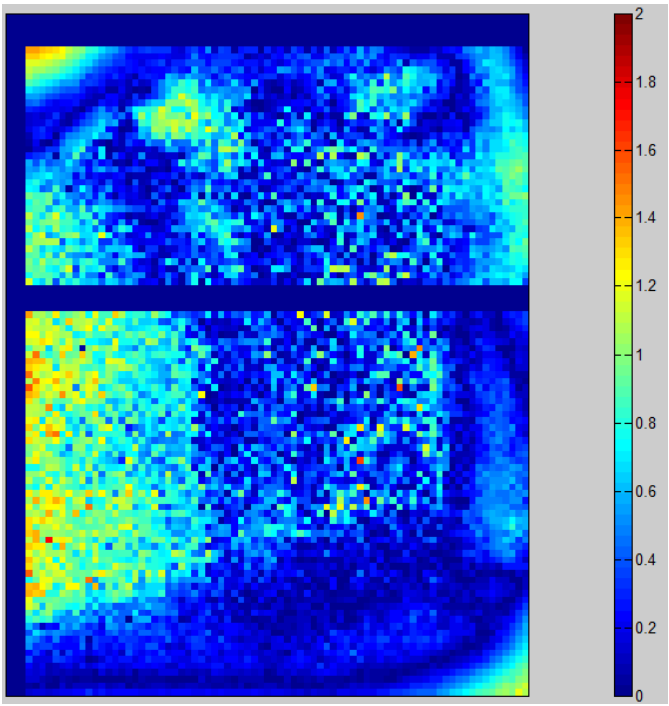

Figure 5-4: TRIAL 4 – Sagittal 93.9% (7%, 4mm)

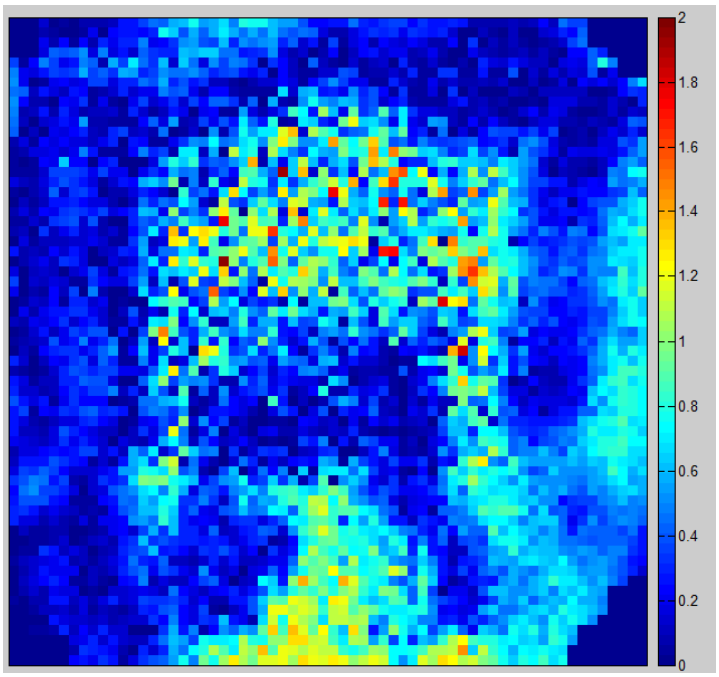

Figure 5-5: TRIAL 5 – Axial 93.4% (7%, 4mm)

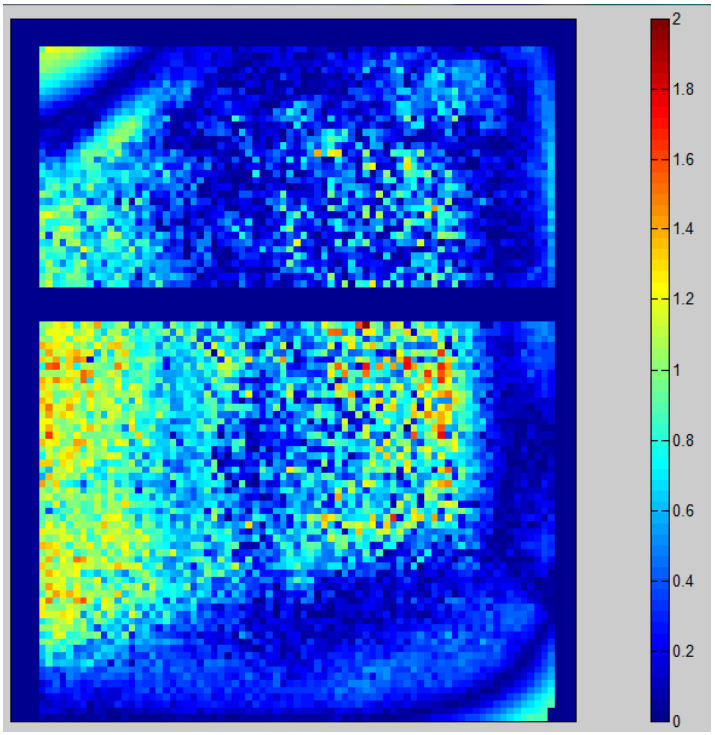

Figure 5-6: TRIAL 5 – Sagittal 90.0% (7%, 4mm)

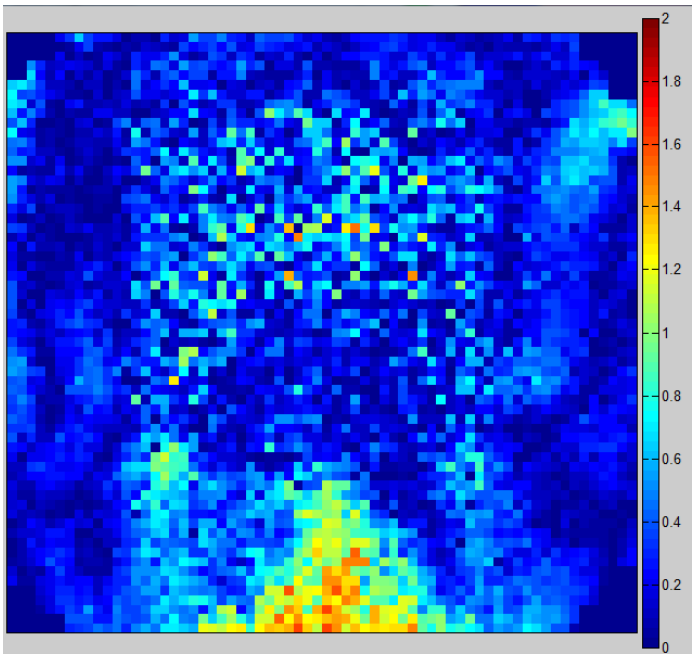

Figure 5-7: TRIAL 6 – Axial 96.2% (7%, 4mm)

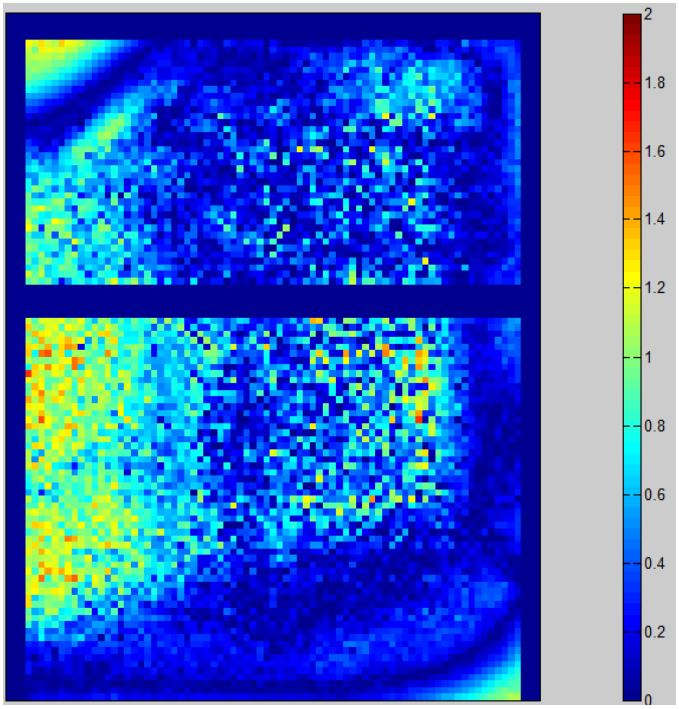

Figure 5-8: TRIAL 6 – Sagittal 92.7% (7%, 4mm)

5.1.2 5% 4 mm Criteria

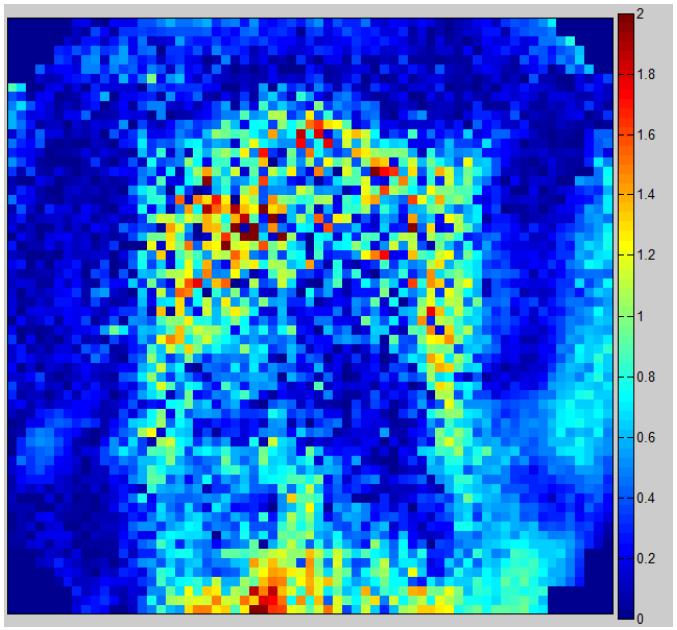

Figure 5-9: TRIAL 1 - Axial 91.0% (5%, 4mm)

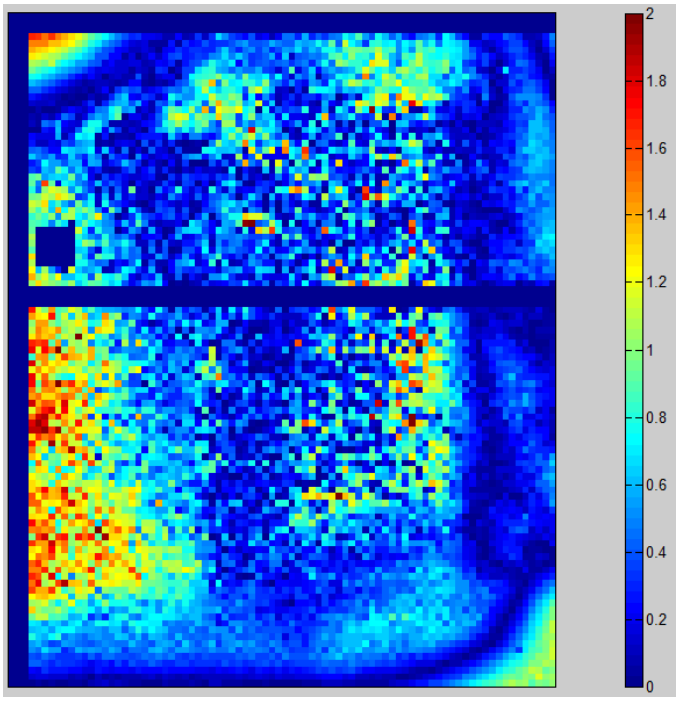

Figure 5-10: TRIAL 1 - Sagittal 87.62% (5%, 4mm)

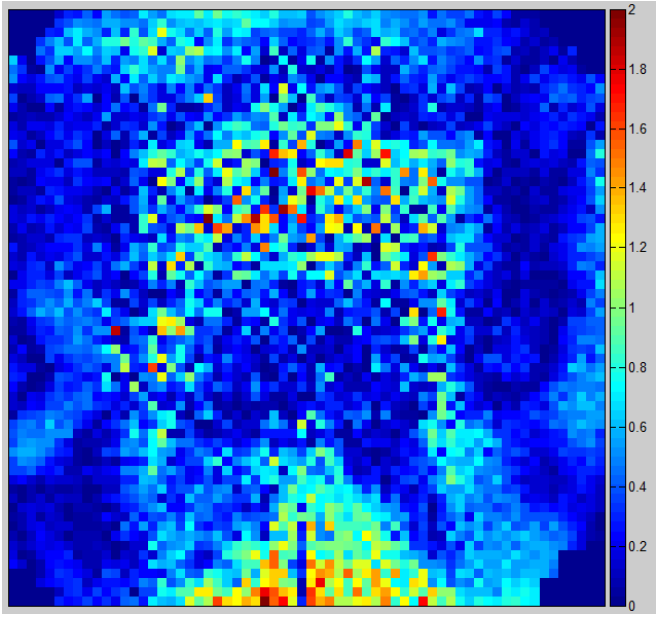

Figure 5-11: TRIAL 4 - Axial 94.0 % (5%, 4mm)

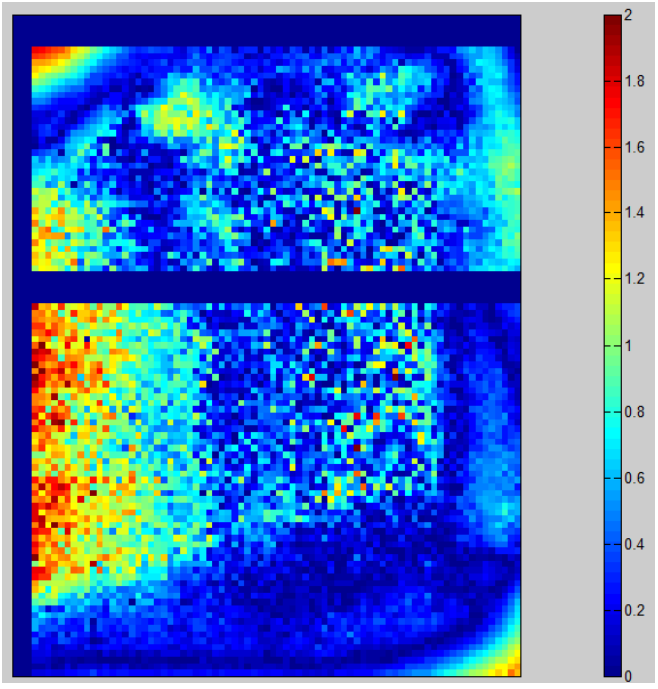

Figure 5-12: TRIAL 4 - Sagittal 87.0% (5%, 4mm)

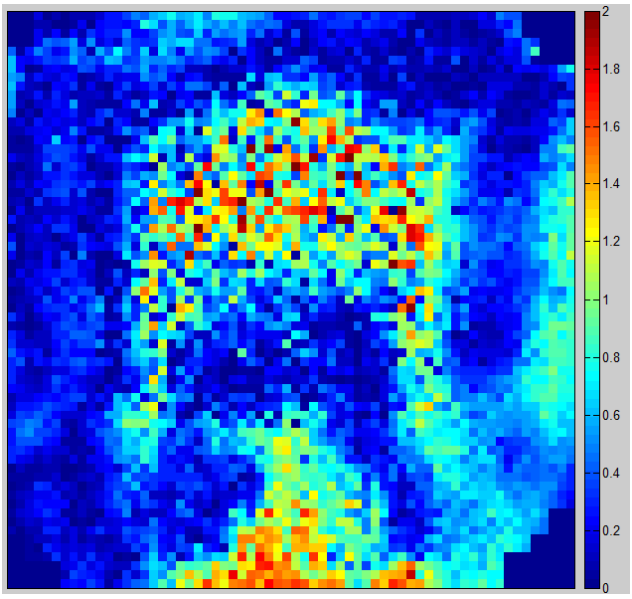

Figure 5-13: TRIAL 5 - Axial 88.5% (5%, 4mm)

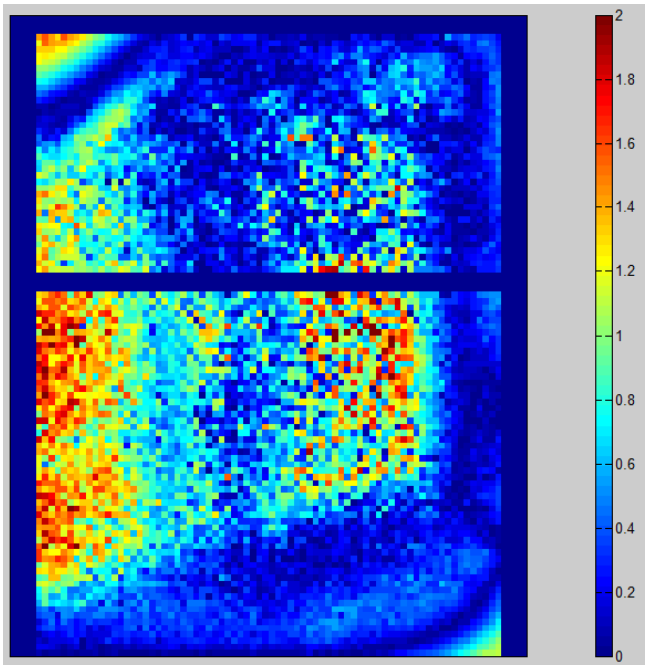

Figure 5-14: TRIAL 5 - Sagittal 81.8% (5%, 4mm)

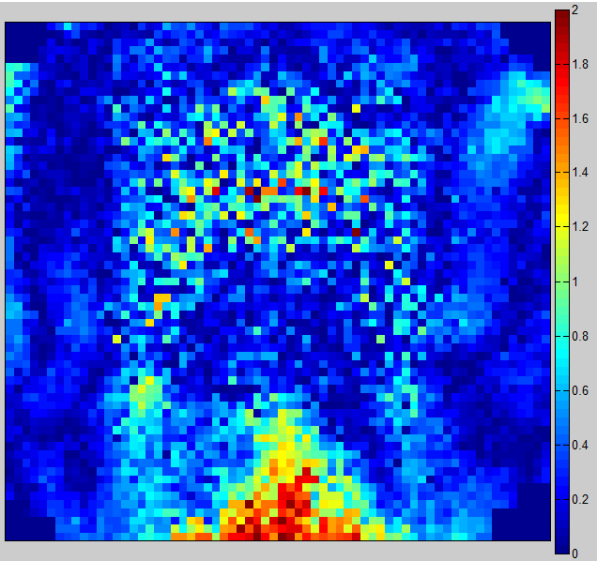

Figure 5-15: TRIAL 6 - Axial 93.4% (5%, 4mm)

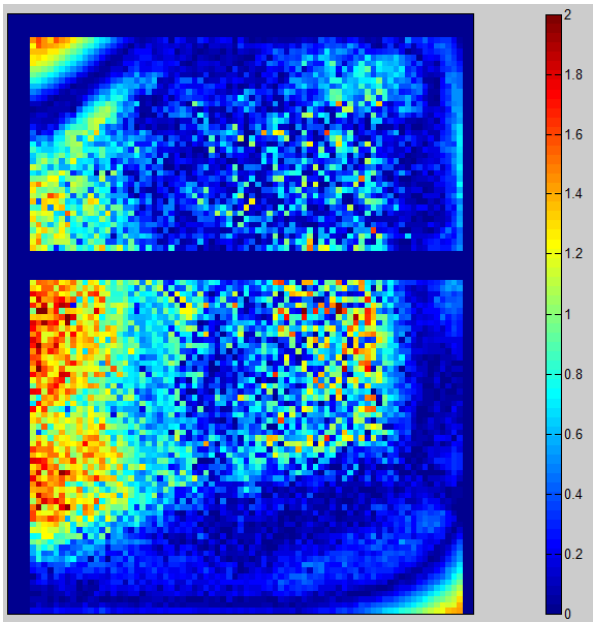

Figure 5-16: TRIAL 6 – Sagittal 86.4% (5%, 4mm)

5.1.3 5% 3 mm Criteria

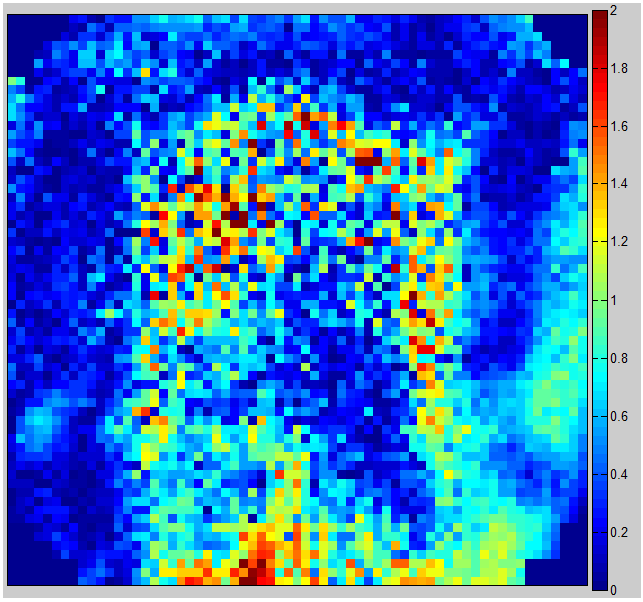

Figure 5-17: TRIAL 1 - Axial 86.27% (5%, 3mm)

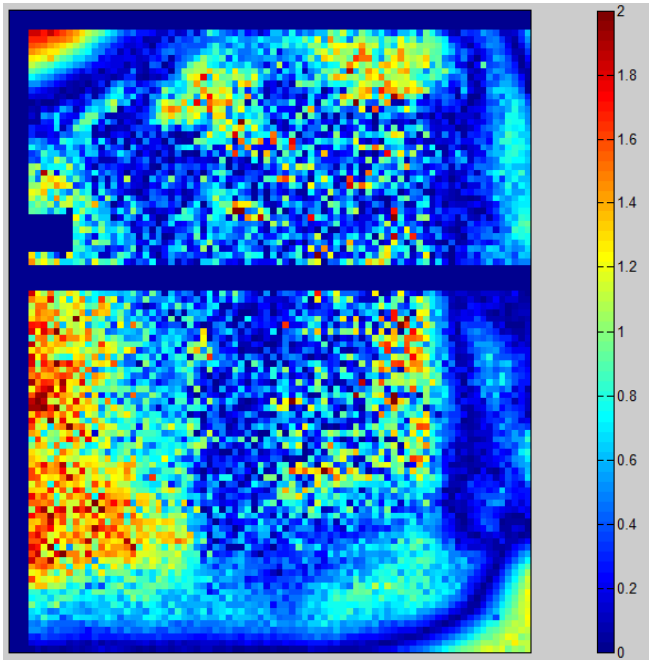

Figure 5-18: TRIAL 1 – Sagittal 82.61% (5%, 3mm)

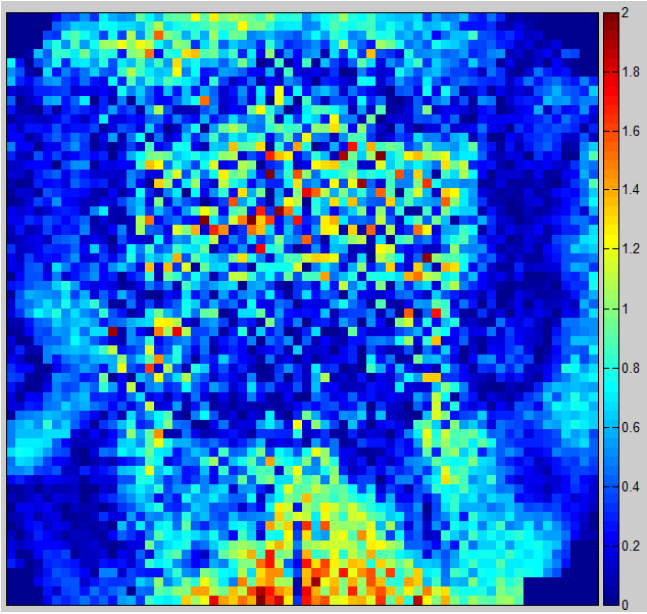

Figure 5-19: TRIAL 4 - Axial 90.69% (5%, 3mm)

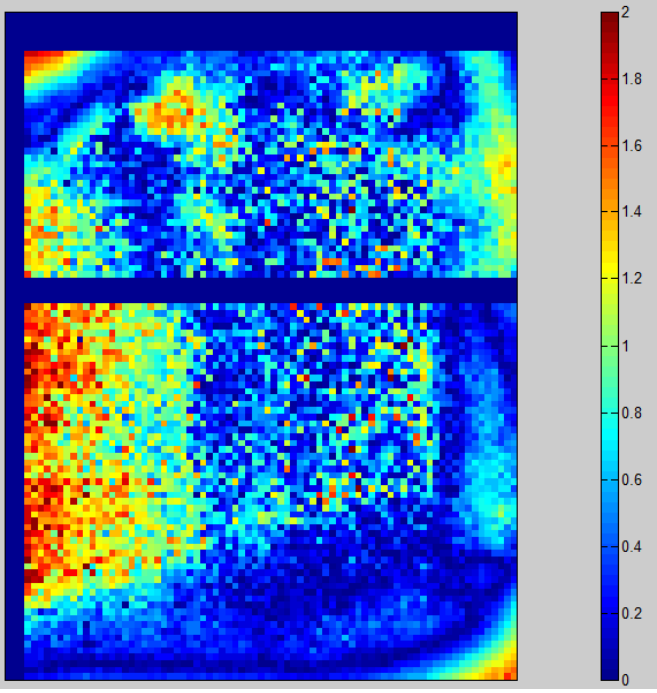

Figure 5-20: TRIAL 4 – Sagittal 80.2% (5%, 3mm)

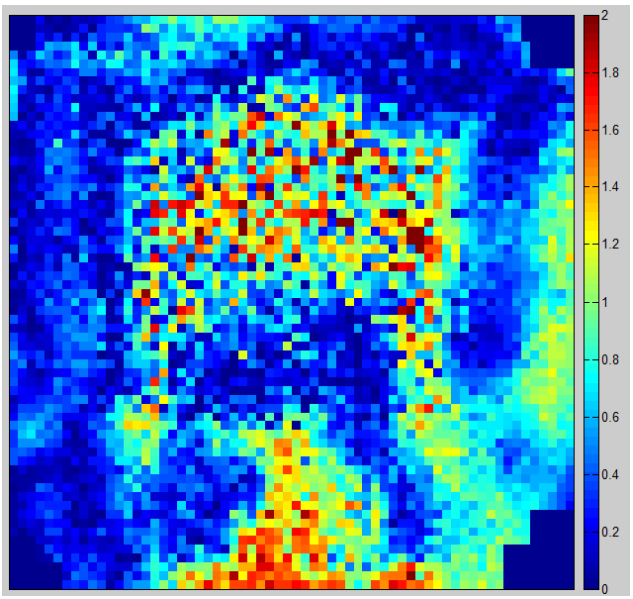

Figure 5-21: TRIAL 5 - Axial 82.1% (5%, 3mm)

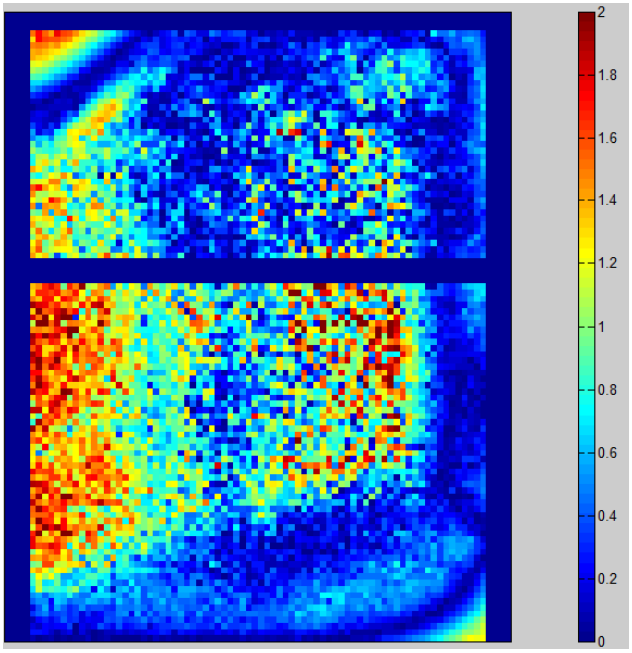

Figure 5-22: TRIAL 5 – Sagittal 76.0% (5%, 3mm)

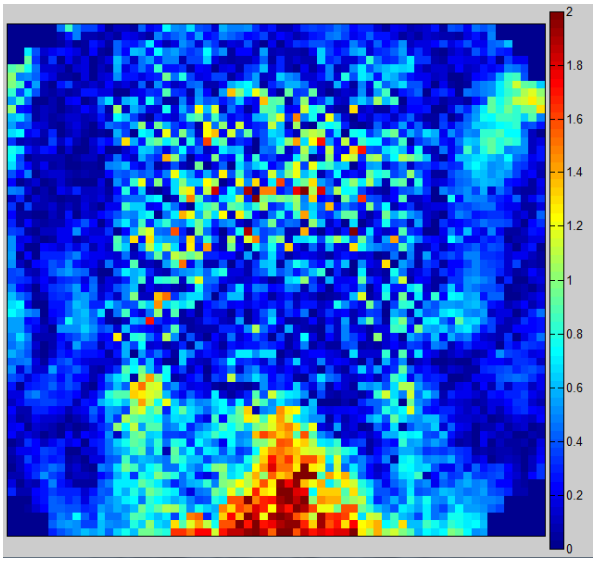

Figure 5-23: TRIAL 6 - Axial 91.0% (5%, 3mm)

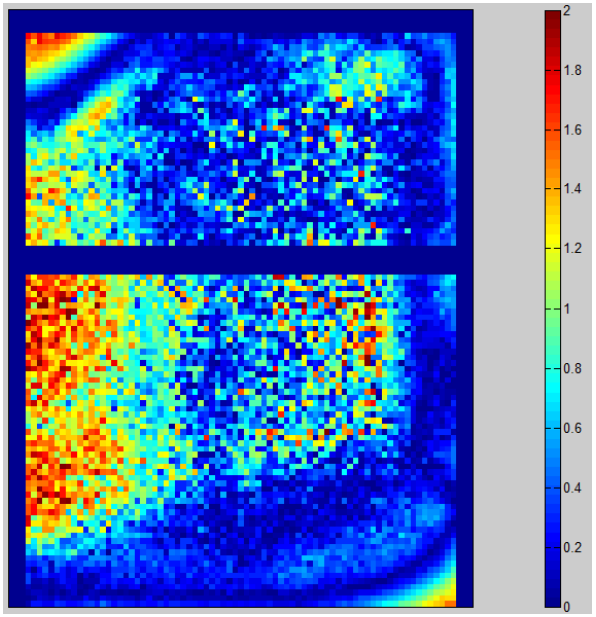

Figure 5-24: TRIAL 6 – Sagittal 80.6% (5%, 3mm)

5.1.4 7% 4 mm Criteria for the Faulty Trials

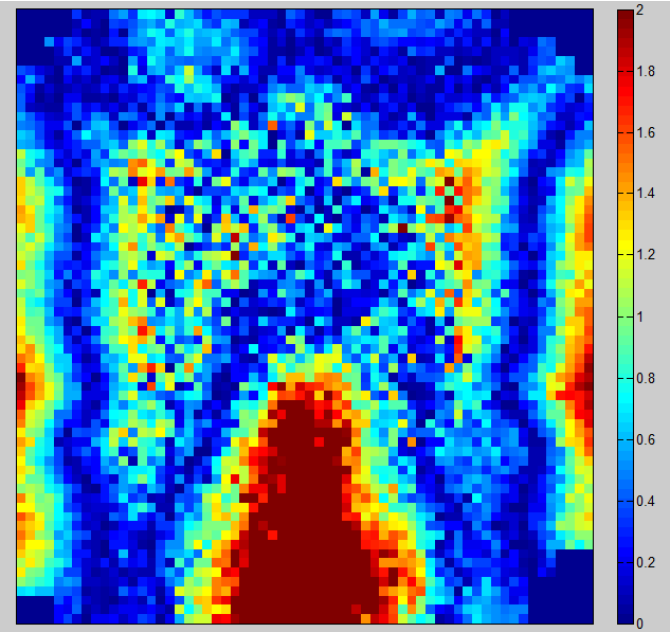

Figure 5-25: TRIAL 2 – Axial 74.5% (7%, 4mm)

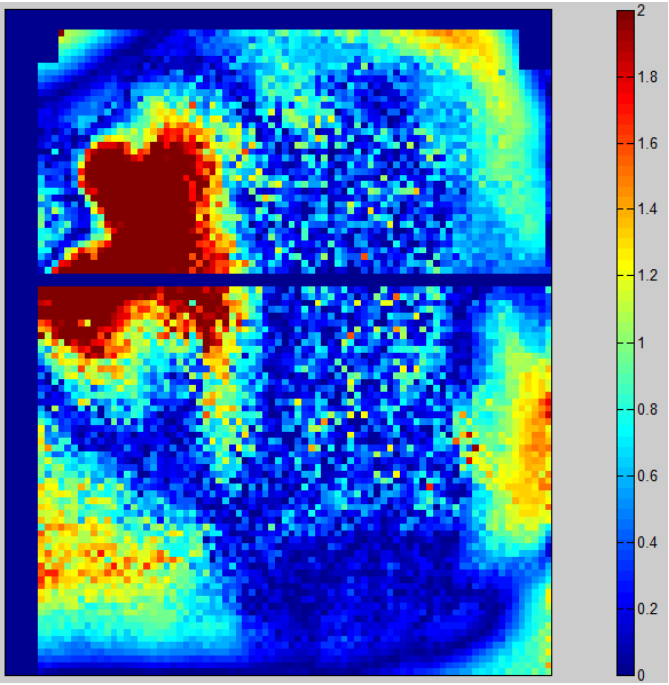

Figure 5-26: TRIAL 2 – Sagittal 78.2% (7%, 4mm)

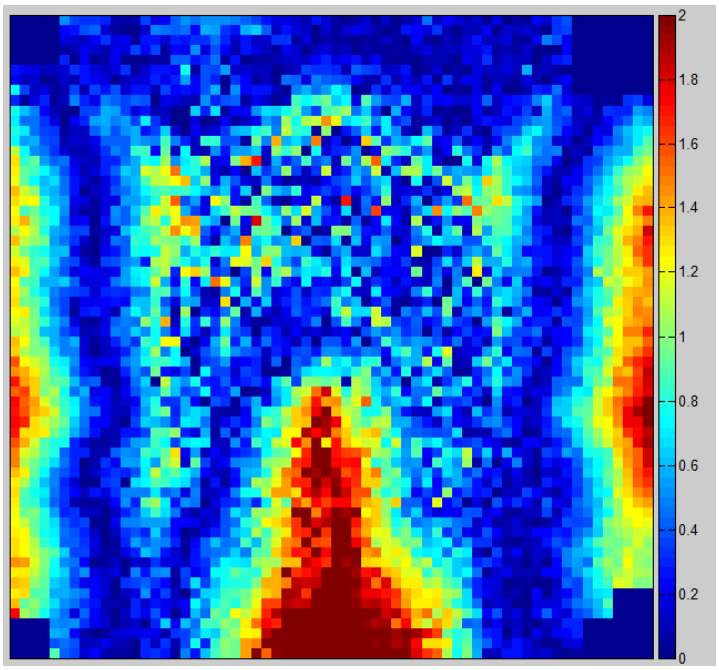

Figure 5-27: TRIAL 3 – Axial 79.5% (7%, 4mm)

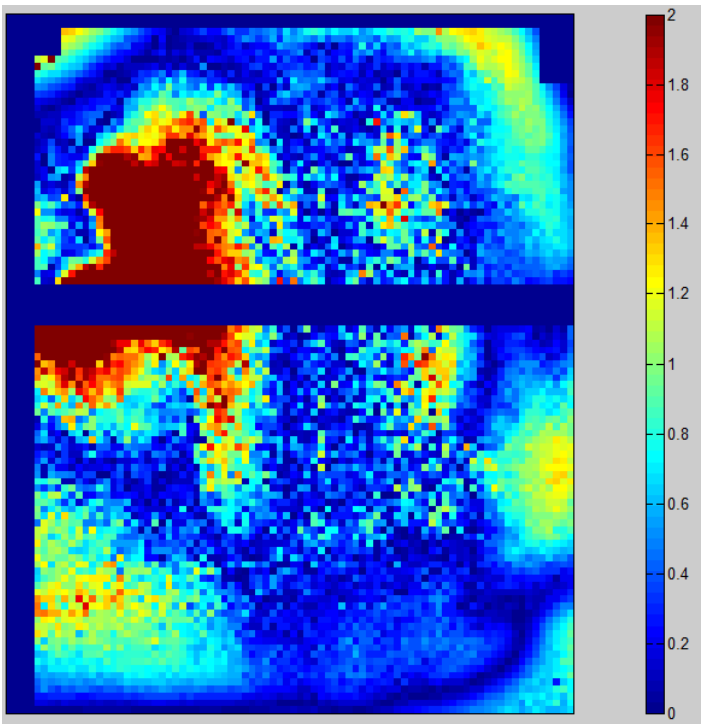

Figure 5-28: TRIAL3 – Sagittal 79.5% (7%, 4mm)

5.2 Film Profiles

5.2.1 Trial 1 Profiles

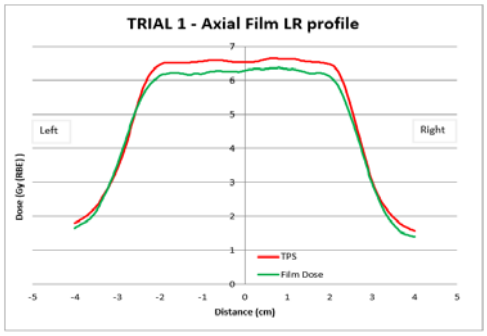

Figure 5-29: Axial (left to right) dose profile comparing the TPS dose with the measured film dose for Trial 1

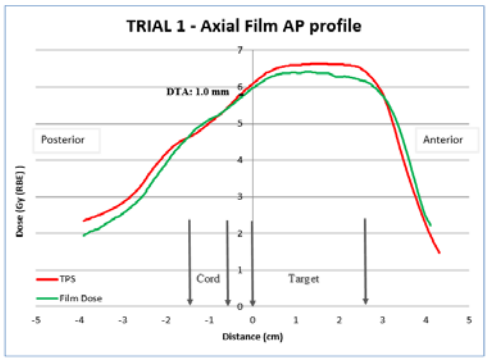

Figure 5-30: Axial (anterior to posterior) dose profile comparing the TPS dose with the measured film dose for Trial 1

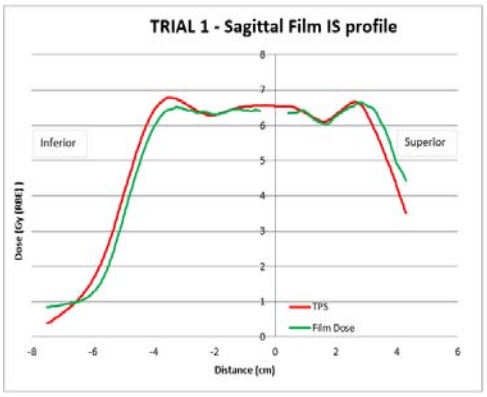

Figure 5-31: Sagittal (inferior to superior) dose profile comparing the TPS dose with the measured film dose for Trial 1

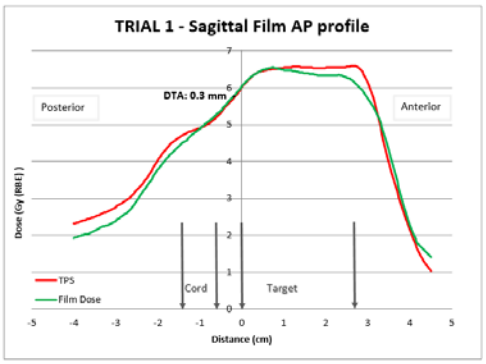

Figure 5-32: Sagittal (anterior to posterior) dose profile comparing the TPS dose with the measured film dose for Trial 1

5.2.2 Trial 4 Profiles

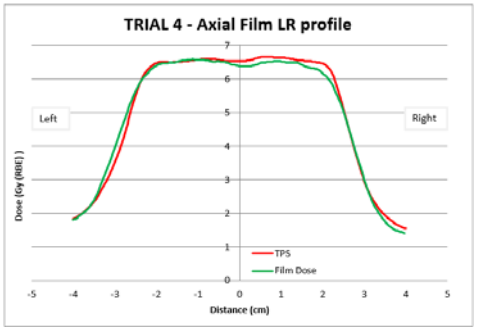

Figure 5-33: Axial (left to right) dose profile comparing the TPS dose with the measured film dose for Trial 4

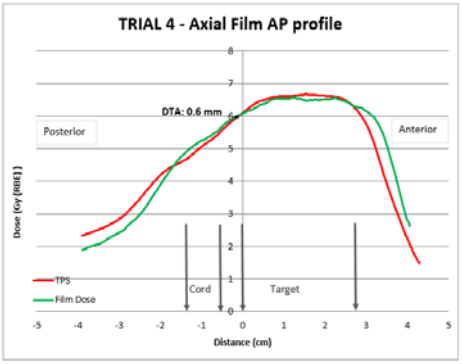

Figure 5-34: Axial (anterior to posterior) dose profile comparing the TPS dose with the measured film dose for Trial 4

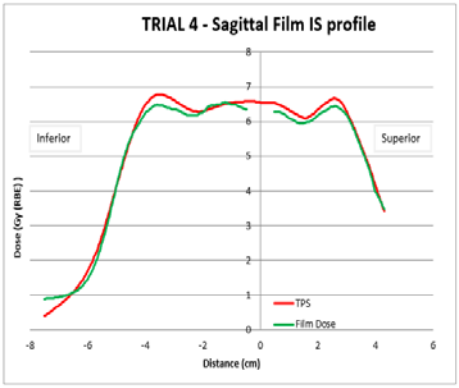

Figure 5-35: Sagittal (inferior to superior) dose profile comparing the TPS dose with the measured film dose for Trial 4

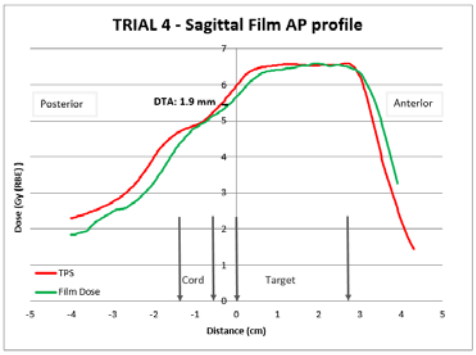

Figure 5-36: Sagittal (anterior to posterior) dose profile comparing the TPS dose with the measured film dose for Trial 4

5.2.3 Trial 5 Profiles

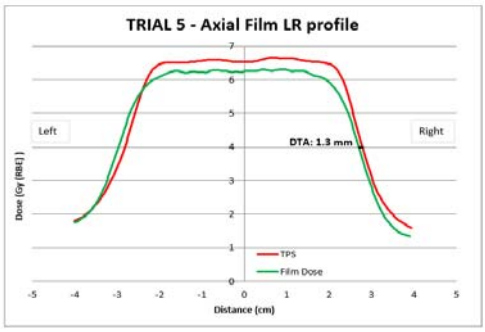

Figure 5-37: Axial (left to right) dose profile comparing the TPS dose with the measured film dose for Trial 5

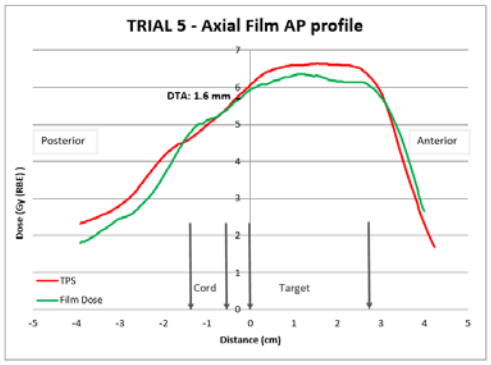

Figure 5-38: Axial (anterior to posterior) dose profile comparing the TPS dose with the measured film dose for Trial 5

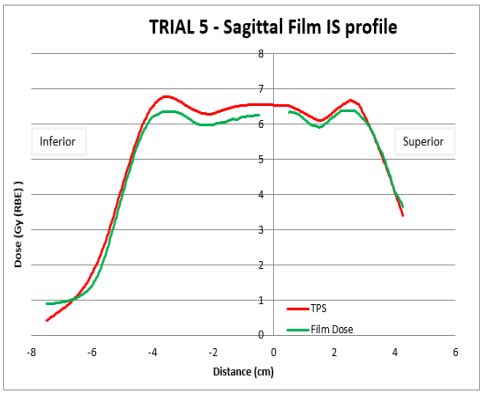

Figure 5-39: Sagittal (inferior to superior) dose profile comparing the TPS dose with the measured film dose for Trial 5

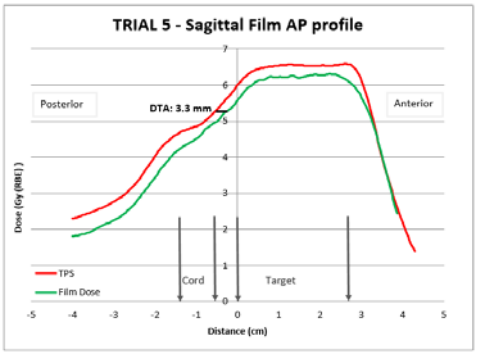

Figure 5-40: Sagittal (anterior to posterior) dose profile comparing the TPS dose with the measured film dose for Trial 5

5.2.4 Trial 6 Profiles

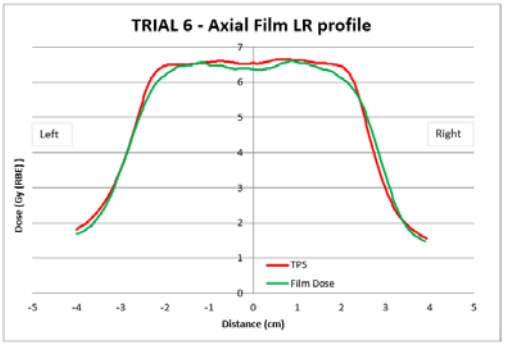

Figure 5-41: Axial (left to right) dose profile comparing the TPS dose with the measured film dose for Trial 6

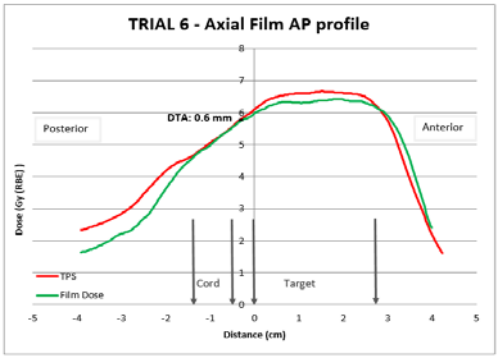

Figure 5-42: Axial (anterior to posterior) dose profile comparing the TPS dose with the measured film dose for Trial 6

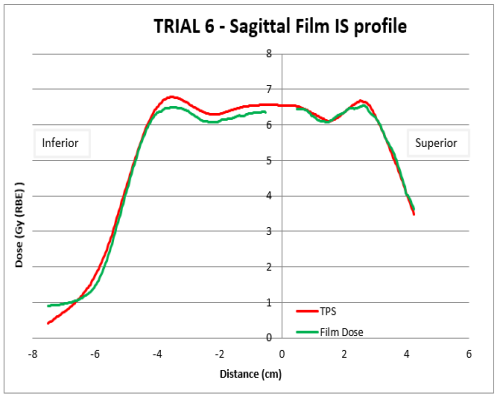

Figure 5-43: Sagittal (inferior to superior) dose profile comparing the TPS dose with the measured film dose for Trial 6

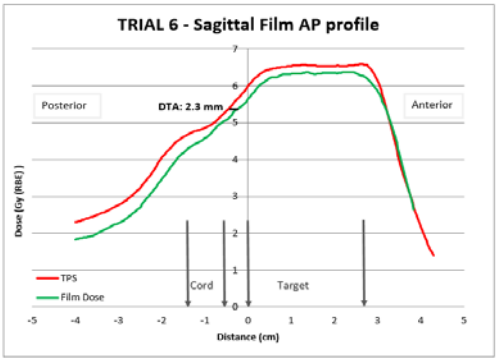

Figure 5-44: Sagittal (anterior to posterior) dose profile comparing the TPS dose with the measured film dose for Trial 6

5.3 PTC – H Phantom QA Report

Department of Radiation Physics, Division of Radiation Oncology M.D. Anderson Cancer Center / Proton Therapy Center Houston

Scanning Proton Beam Patient Specific QA Report

Patient: **ProtonHead, db** MRN: **zzIROC**

Db Protonhead is to receive treatment with proton therapy using the scanning beam in G3. The multi-field optimized treatment plan consists of 3 fields. The plan calls for 6 cGy (RBE) delivered to the GTV in 1 fraction. The parameters of the fields are listed in Table 1.

Prescription	GTV (cc)	(cc)	Field	Nominal Range (cm)	Nominal SOBP (cm)	Max E (MeV)	Layers	Total Spots	MU
Isodose Line (%)	96.7	0	DPAPB	14.97	9.09	144.9	36	3851	135.94
			ERAPB	11.95	8.99	131	40	3309	114.45
			FLAPB	12.55	8.87	132.8	40	3742	131.9

Table 1: Treatment field parameters.

Comprehensive quality assurance measurements of dose distribution were performed for this patient's treatment plan on July 09, 2016. The results are discussed below.

(1) Dose measurements delivered through MOSAIQ™ at the planned gantry angle for each field

In the Eclipse treatment planning system (TPS), a verification plan was created on a digital water phantom. The SSDs and the measurement depths for each field are listed in Table 2. The plan provided a calculated 3D dose distribution for each field. The 2D dose-

distribution-plane perpendicular to the beam direction and intersecting with the isocenter was extracted to compare with measurements. A 2D ion-chamber-array detector (MatriXX) was mounted to the couch via a rotatable attachment and then used to measure the same dose-planes from the treatment-prescribed gantry angles. The measured 2D physical dose distributions were corrected for daily machine output variation, and compared with the TPS-calculated physical dose distributions. Results are shown in Figures 1 - 6. ***All measurements agreed reasonably well with over 95% of pixels passing the 3%/3 mm dose/distance agreement criteria.***

Field	Gantry angle (°)	Snout Position (cm)	SSD (cm)	Depth (cm)	Gamma index (3% /3mm)
DPAPB	180	38	265	5	100.00%
ERAPB	295	38	268	2	95.10%
FLAPB	65	38	265	5	99.40%

Table 2. Gamma index passing rate for fields delivered at treatment gantry angles.

(2) TPS dose calculations compared to HPlusQA

The verification plan was exported from Eclipse to HPlusQA, a patient specific QA system with an independent dose calculation algorithm (Mackin *et al.*Med. Phys. 40, 121708, 2013). The 3D dose distributions from Eclipse were then compared to dose distributions calculated by HPlusQA. Figure 7 shows a dose depth profile comparison of the Eclipse and HPlusQA calculations for each field in the verification plan. The 2D gamma index was used to compare the Eclipse and the HPlusQA dose calculations in a virtual uniform water phantom. The results of these comparisons are given in Table 3. ***The gamma pass rate for HPlusQA***

and Eclipse using 3%/3 mm dose/distance agreement criteria is 100% for all examined depths.

Beam	Depth (cm)	Gamma Index (3%,3mm)
Posterior	5.0	100
	7.9	100
Right Oblique	2.0	100
	8.4	100
Left Oblique	5.0	100
	8.4	100

Table 3. HPlusQA vs. Eclipse gamma index passing percentages. DTA is distance to agreement.

(3) Dose measurements delivered in physics mode for each field

The MatriXX ion chamber array was used to measure the 2D dose distribution in the solid water phantom at several depths for each field. The gamma index scores comparing these measured dose planes to dose planes calculated by Eclipse are listed in Table 4, and the results are shown in Figures 8 - 13. Also, point doses extracted from the measured dose planes are compared to dose profiles (parallel to the beam axis) extracted from both Eclipse and HPlusQA dose calculations in Fig. 7. ***The measurements generally agree with Eclipse with all examined depths having gamma pass rates greater than 95% using 3%/3 mm dose/distance agreement criteria.***

Beam	Depth (cm)	Gamma Index (3%,3mm)
Posterior	5.0	100
	7.9	100

Right Oblique	2.0	95.1
	8.4	100
Left Oblique	5.0	99.4
	8.4	100

Table 4. Gamma index passing percentages for dose planes calculated using a MatriXX ion chamber array compared to dose planes calculated with Eclipse.

Reported by:

Matthew D. Kerr ID#: 186421 Certification: BS Physics Date: 07/10/2016

Reviewed by:

[PHYS. NAME] ID#: Certification:[B.A.,MS,PhD] Date: [DATE]

5.3.1.1 MOSAIQ™ Measurements: MatriXX versus Eclipse (3 mm, 3%), Field: DPAPB

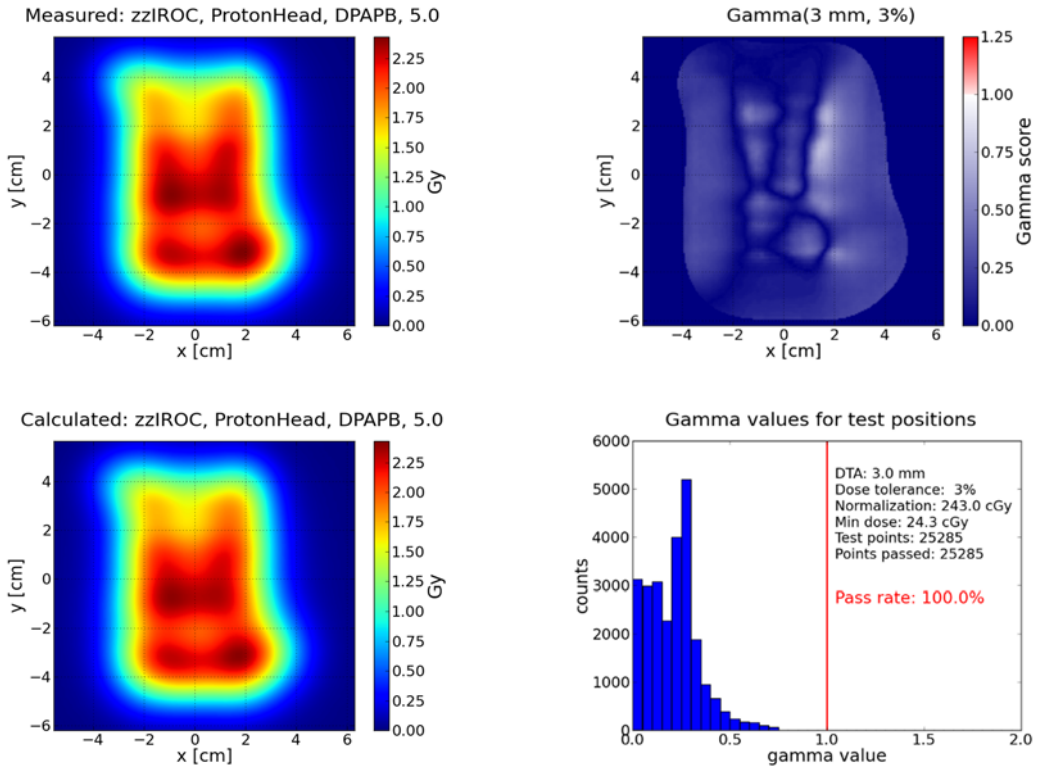

Figure 1: Gamma analysis for field DPAPB (gantry = 180°). Upper left: dose plane measured with a MatriXX ion chamber array; lower left: dose plane calculated with Eclipse; upper right: gamma index map; lower right: histogram of gamma index values for the test pixels. 100.0% of the pixels passed the 3%/3 mm dose/distance agreement criteria. The measurements were made at a water equivalent depth of 5.0 cm.

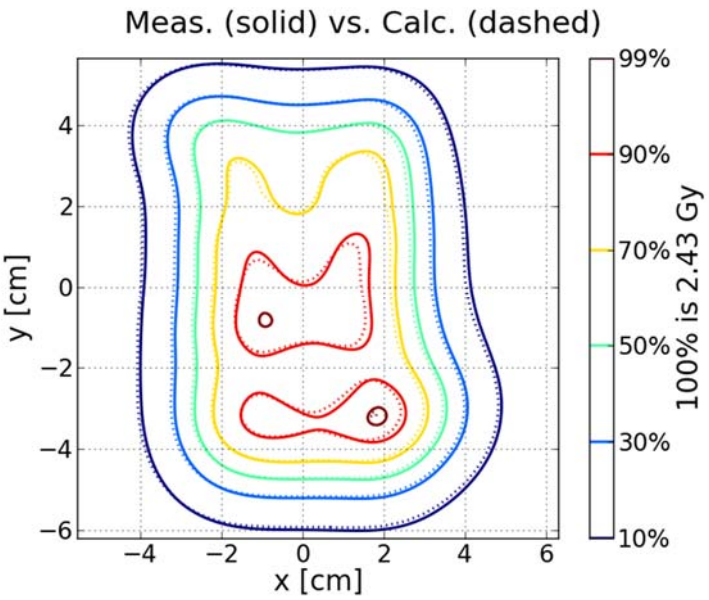

Figure 2: Isodose line-comparison of dose measured with a MatriXX ion chamber array and dose calculated with Eclipse. The measurements were made at a water equivalent depth of 5.0 cm.

5.3.1.2 MOSAIQ™ Measurements: MatriXX versus Eclipse (3 mm, 3%), Field: ERAPB

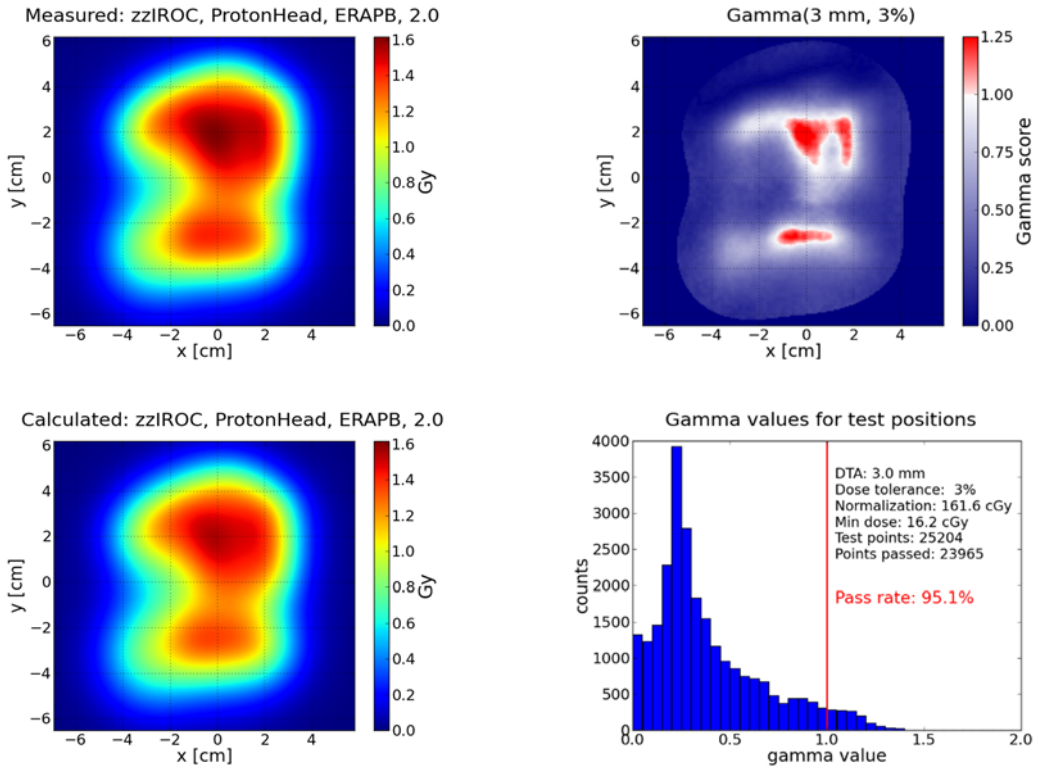

Figure 3: Gamma analysis for field ERAPB (gantry = 295°). Upper left: dose plane measured with a MatriXX ion chamber array; lower left: dose plane calculated with Eclipse; upper right: gamma index map; lower right: histogram of gamma index values for the test pixels. 95.1% of the pixels passed the 3%/3 mm dose/distance agreement criteria. The measurements were made at a water equivalent depth of 2.0 cm.

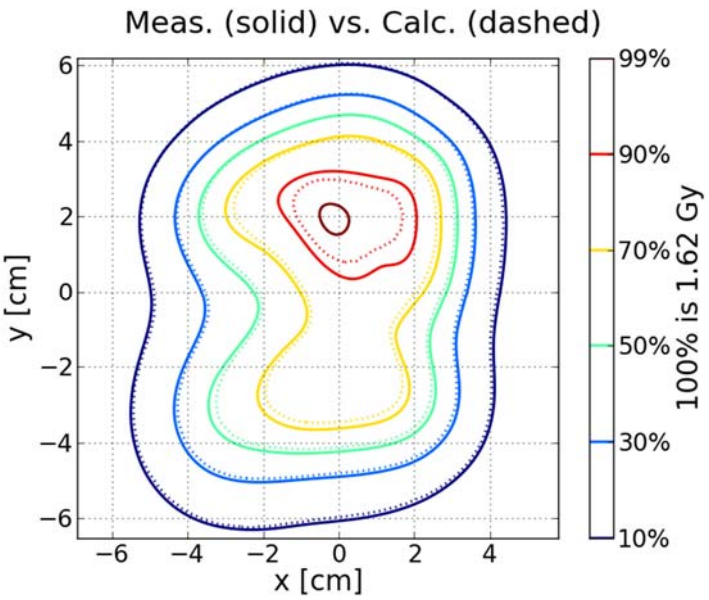

Figure 4: Isodose line-comparison of dose measured with a MatriXX ion chamber array and dose calculated with Eclipse. The measurements were made at a water equivalent depth of 2.0 cm.

5.3.1.3 MOSAIQ™ Measurements: MatriXX versus Eclipse (3 mm, 3%), Field: FLAPB

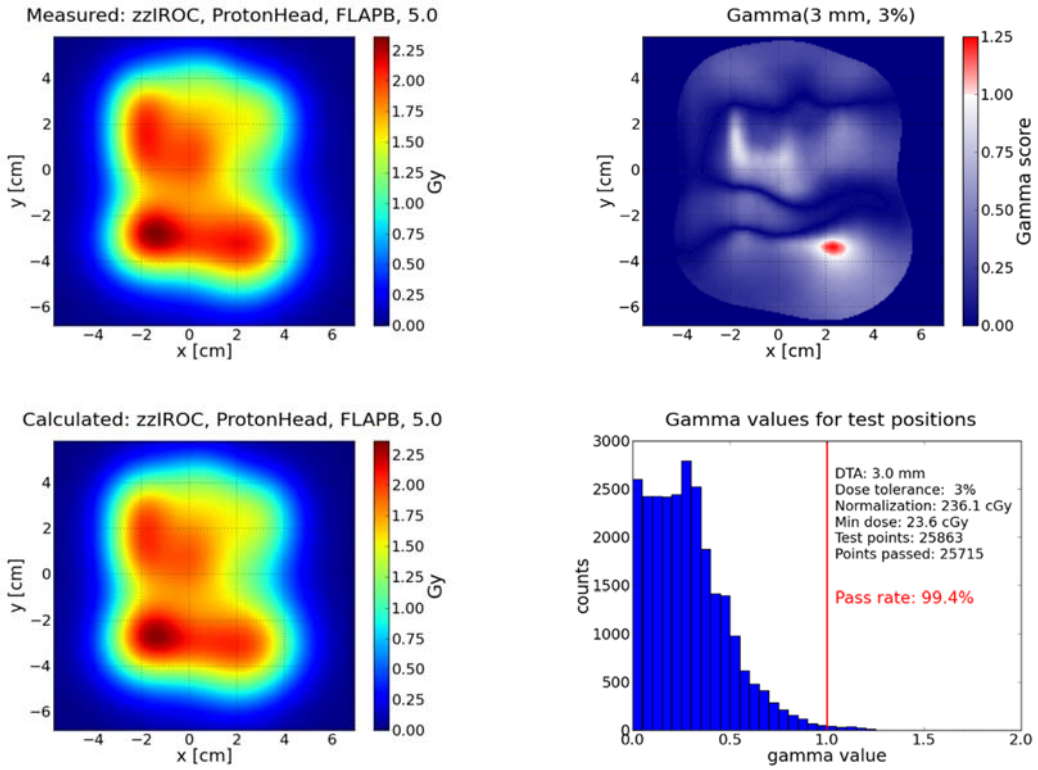

Figure 5: Gamma analysis for field FLAPB (gantry = 65°). Upper left: dose plane measured with a MatriXX ion chamber array; lower left: dose plane calculated with Eclipse; upper right: gamma index map; lower right: histogram of gamma index values for the test pixels. 99.4% of the pixels passed the 3%/3 mm dose/distance agreement criteria. The measurements were made at a water equivalent depth of 5.0 cm.

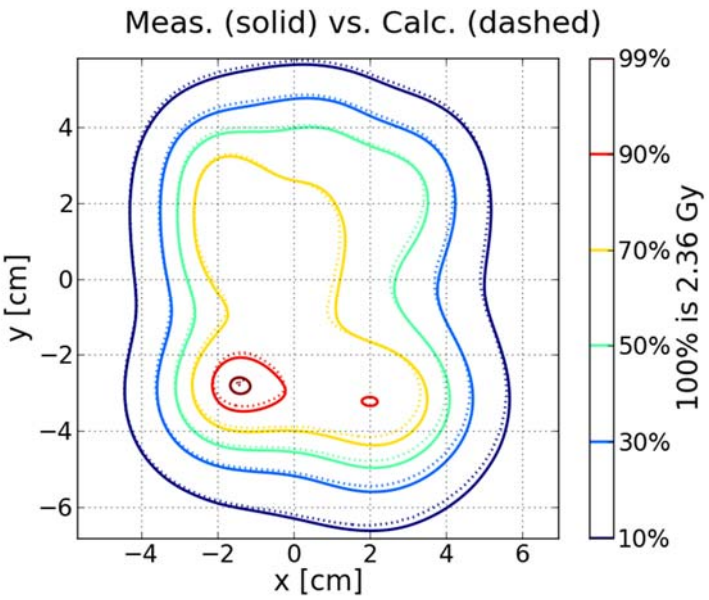

Figure 6: Isodose line-comparison of dose measured with a MatriXX ion chamber array and dose calculated with Eclipse. The measurements were made at a water equivalent depth of 5.0 cm.

5.3.1.4 Treatment Field Profiles

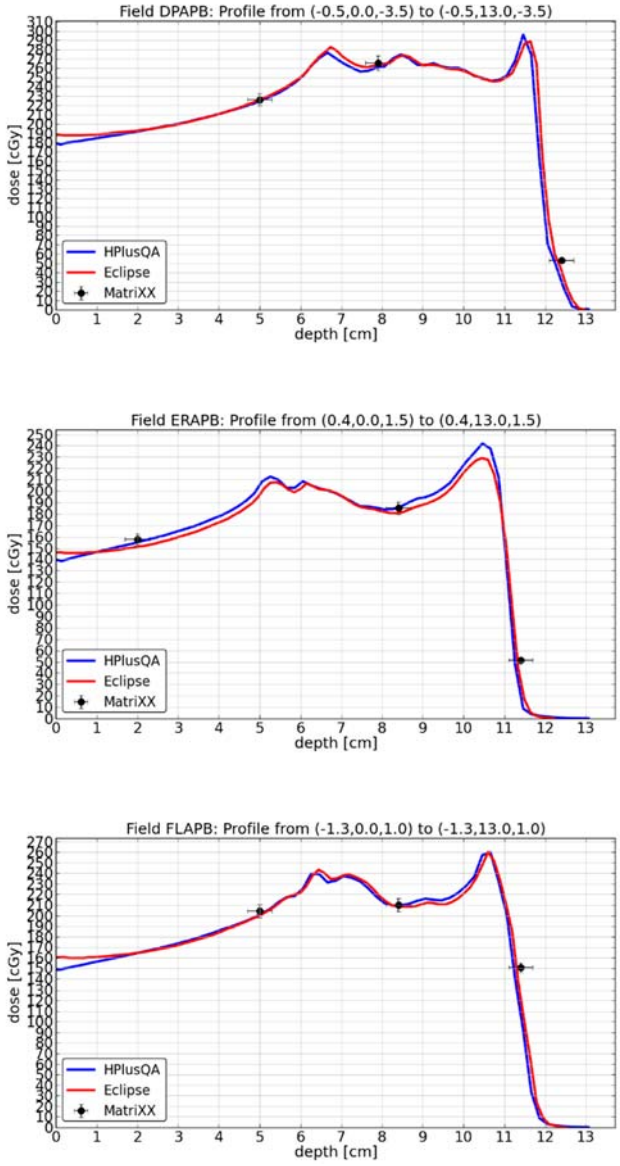

Figure 7: Comparisons of dose depth profiles calculated by Eclipse and HPlusQA. Point doses extracted from dose planes measured with a Matrixx ion chamber array are indicated using black dots. The error bars extending from the black dots represent 3% and 3-mm uncertainties in the horizontal and vertical directions respectively.

5.3.1.5 Depth Measurements: MatriXX versus Eclipse (3 mm, 3%), Field: DPAPB, Depth: 7.9 cm

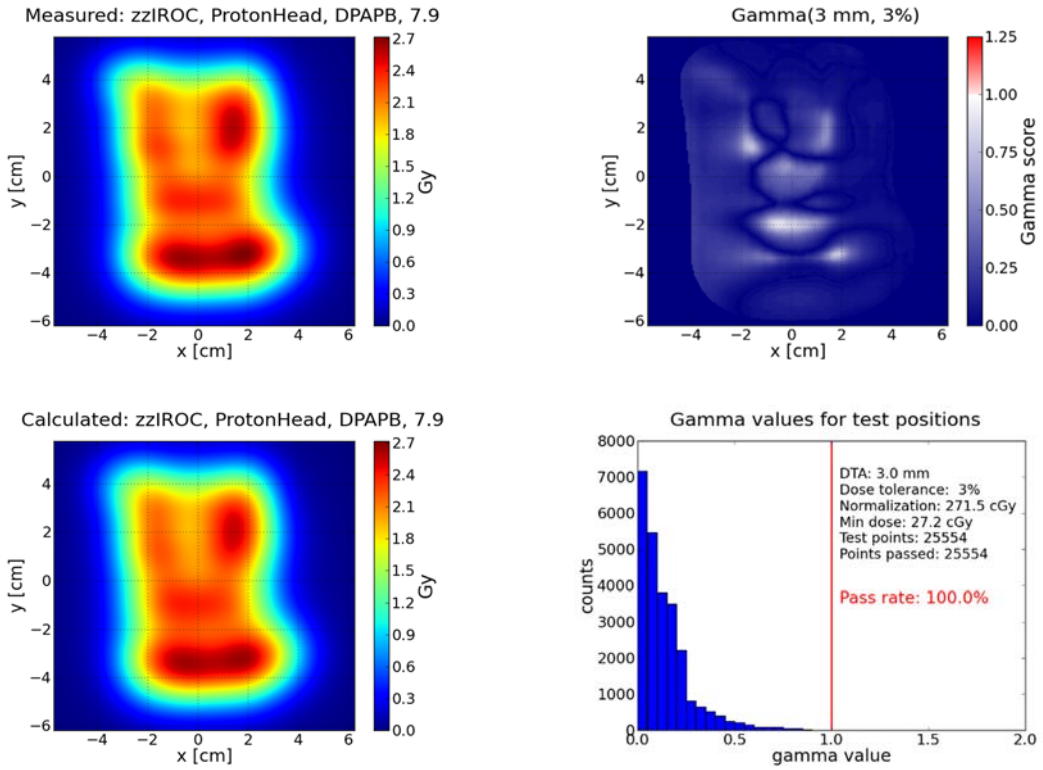

Figure 8: Gamma analysis for field DPAPB. Upper left: dose plane measured with a MatriXX ion chamber array; lower left: dose plane calculated with Eclipse; upper right: gamma index map; lower right: histogram of gamma index values for the test pixels. 100.0% of the pixels passed the 3%/3 mm dose/distance agreement criteria.

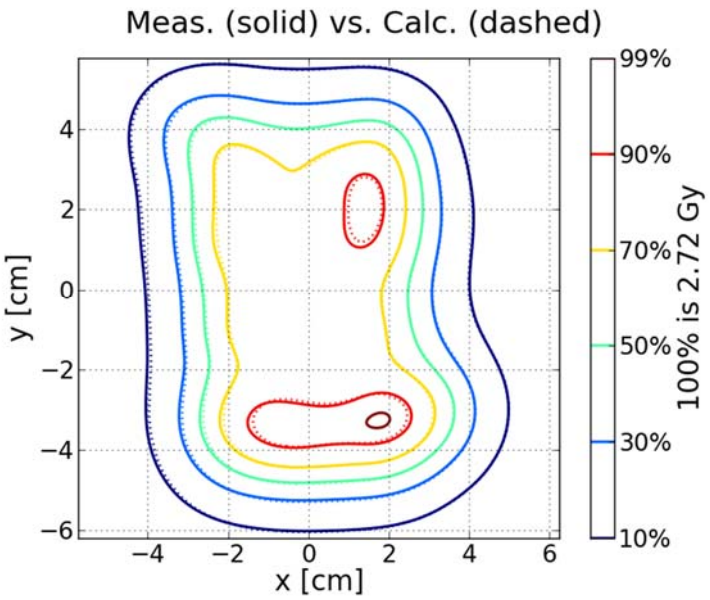

Figure 9: Isodose line-comparison of dose measured with a MatriXX ion chamber array and dose calculated with Eclipse. The measurements were made at a water equivalent depth of 7.9 cm.

5.3.1.6 Depth Measurements: MatriXX versus Eclipse (3 mm, 3%), Field: ERAPB, Depth: 8.4 cm

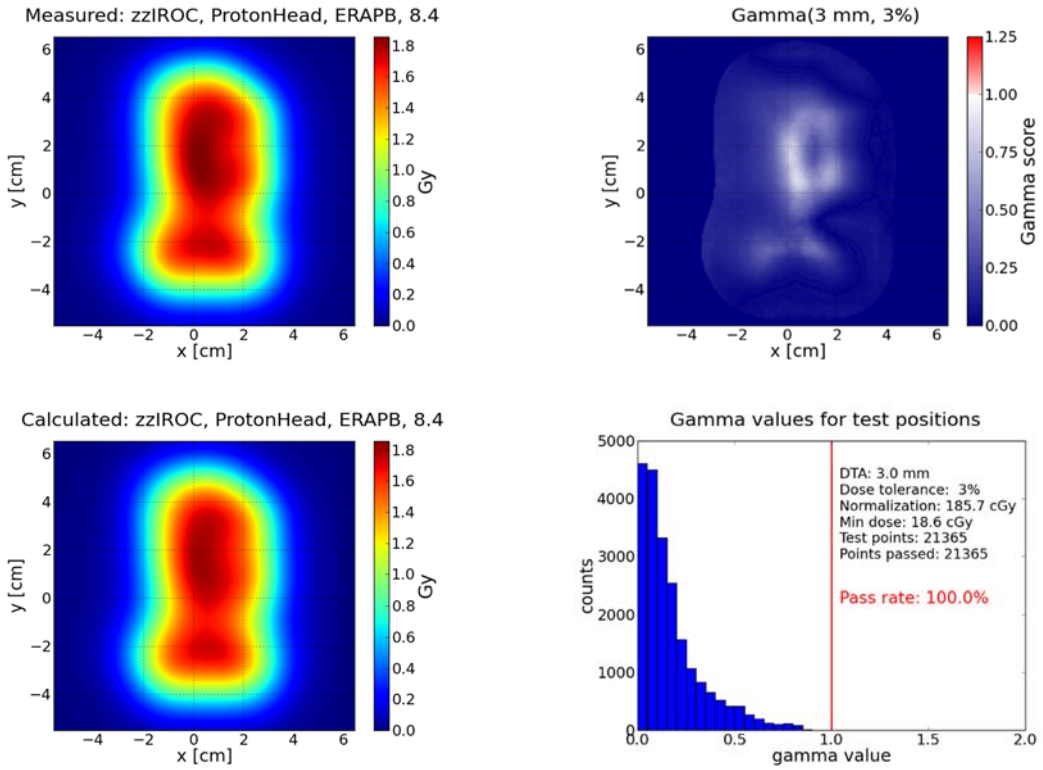

Figure 10: Gamma analysis for field ERAPB. Upper left: dose plane measured with a MatriXX ion chamber array; lower left: dose plane calculated with Eclipse; upper right: gamma index map; lower right: histogram of gamma index values for the test pixels. 100.0% of the pixels passed the 3%/3 mm dose/distance agreement criteria.

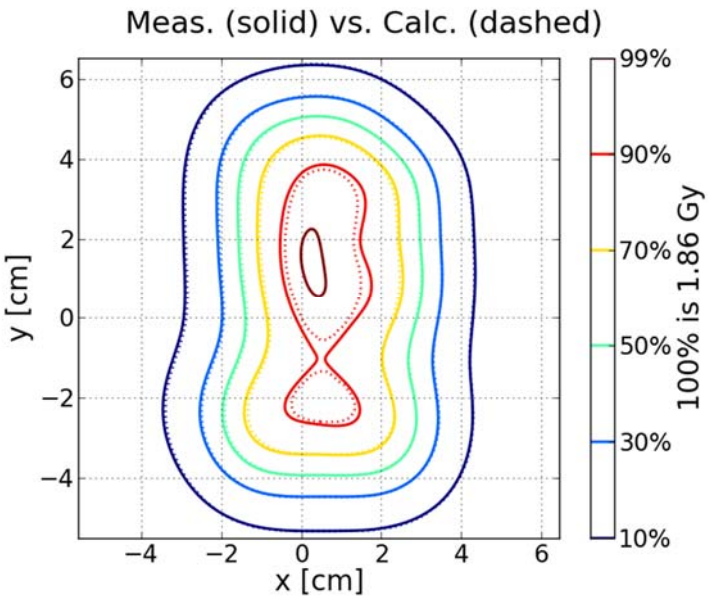

Figure 11: Isodose line-comparison of dose measured with a MatriXX ion chamber array and dose calculated with Eclipse. The measurements were made at a water equivalent depth of 8.4 cm.

5.3.1.7 Depth Measurements: MatriXX versus Eclipse (3 mm, 3%), Field: FLAPB, Depth: 8.4 cm

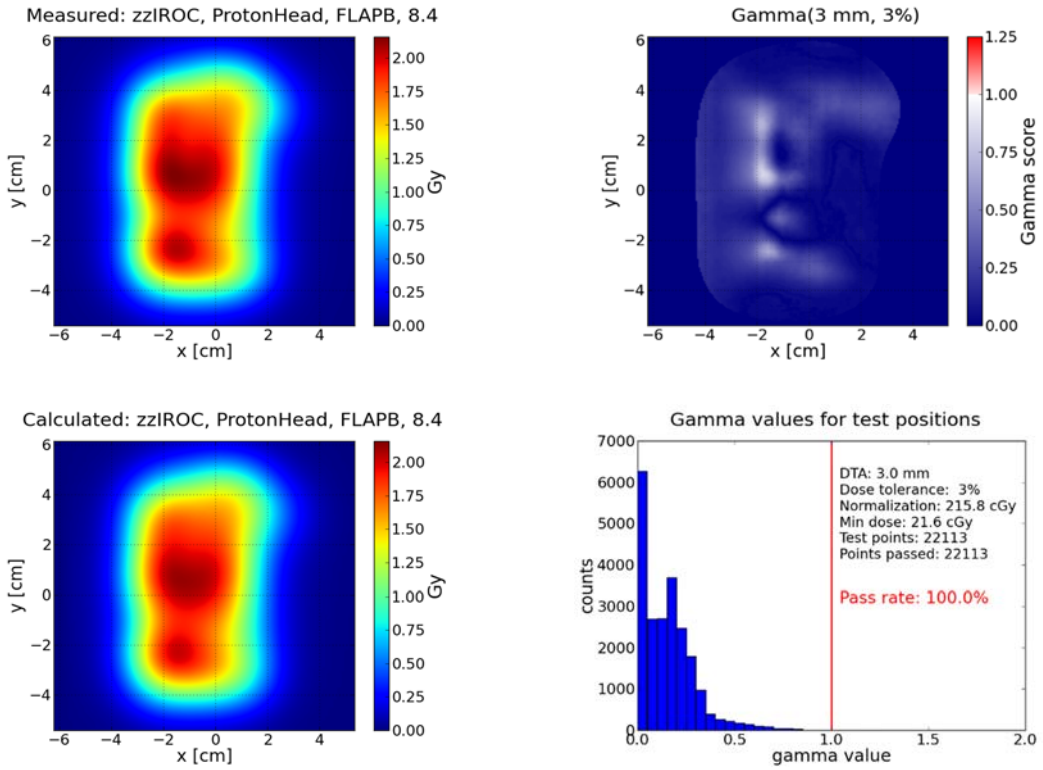

Figure 12: Gamma analysis for field FLAPB. Upper left: dose plane measured with a MatriXX ion chamber array; lower left: dose plane calculated with Eclipse; upper right: gamma index map; lower right: histogram of gamma index values for the test pixels. 100.0% of the pixels passed the 3%/3 mm dose/distance agreement criteria.

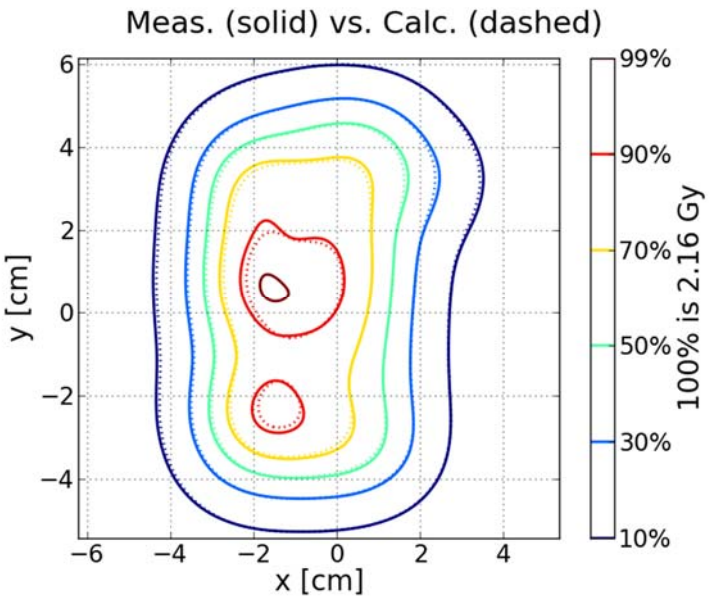

Figure 13: Isodose line-comparison of dose measured with a MatriXX ion chamber array and dose calculated with Eclipse. The measurements were made at a water equivalent depth of 8.4 cm.

6 References

1. *The National Association for Proton Therapy*. [cited 2016 04]; Available from: http://www.proton-therapy.org/.
2. *9 QUALITY ASSURANCE.* Journal of the ICRU, 2007. **7**(2): p. 135-139.
3. *Imaging and Radiation Oncology Core-IROC*. [cited 2016; Available from: http://rpc.mdanderson.org/RPC/home.htm.
4. *Guidelines for the Use of Proton Radiation Therapy in NCI Sponsored Cooperative Group Clinical Trials.* 2012.
5. Ibbott, G.S., et al., *Challenges in Credentialing Institutions and Participants in Advanced Technology Multi-institutional Clinical Trials.* International Journal of Radiation Oncology • Biology • Physics, 2008. **71**(1): p. S71-S75.
6. Followill, D.S., et al., *Design, development, and implementation of the radiological physics center's pelvis and thorax anthropomorphic quality assurance phantoms.* Med Phys, 2007. **34**(6): p. 2070-6.
7. Warnakulasuriya, S., *Global epidemiology of oral and oropharyngeal cancer.* Oral oncology, 2009. **45**(4): p. 309-316.
8. Ferlay, J., et al., *Estimates of worldwide burden of cancer in 2008: GLOBOCAN 2008.* Int J Cancer, 2010. **127**(12): p. 2893-917.
9. *National Cancer Institute SEER Cancer Statistics Factsheets: Oral Cavity and Pharynx Cancer*. Available from: http://seer.cancer.gov/statfacts/html/oralcav.html.
10. Lambert, R., et al., *Epidemiology of cancer from the oral cavity and oropharynx.* European Journal of Gastroenterology & Hepatology, 2011. **23**(8): p. 633-641.

11. Cleveland, J.L., et al., *The connection between human papillomavirus and oropharyngeal squamous cell carcinomas in the United States.* The Journal of the American Dental Association, 2011. **142**(8): p. 915-924.

12. Moore, S., A. Pierce, and D. Wilson, *'Oral cancer'—the terminology dilemma.* Oral diseases, 2000. **6**(3): p. 191-193.

13. Pandey, M., R. Bindu, and C.S. Soumithran, *Results of primary versus salvage surgery in carcinoma of the buccal mucosa.* Eur J Surg Oncol, 2009. **35**(4): p. 362-7.

14. Sherman, C.D., *Cancer of the Head and Neck*, in *Manual of Clinical Oncology*, C.D. Sherman, et al., Editors. 1990, Springer Berlin Heidelberg: Berlin, Heidelberg. p. 188-203.

15. A-J. Tuyns, et al., *Cancer of the larynx/hypopharynx, tobacco and alcohol: Iarc international case-control study in Turin and Varese (Italy), Zaragoza and Navarra (Spain), Geneva (Switzerland) and Calvados (France).* 2006. **41**(4): p. 483-491.

16. Brennan , J.A., et al., *Association between Cigarette Smoking and Mutation of the p53 Gene in Squamous-Cell Carcinoma of the Head and Neck.* New England Journal of Medicine, 1995. **332**(11): p. 712-717.

17. CHOI, S.Y. and H. KAHYO, *Effect of Cigarette Smoking and Alcohol Consumption in the Aetiology of Cancer of the Oral Cavity, Pharynx and Larynx.* International Journal of Epidemiology, 1991. **20**(4): p. 878-885.

18. Craig S. Miller, Dean K. White, and K. Lexington, *Human papillomavirus expression in oral mucosa, premalignant conditions, and squamous cell carcinoma*
A retrospective review of the literature 1996. **82**(1).

19. Leyoshi Kobayashi, et al., *Prevalence of Epstein–Barr virus in oral squamous cell carcinoma.* 1999.

20. Tinhofer, I., et al., *Contribution of human papilloma virus to the incidence of squamous cell carcinoma of the head and neck in a European population with high smoking prevalence.* Eur J Cancer, 2015. **51**(4): p. 514-21.

21. Franceschi S, et al., *Food groups, oils and butter, and cancer of the oral cavity and pharynx.* 1999.

22. Mary Anne Rossing, Thomas L. Vaughan, and B. McKnight, *Diet and pharyngeal cancer.* 2006. **44**(4).

23. Winn, D.M., et al., *Diet in the Etiology of Oral and Pharyngeal Cancer among Women from the Southern United States.* Cancer Research, 1984. **44**(3): p. 1216-1222.

24. A.M. Vellya, et al., *Relationship between dental factors and risk of upper aerodigestive tract cancer.* 1998. **34**(4): p. 284-291.

25. L. Holmes Jr, et al., *Is dental care utilization associated with oral cavity cancer in a large sample of community-based United States residents?* 2008. **37**(2): p. 134-142.

26. Jean J Moulin, et al., *Oral cavity and laryngeal cancers among man-made mineral fiber production workers.* 1986. **12**: p. 27-31.

27. Thomas L. Vaughan, et al., *Formaldehyde and cancers of the pharynx, sinus and nasal cavity: I. Occupational exposures.* 2006. **38**(5): p. 677–683.

28. Tina Liebling, et al., *Cancer mortality among workers exposed to formaldehyde.* 2007. **5**(6): p. 423-428.

29. Lynch HT , Fusaro RM , and L. J, *Hereditary cancer in adults.* 1995. **19**(3): p. 219-233.

30. Stimson P. Schantz, et al., *Young Adults With Head and Neck Cancer Express Increased Susceptibility to Mutagen-lnduced Chromosome Damage.* 1989. **262**(23).

31. Kinlen, L.J., *Cancer: Causes, Occurrence and Control.* 1991. **64**(5): p. 977-978.

32. JP Pignon, et al., *Chemotherapy added to locoregional treatment for head and neck squamous-cell carcinoma: three meta-analyses of updated individual data.* 2000. **355**(9208): p. 949-955.

33. Lawrence, T.S., *Milestones in the Use of Combined-Modality Radiation Therapy and Chemotherapy.* 2014.

34. *History of Proton Therapy*. Available from: http://www.mdanderson.org/patient-and-cancer-information/proton-therapy-center/what-is-proton-therapy/history-of-proton-therapy/index.html.

35. Faiz Khan and J. Gibbons, *The Physics of Radiation Therapy*. 5 ed., Philadelphia: Lippincott Williams & Wilkins.

36. Frank, H.A., *Introduction to radiological physics and radiation dosimetry.* Attix.-1986-607 p, 2004.

37. B Schaffner and E. Pedroni, *The precision of proton range calculations in proton radiotherapy treatment planning: experimental verification of the relation between CT-HU and proton stopping power.* 1998. **43**(6).

38. Alfred Smith, et al., *The M. D. Anderson proton therapy system.* 2009. **36**(9).

39. Stefano Agosteoa, et al., *Secondary neutron and photon dose in proton therapy.* 1998. **48**: p. 293-305.

40. Tommasino, F. and M. Durante, *Proton radiobiology.* Cancers (Basel), 2015. **7**(1): p. 353-81.

41. Wayne D. Newhauser and M. Durante, *Assessing the risk of second malignancies after modern radiotherapy.* Nature Reviews Cancer, 2011. **11**: p. 438-448.

42. Uwe Schneider, S.A., Eros Pedroni, Jürgen Besserer, *Secondary neutron dose during proton therapy using spot scanning.* 2002. **53**(1): p. 244-251.

43. Luca Cozzia, et al., *A treatment planning comparison of 3D conformal therapy, intensity modulated photon therapy and proton therapy for treatment of advanced head and neck tumours.* 2001. **61**(3): p. 287-297.

44. Marloes Stenekera, Antony Lomaxa, and U. Schneider, *Intensity modulated photon and proton therapy*

for the treatment of head and neck tumors. Vol. 80. 2006.

45. Harald Paganetti, et al., *Relative biological effectiveness (RBE) values for proton beam therapy.* 2002. **53**(2): p. 407-421.

46. Paganetti, H., *Range uncertainties in proton therapy and the role of Monte Carlo simulations.* Physics in Medicine and Biology, 2012. **57**(11).

47. Ryan L. Grant, et al., *Relative stopping power measurements to aid in the design of anthropomorphic phantoms for proton radiotherapy.* 2014. **15**(2).

48. McInnis, M., *GSBS Thesis - Assessment of Uncertainty in Planning and Dose Delivery of Proton Therapy in an IROC-Houston QA Phantom due to Variable CT Technique and Proton Energy.* 2015.

49. S. Reinhardt, et al., *Comparison of Gafchromic EBT2 and EBT3 films for clinical photon and proton beams.* 2014. **39**.

50. Bijan Arjomandy, et al., *Energy dependence and dose response of Gafchromic EBT2 film over a wide range of photon, electron, and proton beam energies.* 2010. **37**.

51. Kevin, A., *Development of a Novel Readout System for Radiochromic Film Dosimetry*. 2014.

52. Schuemann, J., et al., *Assessing the Clinical Impact of Approximations in Analytical Dose Calculations for Proton Therapy*. 2015.

7 Vita

Daniela Rezende Fiuza Branco was born in Belo Horizonte, Brazil, daughter of Manuel da Rocha Fiuza Branco Junior and Maria Celeste Fiuza Branco. After completing high school, she moved to the United States to pursue her college education at Northern Michigan University, Marquette MI. She transferred to Wright State University, Dayton OH, where she obtained her bachelors of science in physics in 2014. Following that she entered The University of Texas Graduate School of Biological Sciences at Houston where she completed her Master's degree. She plans on continuing her education and pursing her PhD in Medical Physics.